A study of pellet-plasma interactions using fast three-dimensional imaging in Large Helical Device

Jyoti Shankar Mishra

DOCTOR OF
PHILOSOPHY

Department of Fusion Science
School of Physical Sciences
The Graduate University for Advance Studies

2011 (School Year)

Dedicated to my parents

"Science knows no country, because knowledge belongs to humanity, and is the torch which illuminates the world."

– Louis Pasteur

Acknowledgements

Three years of study at National Institute for fusion Science (NIFS) passed like a speeding *Shinkansen*. *Sakura* blossomed with time, and will be in the next spring, but I will miss it; it will be a pleasant memory forever. Time to wrap-up my thesis on pellet fueling studies in the Large Helical Device (LHD). I take this opportunity to thank the peoples helped me during this course of work.

At first, my deep sense of gratitude and appreciation to my thesis supervisor Dr. Ryuichi Sakamoto for giving me an opportunity to undertake this PhD project. I sincerely thank him for his continuous encouragement and endless support. Whenever I get puzzled, he comes up with a viable solution. Not only plasma physics but also I learn other aspect of the experimental work from him. I am deeply thankful to him and his family for their help towards my family during my stay in Japan

I would also like to thank Prof. Hiroshi Yamada for his continuous encouragement and suggestions on my work, especially, during any presentations. Sincere thank to Dr. G. Motojima and Dr. A. Matsuyama for their cooperation during my work in NIFS. It's my pleasure to acknowledge fellow graduate student and my tutor Mr. A. Murakami for helping me, whenever I need.

My sincere thank to Prof. S Morita for the interesting conversations on diverged topics in leisure time. Special thank to Prof. B. Peterson for helping in English correction of my papers. I would like to thank peoples of the engineering group for helping me in the pellet injector installation. It is pleasure to acknowledge Prof. S. Okamura, Prof. S. Sudo, Prof. M. Skoric, Dr. J. Miyazawa, Dr. T. Morisaki, Dr. S. Masuzaki, Dr. M. Goto, Dr. M. Kobayashi, Dr. N. Yanagi, Dr. K. Tsumori. I would also like to thank all my fellow graduate students.

I wish to express my appreciation to all the members of the LHD experimental group, NIFS, and the administrative staffs for their support. My sincere gratitude to previous and present Director General of NIFS Prof. Osamu Motojima and Prof. Akio Komori, respectively for their encouragement.

Back-home in India, I am grateful to Prof. P. K. Kaw, Director, Institute for Plasma Research (IPR), Gandhinagar, for his continuous interest, and to the members of the academic committee for granting me leave to pursue my higher study. I wish to convey my regards to my boss Ms. R.

Gangradey, for her encouragement. Sincere thank to my colleagues Mr. N. Ravi Pragash, Mr. B. Ramesh, Dr. M. B. Chowdhuri. I would also like to thank Mr. S. Joisa, with whom I start my professional work in SXR diagnostics group. Thanks to all my friends in India, for their continuos encouragement for my PhD.

I would like to thank all the Japanese friends for their continuous support towards my social life in Japan. Special thank to Mr. Yutaka and his wife Ms. Noy for their endless help. I would also like to thank Ms. Sachie, Ms. Misuzu and their family, and Ms. Mieko for their continuous help on various social matters.

Many many thanks to our beloved *bhaina* (Mr. CRC Mohanty) and *bhauja* (Ms. S. Mohanty), for those joyful moments we share in many occasions. Thanks to my all cricketer friends for those cricketing times, which boost my energy from time to time.

I am indebted to my wife Jini for her inexhaustible love and inspirations, and especially, during the moments I face difficulty in my work. The joyful moments I share with my cute son Shashwat is simply inexpressible.

I wish to thank my in-laws and family members, for their continuous encouragement during my PhD. Finally, I am grateful to my parents for their endless love, support and encouragement towards my research work. To them, I dedicate my thesis.

List of Publications

[1] “A low speed single barrel pellet injector and its application to complementary study on ablatant in LHD”,
J. S. Mishra, R. Sakamoto, G. Motojima, H. Yamada,
J. Plasma Fusion Res. SERIES, Vol. 9 (2010).

[2] “Design and performance of a punch mechanism based pellet injector for alternative injection in the large helical device ”,
J. S. Mishra, R. Sakamoto, G. Motojima, A. Matsuyama, H. Yamada,
Review. of Scientific Instruments, 82, 023505 (2011).

[3] “Observation of three-dimensional motion of pellet ablatant in LHD”,
J. S. Mishra, R. Sakamoto, G. Motojima, A. Matsuyama, H. Yamada,
Proceedings of 37^{th} EPS Conference on Plasma Physics, P5.170.

[4] “Observation of three-dimensional motion of the pellet ablatant in the Large Helical Device”,
J. S. Mishra, R. Sakamoto, A. Matsuyama, G. Motojima, H. Yamada,
Nucl. Fusion 51 (2011) 083039.

Abstract

This study is focused on to address the pellet fueling issues such as ablation and mass redistribution in the large helical device (LHD). It has been found that the ablation dynamics strongly regulated by the local fast ion density profile generated due to the neutral beam injection (NBI) heating. Owing to the asymmetric ablation in presence of the fast ions, three dimensionality in the pellet trajectory, and subsequently change in the fueling characteristics has been observed. To explore the improved fueling properties by considering the ∇B structure of the injection location on the pellet ablatant, pellet injection studies are performed for the high field side, and the low field side injection locations. A comparative study of fueling efficiency is presented at different plasma conditions for these locations.

To deliver an intact pellet within the curved guiding path for an injection location other than outboard side, a low speed pellet injector is developed. This injector works on the combined operation of a mechanical punch and He propellant gas. This injector can inject a 3 mmφ $\times$ 3 mmℓ intact pellet with speed ≤ 275 ms^{-1} at a pellet formation temperature of 8.0 K, flexibly. The loss in pellet speed and mass inside the guide tube are less than 6% and 10%, respectively.

Since, pellets are injected into the plasmas of 3D magnetic configuration, a three-dimensional pellet-plasma interaction can be predicted. Therefore, applying the stereoscopic technique, a 3D diagnostics system has been calibrated to image the pellet ablation process inside the plasma. This imaging system uses a fast camera (time resolution of μs scale) and bifurcated coherent imaging fiber. The calibration error of this system is $< \pm$ 20 mm in the pellet penetration direction and within ± 5 mm in the transverse direction, and is able to measure the ablation dynamics with good accuracy.

In presence of asymmetric tangential NBI heated plasmas in LHD, an ablating pellet deflects in toroidal and vertical direction rather than continuing its 1D motion along its injection direction. Whereas, a both sided NBI has less significant effect on the pellet deflection. The toroidal deflection is ≤ 20 cm with acceleration of the order of 10^6 ms^{-2}. The toroidal deflection is successfully explained due to the unilateral ablation by the fast ions on the pellet surface and the formation of the rocket force in passing fast ions direction. At higher n_e, reduction in deflection speed indicates the reduction of fast ion effect. In addition, the role of rotational transform on the pellet ablation

dynamics during its lifetime is explained. The three dimensionality of the ablation behavior by associating with the change in pellet speed affects the pellet penetration inside the plasma, and breaks the general assumption of the penetration depth, considering the constant pellet speed.

In case of the LFS injected pellet, similar to that of the tokomak results, an outward redistribution of the pellet mass has been observed in LHD. In tokomaks, owing to the ∇B induced redistribution of the pellet ablatant, a better fueling efficiency has been reported for HFS pellet injection. As the ideal HFS resides under the helical coil in LHD, it is difficult to access this location. Therefore, in an alternative approach, injection of a pellet from the vessel inboard side with an oblique angle to a location closed to the helical coil has been considered. The injection position is optimized by performing a simple calculation for $\boldsymbol{E} \times \boldsymbol{B}$ drift effect on the plasmoid for that location. In alternative injection case, due to the fast ion effect, the pellet deflects three dimensionally to a location having similar characteristic as that of the LFS injection. Therefore, final mass deposition profile seems to be similar as that of the LFS injection case. The difference in pellet penetration and the deposition peak is around 15 - 20 cm. This indicates the outward redistribution of pellet mass. This behavior is also confirmed by analyzing the pellet ablation images, where outward mass drift at a speed of 8-10 kms^{-1} or more has been recorded. Considering the $\boldsymbol{E} \times \boldsymbol{B}$ drift effect for the alternative injection, it has been found that there are certain possibilities for enhanced deposition, if the pellet can be able to approach the calculated HFS location.

This work leads to the conclusion that the fast ions play a significant role in the pellet ablation process. While discussing the fueling process in the fusion reactor, the effect of the energetic ions on the pellet penetration process should be taken into account. Considering the similarity in redistribution phenomenon of the pellet ablatant in LHD and tokomak for LFS injection, it can be said that, the HFS fueling is necessary for reactor grade plasmas.

Contents

Table of Contents xi

List of Figures xii

List of Tables xvi

1 Introduction 1
- 1.1 World energy crises . . . 1
- 1.2 Nuclear fusion and plasma physics . . . 2
- 1.3 Plasma fueling and pellet injection . . . 3
- 1.4 Pellet injection and relevant diagnostics in LHD. . . . 5
- 1.5 Objective of this thesis . . . 10
- 1.6 Outline of thesis . . . 11

2 Pellet fueling scenarios in helical system 13
- 2.1 Introduction . . . 13
- 2.2 Pellet ablation . . . 14
- 2.3 Mass homogenization . . . 15
- 2.4 LHD and ∇B structure . . . 19
- 2.5 Injection position optimization . . . 21
- 2.6 Summary . . . 25

3 Development and characterizations of a low-speed pellet injector 27
- 3.1 Introduction . . . 27
- 3.2 Design Criteria . . . 28
- 3.3 Design of the pellet injector . . . 29
  - 3.3.1 Properties of Hydrogen isotopes . . . 29
  - 3.3.2 Cryogenic Chamber . . . 32
  - 3.3.3 Vacuum and gas feed system . . . 33
  - 3.3.4 Diagnostics . . . 37
  - 3.3.5 Control and Data acquisition . . . 38
- 3.4 Injector Operation and Characterization . . . 41
  - 3.4.1 Pellet formation and launching . . . 41

3.4.2 Pellet speed and Ideal gun theory 42
3.4.3 Characterization of the pellet injector 44
3.5 Summary 50

4 Stereoscopic Diagnostics 51
4.1 Introduction 51
4.2 Stereoscopic principle 52
4.3 Pixel correspondence 55
4.4 Instrumentation and Camera Calibration 56
4.4.1 Instrumentation 57
4.4.2 Camera Calibration 58
4.4.3 Application to pellet ablation study 62
4.5 Summary 64

5 Stereoscopic observation of the pellet ablatant in LHD 65
5.1 Introduction 65
5.2 Experimental setup 67
5.3 Experimental Results 70
5.4 Discussions 84
5.4.1 NBI Heating and Fast ion in LHD 84
5.4.2 Rocket Effect and Pellet Toroidal Deflection 87
5.4.3 Field Geometry and Pellet Vertical deflection 91
5.5 Summary 92

6 Pellet injection studies from multiple injection locations 95
6.1 Introduction 95
6.2 Experimental setup 97
6.3 Results and Discussion 99
6.3.1 Low field side pellet injection 100
6.3.2 Inboard high field side pellet injection 106
6.3.3 Plasmoid drift and mass redistribution 114
6.3.4 Pellet fueling efficiency 119
6.4 Summary 121

7 Summary and Conclusion 123

Bibliography 126

List of Figures

1.1 Reactivity for the D-T, D-D and D-He^3. 3
1.2 Cross section of LHD showing horizontal and vertical elongated section. Various coils position, vacuum vessel, and cryostat are also shown. 6

2.1 Schematic of the NGS pellet ablation model 14
2.2 Plasmoid drift mechanism in presence of non-uniform magnetic field. 16
2.3 Contour plot of the pellet penetration as a function of the T_e and V_p. 18
2.4 Poloidal section of LHD showing, (a) Horizontally elongated, (b) Vertically elongated section. A HFS exist under the helical coil, ∇B has four different directions. . 19
2.5 (a) Rotational transform of the LHD **B** field. (b) ∇B structure on the field line throughout the torus indicating the three-dimensionality of the LHD plasma. . . . 20
2.6 Three dimensional view of the $\boldsymbol{E} \times \boldsymbol{B}$ vector direction on the pellet plasmoid for a horizontally elongated outboard section injected pellet (bottom). Projections of the above vector on poloidal plane (Top). Color bar indicates the drift direction within 60 cm expansion of the plasmoid along the toroidal direction. 22
2.7 Projection of $\boldsymbol{E} \times \boldsymbol{B}$ drift direction for vertically elongated inboard injection. 23
2.8 (a) Cross section of the alternative injection location: oblique angle injection close to helical coil. (b) Projected $\boldsymbol{E} \times \boldsymbol{B}$ drift direction for this location. 24

3.1 Schematic view of the punch-mechanism based low speed pellet injector 30
3.2 Phase diagram of H_2 isotope showing solid, liquid and gas phases. Triple point at a temperature of 13.9 K is indicated by the solid diamond symbol. 31
3.3 Vacuum system of pellet injector showing pellet formation region, two stage differential pumping system and gas (fueling and propellant) feed system. 34
3.4 Vacuum characteristics curve for two-stage differential pumping system. 35
3.5 Schematic view of LHD with guide tubes connecting between the pellet injector and various injection ports. 37
3.6 Photo diode signal for both light gates used for the calculation of pellet speed . . . 38
3.7 Block diagrams of the injector control and data acquisition system 39
3.8 LABVIEW based user interface control for the injector remote operation. 40
3.9 Low speed pellet injection mechanism using mechanical punch and pneumatic propellant system. 41

3.10 IGT approximation of pellet speed at different propellant pressure (Solid line). The dashed curve indicates the IGT speed after pressure, P_0, and barrel length, L_0, correction. Solid circles indicating the experimentally observed pellet speed. . . . 44
3.11 Shadow-graphic image of (a) an intact pellet at 348 ms^{-1} and (b) a broken pellet at 380 ms^{-1} taken at inboard side guide tube exit. The circles on both figure indicate the position of pellet / pellet fragments on the image. 45
3.12 Change of pellet speed with propellant pressure at different T_p. 46
3.13 Comparison of V_p at curved guide tube exit with pellet muzzle speed (filled symbols) at different T_p. Pellet speed reduction (%) with muzzle speed (open symbol) . 47
3.14 Intact pellet fraction plotted against injection speed at different T_p. The horizontal bars indicate the bin size of the speed taken to estimate the intact pellet fraction. . . 48
3.15 Comparison of experimentally obtained intact speed (Solid circle) with calculated intact speed (Broken line) at different T_p 49

4.1 Schematic of stereoscopic measurement principle. 54
4.2 Stereoscopic diagnostic setup with fast camera and bundled fiber. 57
4.3 Camera calibration setup. The coordinates X, Y and Z represent the plasma vertical, toroidal, and the pellet injection direction of the plasma, respectively. The epipolar plane corresponding to a world coordinate is also indicated. 58
4.4 Epipolar lines (in right half image) corresponding to a number of points in the left image shows the closeness of the estimated points to the actual points. 61
4.5 (a) Stereo reconstructed error along Z direction (Maximum error ± 18 mm). (b) Error in in $X-Y$ direction for all Z-positions. An error of 10 mm is indicated by the bounding circles of 10 mm radius. 62
4.6 A typical picture of an ablating pellet image taken from two different locations. The epipolar line corresponding to the pellet position in left image is shown on right image 63
4.7 Time evolution of the stereo reconstructed pellet position and H_α ablation intensity. Predicted pellet position by considering the constant pellet speed is indicated by the solid line. The open circles show the stereo reconstructed pellet penetration speed. 63

5.1 (a) Three dimensional view of the LHD plasma with helical coils, (b) Mid-plane top view of pellet injection showing plasma flux surface, pellet injection direction and stereoscopic observation system. (c) Vertical view of injection cross section. Field of view of the camera lenses is shown by the hatched region. 68
5.2 Temporal evolution of a typical pellet injected discharge (# 60825: CW-NBI and # 59515: CCW NBI). Shaded region corresponds to the pellet timing considered in this study. 71
5.3 H_α and camera intensity signal for CW and CCW NBI case. The last closed flux surface (LCFS) and pellet ablation time are indicated by dashed line in both figure. 72
5.4 Loss function $L(E)$ and effective cross-section $\Lambda(E)$ of electrons and ions 73

5.5 (a) & (b) Projection of the magnetic flux surface on the camera image showing elongation of the pellet cloud along the magnetic field lines (solid lines). (b) Change in plasmoid angle with the plasma mid-plane while penetrating into the plasma. (c) Comparison of the pitch of the magnetic field line and the plasmoid angle with the plasma mid-plane, along R. 75
5.6 (Top) Reconstructed pellet trajectory on (a) toroidal (mid-plane view) and (b) vertical plane of the LHD for CW-NBI injection. Shaded area indicates the viewing area of the observation system. Direction of the pellet injection and tangential NBI are indicated by the arrows. (Bottom) The pellet trajectory on (c) toroidal (mid-plane view) and (d) vertical plane, in the case of the CCW-NBI injection. . . 77
5.7 Reconstructed pellet trajectory on (a) toroidal (mid-plane view) and (b) vertical plane of the LHD for CCW-NBI injection. 78
5.8 Histogram (20 pellets for each case) showing the variation of the deflection radius in presence of CW and CCW NBI conditions. Deflection radii of the two discharges analyzed in this study are indicated by the arrows. 79
5.9 Pellet speed along vertical (V_{pol}), toroidal (V_{tor}) and negative major radial (V_{rad}) direction of the plasma for (a) CW and (b) CCW NBI injection.(c) Pellet toroidal acceleration in both NBI conditions, negative acceleration means CW direction. . 80
5.10 Variation of maximum toroidal deflection speed with fast ion collision time. 81
5.11 Time evolution of the pellet penetration in plasma under two NBI conditions. . . . 82
5.12 Radial profiles of T_{e} and n_{e} before and after the pellet injection in the case of CCW NBI plasma. Observed penetration depth is indicated by the vertical dashed line. The difference in two density profiles (Δn_{e}) shows the effective pellet mass deposition. 83
5.13 Pellet ablation profile calculated by using ABLATE code signifies the effect of fast ion on the pellet ablation process. 85
5.14 Formation of a rocket effect due to assymmetric ablation by the fast ions. 86
5.15 Calculated fast ion density profiles along the pellet trajectory. Shaded area corresponds to the bending radius in the cases of CW and CCW NBI conditions. 90
5.16 Comparison of the observed vertical deflection (filled symbols) and poloidal shift (absolute value) of the field lines, calculated from the field line tracing (dashed lines) within the pellet life time at different pellet deflection radii. 93

6.1 Schematic of the pellet injection cross-section for LFS and HFS injection showing, (a) top view of mid-plane and (b) vertical view. Origin of the pellet position (X_{pol}, Y_{tor}, Z_{rad}) inside the vessel is taken at the Lens-2 camera port. The shaded portions (in top figure) represent the viewing area of each camera. 98
6.2 The range of the plasma parameters covered in this experiment. The size of a symbol represents the pellet injection speed in the corresponding speed range. . . . 100
6.3 Waveform of a typical pellet injected discharge for LFS injection showing: (a) H_α ablation light, (b) central electron temperature T_{e0}, (c) plasma stored energy and the port through NBI power, and (d) line averaged electron density $\bar{n}_{\mathrm{e}}$. 101

6.4 Experimental penetration depth plotted against the predicted penetration depth considering the NGS model (electron ablation only). 102
6.5 Temperature dependence of the penetration depth in the density range (1-2) $\times 10^{19}$ m^{-3} in case of low speed and high speed pellets. The solid line indicates the $T_{\mathrm{e}}^{-0.68}$ fitting of the data's. 104
6.6 Radial profiles of the T_{e} and n_{e} obtained from the Thomson scattering diagnostic in the case of (left) low speed (# 104254), and (right) high speed (# 99391) injected pellets. The particle deposition profile, which is the difference in density profile after and before the pellet injection, is shown by the inverted solid triangles. H_{α} ablation light indicating the pellet penetration depth is also shown. 105
6.7 Waveform of a typical pellet injected discharge for alternative injection showing (a) H_{α} ablation light, (b) central electron temperature T_{e0}, (c) Plasma stored energy and the port through NBI power, (d) line averaged electron density $\bar{n}_{\mathrm{e}}$. 107
6.8 Reconstructed pellet trajectory for alternative location injected pellet on (a) vertical plane ($\phi = 23^{\circ}$ section) and (b) toroidal mid-plane of LHD. The shaded area indicates the viewing area of the observation system. (c) Pellet speed in three directions, injection speed and the total speed of the pellet. 108
6.9 Pellet toroidal deflections as a function of the fast ion density ratio. 110
6.10 Maximum toroidal deflection as a function of the ion collision time for the inboard (open diamond) and outboard injection (solid diamonds). 111
6.11 Radial profiles of the T_{e} and n_{e} obtained from the Thomson scattering diagnostic in the case of (left) less CW deflected pellet (# 104237), and (right) CCW deflected pellet (# 102885). The particle deposition profile, which is the difference in the density profile after and before the pellet injection, is shown by the inverted solid triangles. H_{α} ablation light indicating the pellet penetration depth is also shown. . . 113
6.12 Typical fast camera view of an ablating pellet from two different observation points for, (top) outboard LFS and (bottom) inboard HFS. 115
6.13 Typical fast camera image sequence (single view) of an ablating pellet in both type of injection, showing break-away plasmoids drifting in a direction opposite to that of the pellet injection direction 116
6.14 Temporal evolution of the pellet ablation light and the line averaged density for the chords at the boundary ($\bar{n}_{\mathrm{e}}^{\mathrm{b}}$) and core plasma ($\bar{n}_{\mathrm{e}}^{\mathrm{c}}$) 118
6.15 (a) Pellet fueling efficiency as a function of the penetration depth. (b) Degradation of the ε_{f} with the increase in NBI power. 119

List of Tables

1.1 List of LHD diagnostics 8

3.1 Properties of H_2 isotopes 31

Chapter 1

Introduction

1.1 World energy crises

Energy is the vital need for human civilization. The increase in world population impetus the energy demands. At least 50 % increase in demand is expected by the middle of this century, mainly due to the increase in population [1]. Furthermore, according to the Unite Nations, still 1.5 billion peoples in developing countries having no access to the electricity [2]. At present 80 to 90 percent of total worldwide energy is derived from the combustion of the fossil fuels [3]. As the reserves are limited, it is expected that this will last for few hundred years (Oil and gas within the next 50 years and coal within 300 years) [4]. In addition, burning of fossil fuels has adverse impact on the climate change. There are many alternatives to fossil fuels such as biomass, wind power, and solar power etc. However, the large-scale productions of these are limited. Therefore, energy from the nuclear power is a viable solution for future energy crises. Nuclear fission and nuclear fusion are the two forms of the nuclear energy. In the case of the nuclear fission, there are hazards of radiation, and also high risk of the nuclear waste management as these are radioactive in nature with longer half-life period. Nuclear fusion is safer than the nuclear fission, as the nuclear waste from fusion machines will be very less with limited long-term waste disposal requirements. It is also a clean source of energy with almost no environmental impact.

1.2 Nuclear fusion and plasma physics

Nuclear fusion is the process of combining two light nuclei to form a heavier nucleus. During this process the mass difference of the reaction is converted into energy according to the Einstein's relation, $E=mc^2$. In order to induce the fusion of nuclei, it is necessary to overcome the coloumbic repulsion between like charged particles by applying higher energy. Therefore the most promising method of supplying the energy is to heat the reactant to millions of degree Celsius. At this temperature the reactants are fully ionized. The electrostatic charge of the nuclear ions is neutralized by the presence of equal number of electrons, which exhibit a collective behavior and the resulting nuclear gas is called the plasma. To achieve the high temperature needed for nuclear fusion, plasma must be confined so that it does not lose energy and cool. There are numerous mechanisms for plasma confinement, including gravitational (in stars), inertial, and magnetic confinements. However, magnetic confinement is the most favorable, and advanced solution for laboratory scale plasmas to produce thermonuclear fusion in steady state conditions. The leading fusion machines in the field of magnetic confinement are stellarator and tokamak.

The most promising fusion reaction in magnetic confinement is that in which the nuclei of deuterium and tritium fuse to produce an α-particle of energy 3.5 MeV and a neutron of 14.1 MeV. The reactivity cross-section for various fusion reactions is shown in Fig. 1.1. As the reactivity cross-section for D-T reaction is maximum just over 100 keV, this reaction is favorable over other two reactions [5]. The condition necessary to initiate the fusion reaction is defined by the Lawson criteria, which is written as,

$$n\tau_\varepsilon T_\mathrm{e} > 3\times 10^{21}\mathrm{m}^{-3}\mathrm{s\ keV}. \tag{1.1}$$

where, n is the ion density, τ_ε in the energy confinement time and T_e is the electron temperature of the plasma. Therefore, the plasma density and the temperature are important factors for achieving the nuclear fusion.

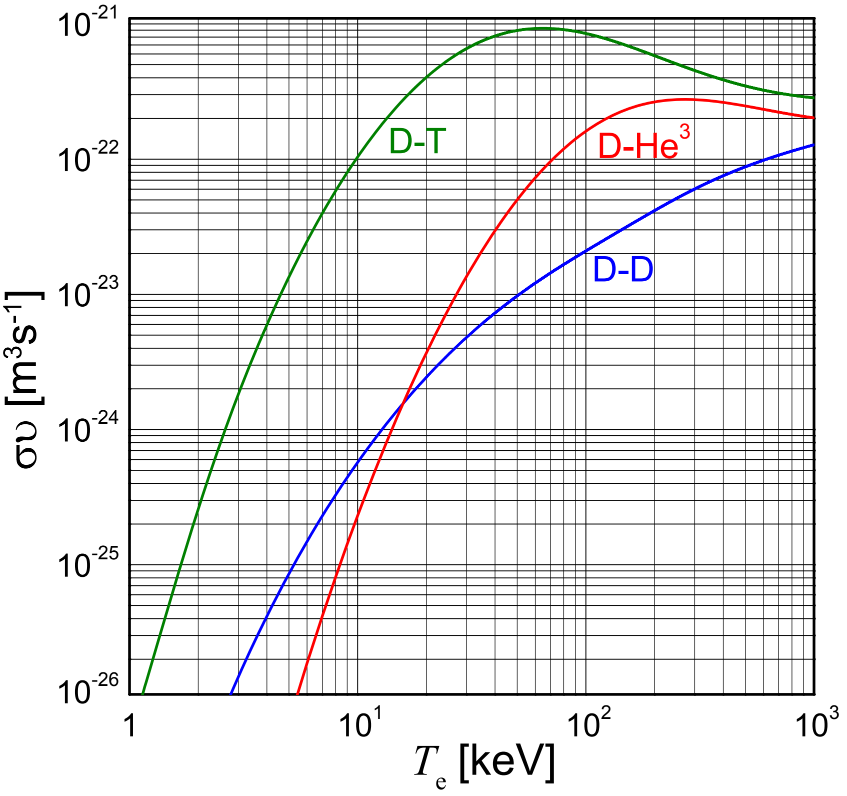

Figure 1.1 Reactivity for the D-T, D-D and D-He^3.

1.3 Plasma fueling and pellet injection

The plasma is formed by ionization of pre-filled gas. After the plasma is formed, it is necessary to maintain the discharge by replenishing the spent fuel. There are several possibilities of refueling the plasma such as gas puff, NBI injection and pellet injection. Although gas puffing is the simplest way of plasma fueling, major concern for this is the low fueling efficiency. The fueling efficiency for the gas puff is less than 20 % in the case of tokamaks using active diverter [6] and the condition worsens for reactor grade machines. Core fueling is necessary for the next generation plasma devices like ITER [7]. Therefore fueling by gas puff is not capable of high-density operation. Besides heating of the plasma, neutral beam can also be used for plasma fueling. However for bigger scale fueling, the particle should be accelerated to very high energies and currents (1 MeV, 40 A), which create technological challenge [8].

In comparison to the above two methods, frozen pellets of the isotopes of Hydrogen at liquid He temperature with speed few hundreds to thousands of ms^{-1} has become the most favorable method for refueling magnetically confined plasmas. The major advantage of this method is the core fueling and peaking of the plasma density profile accomplished by deep penetrated pellets. In addition, power required by this method to inject the fresh fuel is negligible in comparison to the fueling by the neutral beam injection. Using the pellet injection, improved particle and energy confinement properties have been demonstrated by several confinement devices including, Alcator-C [9], DIII-D [10], TFTR [11], ASDEX [12], JET [13], JT-60 [14, 15] and LHD [16]. Enhancement of the plasma performance depends upon the pellet penetration and subsequent deposition of the ablated mass inside it. Concerning with the pellet ablation in the plasma, several models have been proposed on the basis of the neutral gas shielding (NGS) [17] on the ablation characteristics. The advancement of the NGS model considering the additional shielding from the low temperature plasma cloud surrounds the pellet has also been formulated in the form of the neutral gas and plasma shielding (NGPS) model [43]. In the framework of the NGS model, the normalized penetration depth (λ/a) inside the plasma that depends upon the plasma electron density (n_e) and temperature (T_e), and the pellet radius (r_p) and speed (V_p), is given by [107],

$$\frac{\lambda}{a} = 0.079 T_\mathrm{e}^{-5/9} n_\mathrm{e}^{-1/9} r_\mathrm{p}^{5/9} V_\mathrm{p}^{1/3} \tag{1.2}$$

Due to strong dependence of the electron temperature on the pellet penetration, it will be great challenge to fuel the fusion grade plasmas, even if the pellet injection speed can be increased to the possible technological limits.

A discrepancy between the pellet penetration and effective mass deposition depth is reported in tokamaks. This indicates the existence of a redistribution process of the pellet mass, just after the ablation. This redistribution is believed to be due to a drift force down the magnetic field gradient, towards the low field side (LFS) of torus. In tokamaks, this drift expels the deposited matter out of the plasma in the case of LFS pellet injection, while it favors core deposition for the high field side (HFS) injection [102]. With increase in heating power, degradation of the fueling efficiency, observed in case of LFS injection has not been found in HFS fueling. Therefore, it now seems less critical to dispose of high-velocity pellet injectors to fuel a reactor scale device. This enhanced mass deposition profile encourages to use the HFS fueling in ITER [18]. Considering this redistribution process, recent pellet ablation models are aims to predict the exact mass deposition profile inside the plasma with the inclusion of mass drift effect [19]. Apart from use of the pellet for plasma fueling, analysis of pellet trajectory is also used as a diagnostic tool to get the information about the particle transport [20] and q-profile measurement [21]. Recently, small sized Hydrogen pellets are also used to control the ELM frequency in ASDEX-U [22]. Apart from the pellet ablation physics, significant progress has been made in the areas of the pellet injector technology. A detail of the various injection technologies can be found in [62].

1.4 Pellet injection and relevant diagnostics in LHD.

Large Helical Device (LHD), Worlds largest heliotron type plasma device is built with an objective to demonstrate the steady state plasma operation [23]. One of the advantage of this device over tokamak is the current-less, and disruption free plasma. The major radius varies between 3.5 $\leq$ R $\leq$ 4.0 m for different operational conditions. The largest plasma volume is 30 m^3 for the standard configuration of R = 3.6 m. The averaged minor radius is 0.6 m. The magnetic field strength on the plasma axis is up to 3 T. A cross sectional view of LHD is shown in Fig. 1.2. In LHD, magnetic confinement field is generated by l/m = 2/10 continuous helical coils and three set of poloidal coils, where l and m are the toroidal and poloidal pitch numbers, respectively. As the confinement field is generated by external helical coils, the plasma varies elliptically between vertically and horizontally elongated sections. This helical field makes the LHD plasma three-dimensional. The poloidal coil system include sets of; (1) inner vertical (IV), (2) inner shaping (IS), and (3) outer vertical (OV) coils. All the coils are made up of superconductor. Ten pairs of local island diverter (LID) coils are placed at the top and bottom port of the vertically elongated section for edge plasma

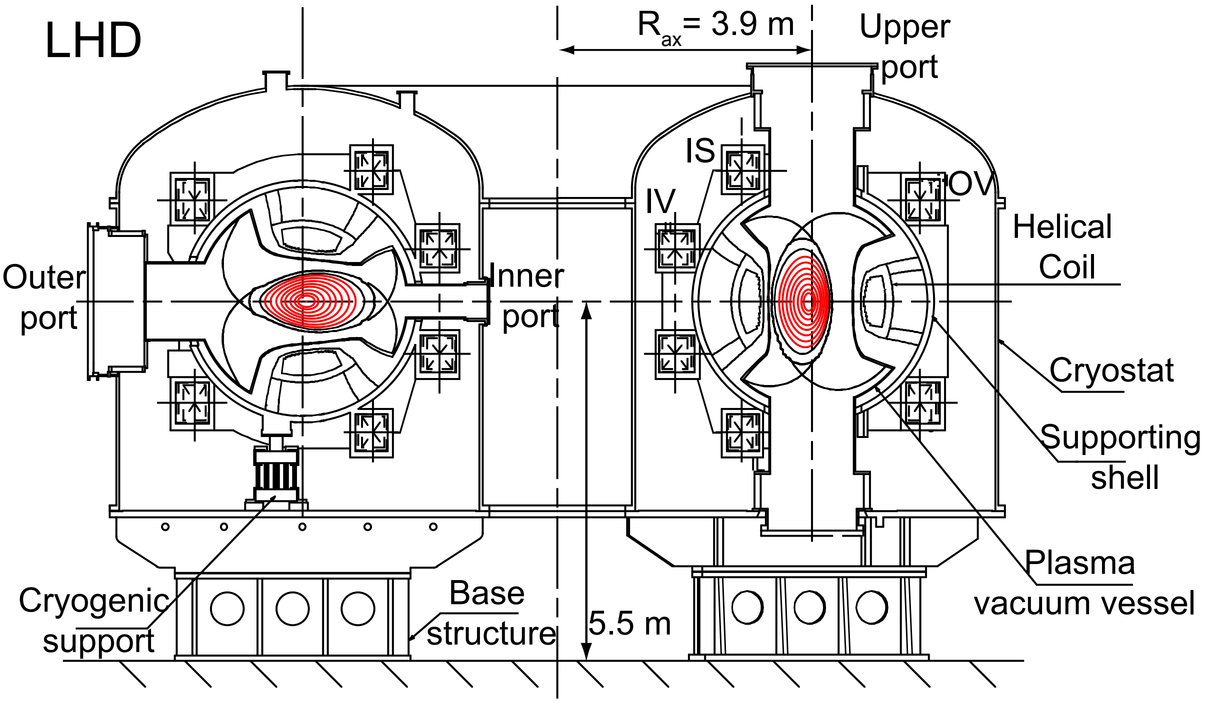

Figure 1.2 Cross section of LHD showing horizontal and vertical elongated section. Various coils position, vacuum vessel, and cryostat are also shown.

control [24]. The LID is a closed diverter that uses m/n =1/1 island. The position of the magnetic axis that fundamentally decides the plasma confinement is changed by the OV and IV coils. The IS coils control the ellipticity of the plasma.

A discharge can be initiated by either electron cyclotron heating (ECH) [25] and/or by neutral beam injection (NBI) [26]. The ECH used for plasma production and heating, is generated by gyrotrons at the characteristic frequency of 84, 82.6 and 168 GHz. Three negative ion based tangentially applied neutral beam injectors are the main heating devices in LHD. Out of these, two injectors are operated in Counter Clock Wise (CCW) direction and the other injector is operated in Clock Wise (CW) direction. Each NBI is designed to inject a 7.5 MW hydrogen beam at energy of 180 keV.

After the initiation of the plasma discharge, external fueling is necessary to maintain the plasma density at a specific level. LHD is equipped with gas puff [27,28] as well as pellet injection

[65] systems for plasma fueling. Using the pellet injection, favorable dependence of the energy confinement on the plasma density has been achieved, which has not been possible by the gas puffing [16]. By using the repetitive pellet injection [29], high density steady state operation has also been demonstrated in LHD [30]. Since, NBI is the main source of the plasma heating in the pellet injected discharges, measurement of the fast ion profile in the plasma is necessary for the pellet ablation studies. The fast ion deposition profiles are evaluated by using the Monte Carlo simulation code, MCNBI [31]. The basic diagnostic systems needed to know the pellet characteristics are light gate system for pellet speed, shadowgraph, and microwave cavity [32] for the pellet intactness and mass measurement. Two light gate systems consist of laser and photo diodes, are installed in the injector to measure the injected pellet speed. A CCD camera with nano second pulsed light is used to capture the pellet image. The pellet shape and mass provide the information about the particle content of the injected pellet into the plasma, which further needed for the fueling efficiency estimation. The H_α and the fast imaging camera diagnostics are installed to analyze the pellet dynamics inside the plasma. The pellet ablation light is measured by a Si-PIN photo diode with a Balmer alpha, H_α filter at a time resolution of 1μs. Stereoscopic diagnostics [80] consisting of two bifurcated imaging fiber and a fast imaging camera is employed to extract the information about an ablating pellet. The image resolution of the camera is more than 100 K pixel. The images are obtained with temporal resolution of 20 μs with 5 to 20 μs exposure times. A high-speed spectroscopic diagnostic, using fast camera and five arm bundled fiber has been installed in LHD to characterize the ionized pellet ablation cloud (plasmoid) in LHD [33]. The spectra of Hydrogen Balmer-lines and background continuum radiation, depend on the electron density and temperature of the plasmoid. Therefore the Balmer-β line (wavelength: 486.1 nm) and continuum (wavelength: 576.8 nm) lines are used to evaluate the density and the temperature of the plasmoid.

While developing the diagnostic systems for LHD, capability to address the key issues such as multi dimensional measurements (because of non-axisymmetricity of the plasma) and operation

Table 1.1 List of LHD diagnostics

Diagnostics	**Measurements**
FIR laser Interferometer	Line integrated n_{e}(r)
Co$_2$ laser Interferometer	High n_{e} plasma measurement
MMW Interferometer	Line-averaged n_{e}
Thomson scattering	T_{e}(r), n_{e}(r)
Electron Cyclotron Emission (ECE)	T_{e}
X- ray pulse height analysis	T_{e}, Impurities
Hard X-ray CCD camera	Two dimensional T_{e} profile
Charge exchange spectroscopy	T_{e}(r), Plasma rotation $(V_{\mathrm{p}}(r), V_{\mathrm{t}}(r))$
Crystal spectrometer	T_{e}, V_{t}
UV and Visible spectrometer	Impurity, n_0(H), Z_{eff}
Bolometry	P_{rad}(r)
TESPEL	Particle transport
CXS	Poloidal rotation speed
Heavy Ion Beam Probe (HIBP)	Φ_{p}(r), Φ_{p} fluctuation
SXR CCD camera	Shafranov shift
Diamond and Silicon detectors	Neutral particles
Magnetic probe	I_{p}, W_{p}
Langmuir probe	Edge T_{e}, n_{e}, Φ_{p}
Visible / Infrared camera	Plasma-wall interaction
Diverter spectroscopy	Recycling and particle influx

in steady state conditions, are taken into consideration. Another big issue in diagnostics is the handling of huge amounts of data. The following physics issues while developing the diagnostics are considered for fulfilling the LHD missions; diagnostics for (a) High $n\tau_E T_e$ plasmas and transport physics, (b) Magnetohydrodynamics (MHD) equilibrium and stability, (c) Long pulse operation and diverter function, and (d) confinement for energetic particles. A list of important diagnostic systems in LHD is tabulated in Table 1.1. A detail knowledge of the LHD diagnostic systems can be found else where [34]

The effect of pellet injection on the plasma performance is analyzed by the electron temperature (T_e) and density (n_e) of the plasma. Line integrated n_e is measured by the 13 channel FIR laser interferometer [35], positioned at a vertically elongated plasma section. High time resolved datas (up-to 1 μs) can be obtained from this diagnostic and it is useful for the analysis of the mass redistribution process in a pellet-injected discharge. The radial density profile can be obtained by the Abel inversion technique [36]. A CO_2 laser imaging interferometer is installed on the LHD to measure the density profile, without phase jump during high density ($n_e > 10^{20}$ m^{-3}) plasma operation. A two color MMW interferometer [37] is installed to measure the n$_e$, along the central chord on horizontally elongated section. Thomson scattering diagnostic is a useful system to obtain the plasma electron density and temperature profile, locally. This diagnostic is installed on a horizontally elongated mid-plane section in LHD [38]. As this diagnostic adopts an obliquely back scattering system, it is possible to measure the whole plasma region along the major radius on the mid-plane R, under the severe port constraint of the helical configuration. It can measure datas from 200 points radially with a spatial resolution of 15- 30 mm, which depends on the radial position of laser scattering. The plasma-stored energy (W_p) is obtained by the diamagnetic loops, which in turn is used for the estimation of the energy confinement time.

1.5 Objective of this thesis

This thesis is focused on the global issues of the pellet fueling studies, such as pellet ablation and particle redistribution process in the LHD. The questions concerning the ablation dynamics are : what is the effect of the energetic ions on the pellet ablation process? How does the three-dimensionality of the plasma affect the pellet penetration characteristics? From the viewpoint of the fueling efficiency, is it possible to demonstrate the improved fueling scenarios in LHD considering the magnetic field structure of the injection location, as observed in tokamaks?

The pellet ablation process is regulated by the local plasma parameters such as density, electron temperature. Due to its strong dependence, pellet penetration decreases significantly with the increase in T_e. This penetration loss affects the fueling efficiency (ε_f). With the increase in heating power, degradation of the ε_f has also been reported in tokamak [85]. The generation of the energetic particles due to the external heating can strongly affect the ablation dynamics. Not only it enhances the ablation but also an asymmetry can gives rise to deflection of the pellet from its initial trajectory. In LHD, neutral beam injection (NBI) is the major source of the plasma heating in the pellet injected discharges, and hence the generation of the fast ions is significant. A two dimensional deflection of the pellet trajectory in presence of the NBI has been reported earlier in LHD [91]. Since, LHD plasma has the three-dimensional characteristics, a 3D interaction between the pellet and the plasma cannot be ruled out. Therefore an extensive study of the effect of the fast ions on the pellet ablation dynamics is one of the objectives of this thesis.

Another important aspect of the pellet fueling is the effective mass deposition. The fuelling efficiency is not only affected by the pellet penetration into the plasma, but also depends upon the mass redistribution owing to the field gradient of the injection location. In concern to this, enhanced fueling efficiencies have been reported in tokamaks for HFS injection in comparison to the LFS injection [102]. Similar to that of the tokamak results, outward distribution of the pellet mass has also been found in LHD for LFS pellet injection. Due to lack of proper diagnostics, it is premature to conclude the pellet injection characteristics for the coil side injection (HFS) performed earlier in LHD [91]. In that study, although there is no outward redistribution of the pellet mass has been reported; due to lack of the local density measurements, it has not been possible to demonstrate the fueling behavior quantitatively. Therefore a part of work in this thesis is aimed at exploring the alternative injection scenarios for better particle deposition profiles in LHD. Since the HFS resides under the helical coil, an alternative approach to access the HFS is considered. In this approach a pellet is injected from the inboard LFS location obliquely to a region, close to the helical coil.

To support the experimental objectives, a low speed pellet injector and a fast 3D imaging diagnostic system have been developed. The proposed HFS injection location is situated at the inboard side of the torus. In order to deliver an intact pellet through the bended guide tube, a low speed pellet injection system (100-400 ms^{-1}) using a mechanical punch device is developed. To study the 3D pellet-plasma interaction, a three-dimensional diagnostic is necessary. Since the perpendicular observations are restricted by the helical coils in LHD, a three-dimensional imaging diagnostic by applying the stereoscopic principle is calibrated. This diagnostic uses a fast camera and bifurcated imaging fiber. Not only the trajectory of the pellet but also the mass deposition characteristics can be studied by analyzing the individual image frames.

1.6 Outline of thesis

After introducing the first chapter (this chapter), Chapter-2 describes about the pellet ablation dynamics inside the plasma, and injection position optimization in LHD. In Chapter-3, development of a low speed pellet injector, and injection test of the pellet through the bended guide tube is presented. Calibration of the three-dimensional measurement diagnostic basing on the stereoscopic principle is discussed in Chapter-4. In Chapter-5 three-dimensional observation of the pellet ablation behavior in presence of the fast ions is discussed. Then, Chapter-6 describes the results regarding the pellet fueling and mass redistribution for the different pellet injection locations in LHD. Finally, the summary and conclusions are given in the Chapter-7.

Chapter 2

Pellet fueling scenarios in helical system

2.1 Introduction

The success of a future fusion reactor implicitly depends on the efficient fueling, which is possible by the pellet injection. In several fusion machines including the tokamak and the helical device, extended operational limits have been achieved, which has not been possible by the gas puffing [10, 16]. After the pellet enters in to the plasma, change of phase from a solid material to the mass deposition lasts for few milli-second. The overall pellet dynamics during this time can be divided into two parts, such as ablation and mass homogenization. In context with this, the successful prediction of the pellet dynamics inside the plasma is necessary. Although it has been proven as a favorable candidate for fueling, outward redistribution of the deposited mass [40] for the low field side (LFS) pellet injection is a major concern. On the other hand, for the high field side (HFS) injection, enhanced fueling efficiency (ε_{f}) has been observed in tokamak [41]. The basic question arises here is, whether the success of the HFS injection in the tokamak can be extended to the helical plasmas, which is different from the former by its three dimensional helical magnetic field. In this chapter we will discuss about these issues and will extend the global understanding in this regard to explore the favorable pellet injection locations in LHD.

2.2 Pellet ablation

Soon after a pellet enters into the plasma, it is exposed to the heat flux, carried out by the plasma electrons and ions. If the electron and the ion temperatures are equal, the electron heat flux is dominated owing to the ratio of the electron and ion mass ratio $\sqrt{(}m_\mathrm{i}/m_\mathrm{e})$, where m_i and m_e are the ion and electron masses, respectively. The pellet starts to evaporate and forms a spherical neutral cloud around it. This ablation cloud shields the pellet from the incident heat flux and hence the pellet lifetime is increased. After the formation of the neutral cloud, it is further heated and ionized, and forms a high density, low temperature ionized plasma cloud, called plasmoid. The plasmoid having high pressure inside it expands along the magnetic field line until the pressure equilibrium with the background plasma. A diagram illustrating the ablation phase is shown in Fig. 2.1. In this figure R_ax, V_p, $\boldsymbol{B}_\phi$ and a, represent the magnetic axis, injected pellet speed, toroidal magnetic field and minor radius of the plasma, respectively. The pellet penetration at a particular time from the plasma edge is represented by λ. The descriptions presented here is the simplest form of the neutral gas shielding (NGS) model [17]. This model has been systematically

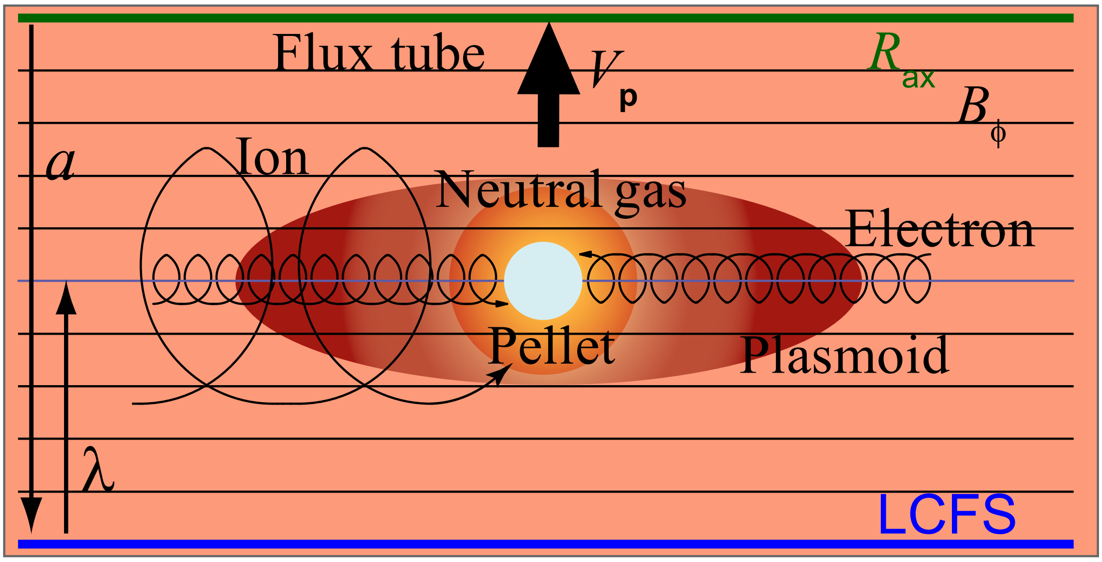

Figure 2.1 Schematic of the NGS pellet ablation model

modified by many researchers taking into account of various aspects such as Maxwellian electron distribution and geometrical effect [42], shielding from the ionized cloud (NGPS model) [43], and considering the atomic processes [44] . In the original pellet ablation model, the heat flux due to the electrons is only considered. In the discharges with significantly higher external heating power, the ablation rate is strongly modified by the high-energy particles. Therefore the original NGS model is latter extended by Milora [45] and Nakamura [46], taking into account of the effect of fast ions on the ablation process. While considering the energetic particle ablation, it is important to consider the effect from pitch angle and the Larmor radius of the incident flux particles. The effect of the fast ions and its asymmetry surrounding the pellet, on the ablation process is discussed in latter chapters.

The efficiency of the fueling improves with the increase in pellet penetration depth. If the pellet is completely ablated inside the plasma, then, ε_f close to 100% is expected. However, the fueling efficiency well below this value has been found in experiments. The experimental results indicate that the particle deposition depth is lesser than the the pellet penetration depth in the case of the LFS injection. Therefore the pellet penetration is not the end of the process, and there exist some other mechanisms that cause the degradation of the fueling efficiency by removing the particles out of the plasma.

2.3 Mass homogenization

After the ionization of the neutral cloud, the spherical cloud becomes a cigar shaped plasmoid and expands along the magnetic field lines. The expansion speed of the ablatant is much lower than that of the incoming heat flux. Therefore the energy density in the ablation cloud is rapidly increased over the ambient plasma pressure, and a localized high-β plasmoid is formed [47]. The expansion of the ionized cloud continues up-to the pressure equilibrium with the background plasma. The mass homogenization process across the flux surfaces occurs in this phase. The ionized particles at this stage move across the magnetic field due to the $\boldsymbol{E} \times \boldsymbol{B}$ drift force in its self-consistent electric field. There are several possibilities for the formation of these fields in the pellet cloud [48]. One of the possibilities is, the formation of the electric field due to the gradient in the toroidal magnetic field. The above said drift force affects the final mass deposition process significantly by pushing the plasmoid towards the LFS of the torus. The simplified physical picture of $\boldsymbol{E} \times \boldsymbol{B}$ drift model is shown in Fig. 2.2. Let us consider an isolated ionized ablation cloud in the non-uniform

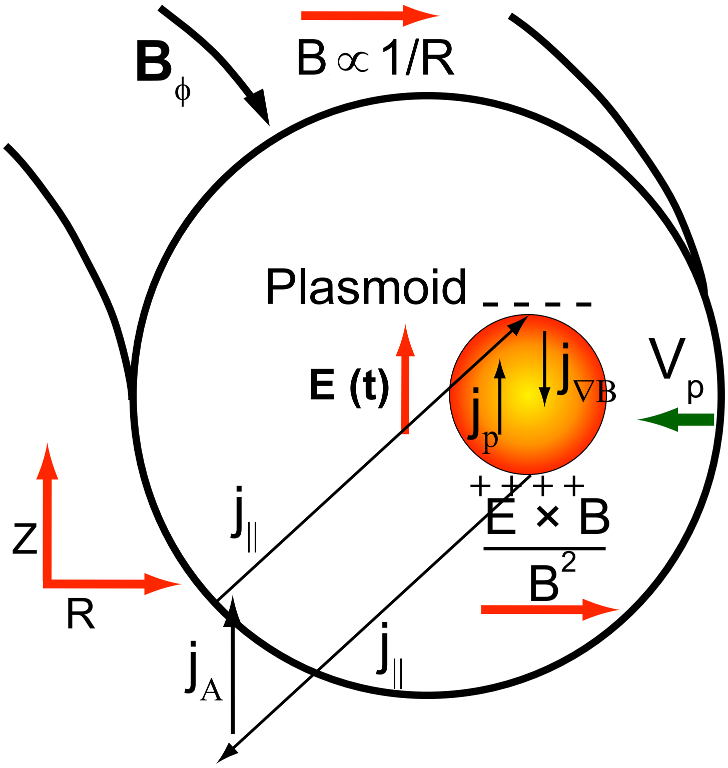

Figure 2.2 Plasmoid drift mechanism in presence of non-uniform magnetic field.

magnetic field, which is proportional to $1/R$. The cloud is assumed to has the constant electron and ion temperature, which are much less than the ambient one. The polarization of such a cloud arises due to the ∇B drift of ions and electrons in the vertical direction. The corresponding vertical current is,

$$j_{\nabla B} = \frac{2p}{RB}. \tag{2.1}$$

Where, $p = n_{\mathrm{I}}(T_{\mathrm{e}} + T_{\mathrm{i}})$, is the cloud pressure. When the ionized particles start to decelerate due to the particle's gyro-motion, the drift velocity reduces and the polarization current arises. The polarization current in the vertical direction is opposite to the ∇B drift current, and is written as,

$$j_{\mathrm{p}} = \frac{n_{\mathrm{i}} m_{\mathrm{i}}}{B^2} \frac{\partial E_{\mathrm{z}}}{\partial t}, \tag{2.2}$$

where n_{i} and m_{i} are the local density and mass of the injected ions, and E_{z} is the vertical electric field due to the polarization of the cloud. However, if the polarization current exists, there should be another current system to close the circuit. Such a current system flows in the ambient plasma. If the currents in the ambient plasma are large enough to compensate the polarization current inside the cloud, the polarization inside the cloud reduces and hence E_{y} field reduces. This electric field generates the $\boldsymbol{E} \times \boldsymbol{B}$ drift force towards LFS of the torus. Consider, there exists an isolated plasmoid at the beginning of the drift, so that the net current inside it is zero ($\nabla \cdot I = 0$). At this condition, two opposite current balances each other. Equating the Eqns. 2.1 and 2.2, the acceleration of the cloud can be written as,

$$m_{\mathrm{i}} \frac{\partial V_{\mathrm{R}}}{\partial t} = \frac{2(T_{\mathrm{e}} + T_{\mathrm{i}})}{R}, \tag{2.3}$$

where $V_{\mathrm{R}} = \frac{E \times B}{B^2}$ is a drift velocity. This drift acts down the magnetic field gradient towards the LFS of the torus. Therefore if a pellet is injected from the low field side, due to this force, the mass is drifted out of the plasma and the fueling efficiency is low. Similarly for the HFS injection, the deposited mass drifts toward the axis of the plasma, and causes high fueling efficiency. It had been reported in several machines that the observed drift is smaller than what can be deduced from the calculation of the drift velocity, and the time scale of the mass homogenization. Various possibilities for the drift compensation like, Alfvén wave generation and overlapping of flux tubes after the plasmoid expands half a toroidal turn along the field line, tends to compensate the polarization field and hence the drift, are proposed in the modeling studies [70].

From the NGS scaling law for the pellet penetration (Eqn. 1.2), it can be seen that there is a strong dependence of the pellet penetration on plasma electron temperature over the pellet injection speed. Contours plot for the pellet penetration as a function of the T_e and the pellet injection velocity (V_p) for LHD is shown in Fig. 2.3. The open circles in the figure represent the points with seven fold increase in the plasma temperature and speed of the pellet. In this calculation n_e and r_p are 1×10^{20} m^{-3} and 3 mm, respectively. From the figure, it can be observed that for a seven folds increase in the injection speed, pellet penetration (λ/a) just increases by 2 times. However, for a similar increase in T_e, λ/a decreases more than three times. At this temperature, if the speed is increased up-to 3 kms^{-1}, the normalized penetration is still less than 0.3. Therefore, it will be a great challenge to fuel the reactor scale plasmas with bigger volume and higher T_e, within the technological limit of the pellet injection speed. In contrast, a better fueling efficiency can be achieved even with lower injection speed by using the HFS of the torus, owing to the mass

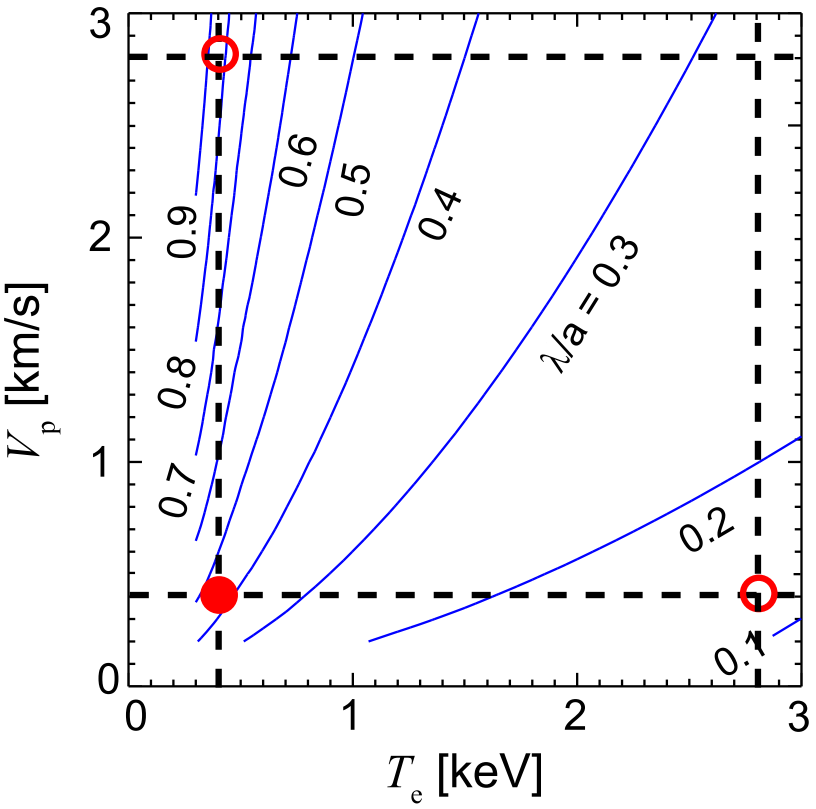

Figure 2.3 Contour plot of the pellet penetration as a function of the T_e and V_p.

drift effect discussed above. Therefore, optimization of the fueling location is necessary in order to achieve higher fueling. The above discussed $\boldsymbol{E} \times \boldsymbol{B}$ drift effect can be used as a tool for the optimization of the fueling location in fusion devices.

2.4 LHD and ∇B structure

In LHD, since the helical modulation is superimposed to the toroidicity, additional high field side appears under the helical coil and varies from one location to other, hence the HFS side is not always inboard to the vacuum vessel as in the case of a tokamak. Therefore, one cannot simplify the magnetic field strength distribution like $B \propto 1/R$ as in axis symmetric tokamak field. The shape of the plasma in LHD varies elliptically between horizontally and vertically elongated cross-sections. The magnetic field structure of the LHD showing HFS and LFS for the above cross sections, and the ∇B directions is shown in Fig. 2.4. It can be observed from the figure that in each cross-section there exist four different directions of ∇B. A complementary study, focusing on the

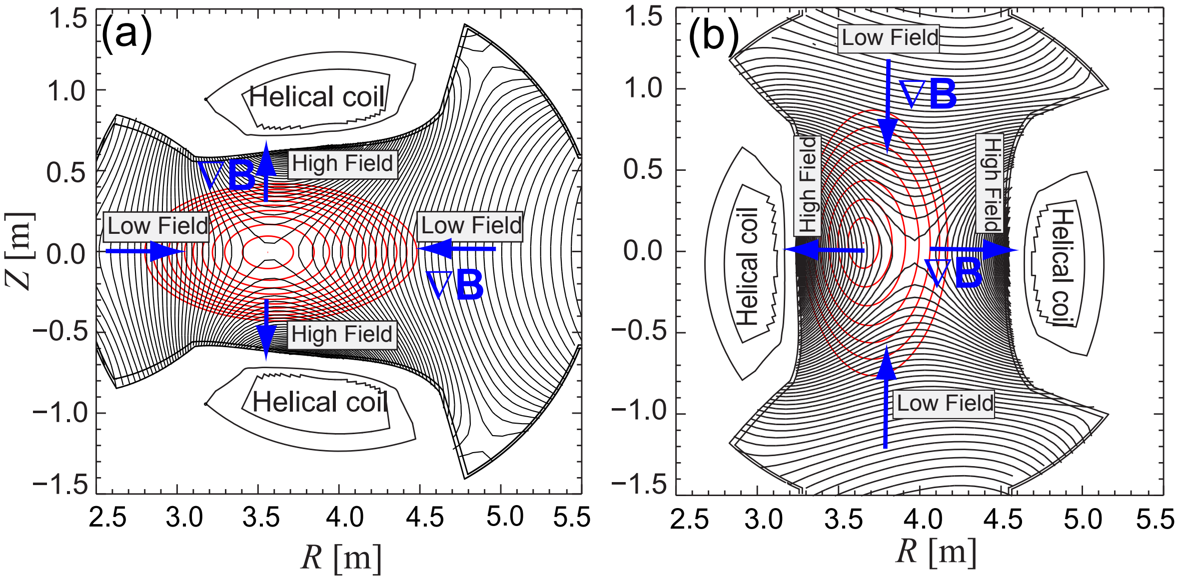

Figure 2.4 Poloidal section of LHD showing, (a) Horizontally elongated, (b) Vertically elongated section. A HFS exist under the helical coil, ∇B has four different directions.

differences of the magnetic field configuration between the helical device and tokamak, is one of the approaches to understand the effect of the plasmoid drift on the fueling efficiency in LHD.

Since, magnetic confinement field is generated by the external helical coils, LHD has high rotational transform at the edge. Figure 2.5(a) shows the rotational transform for $R_{\mathrm{ax}} = 3.6$ and 3.75 m. This indicates that the rate of change of the magnetic field on the edge region is very high and is less for inner region of the plasma. Considering a pellet plasmoid exists in the plasma, a magnetic field line is traced from the plasmoid position along the toroidal direction. The position of this field line on the poloidal plane, and the direction of the ∇B on this line for each toroidal angle are calculated. A field line trace starting from the $\rho = 0.9$ at the outboard low field side (mid plane) is shown in Fig. 2.5(b). In the figure the tail point of the vector shows the position of the field line in poloidal plane and the vector indicates the direction of the magnetic field gradient on the field line. The magnitude of the vector represents the strength of the field gradient. A coordinate system indicating various directions is also shown in the figure. For each toroidal rotation, ∇B

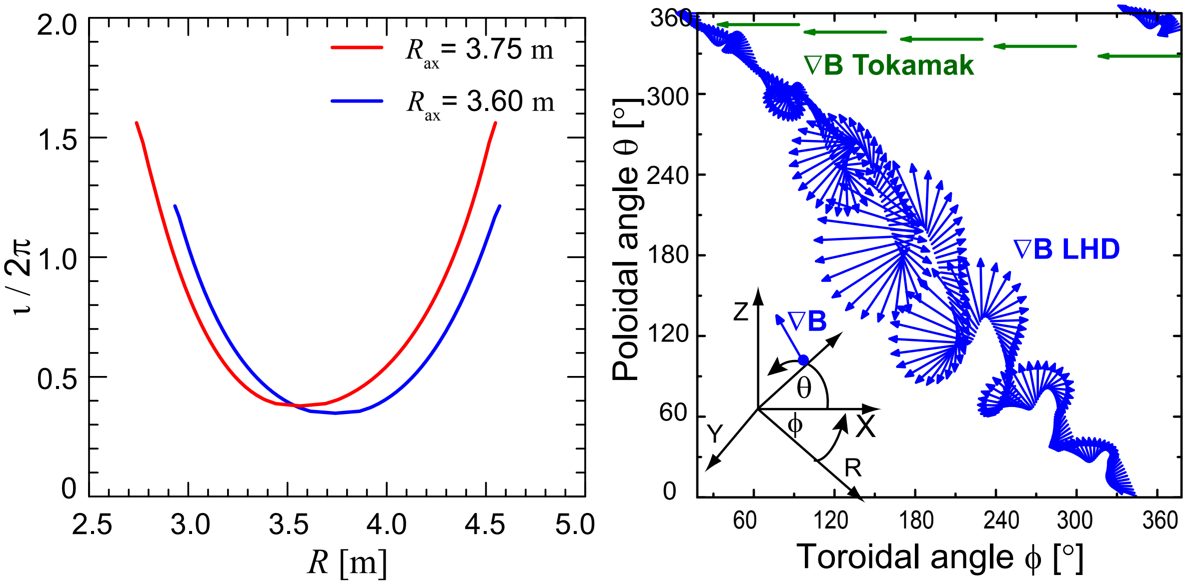

Figure 2.5 (a) Rotational transform of the LHD **B** field. (b) ∇B structure on the field line throughout the torus indicating the three-dimensionality of the LHD plasma.

makes 9 rotations poloidally, and also the poloidal position variation rate is high. A comparison for the case of an equivalent aspect ratio tokamak for the same ρ value represented by the green arrows indicates that, ∇B direction is always towards inboard side of the torus and there is a little variation of it. Due to the high rotational transform at the edge of the plasma, a possibility for drift compensation due to the overlapping of the polarized charges (as discussed in ref. [48]) cannot be ruled out. Therefore it may lead to less drift of the pellet by reducing the E field inside the plasmoid. This discussion of the ∇B structure signifies the necessity to optimize an injection location for the pellet fueling studies, considering the ∇B drift in LHD.

2.5 Injection position optimization

It has been stated earlier that, owing to the plasmoid drift down the magnetic field gradient, enhanced ε_{f} has been reported in tokomkas for the HFS injection. To explore the HFS injection scenarios and enhanced fueling properties in LHD, various pellet injection positions are considered. The injection positions are decided by considering the effect of the $\boldsymbol{E} \times \boldsymbol{B}$ drift on the pellet plasmoid for the corresponding injection locations [49]. To decide an injection location, at first a probable injection direction was chosen. A discrete set of points on the direction of the injection is presumed. A plasmoid is assumed to be at these points, just after the ablating pellet leaves it behind on its injection path. Expansion of the plasmoid from that point along the toroidal magnetic field direction is considered. The ∇B structure and hence the $\boldsymbol{E} \times \boldsymbol{B}$ force on the transverse direction following the field line is estimated. The complete procedure of this calculation for a horizontally elongated outboard side mid plane location is shown in Fig. 2.6. In the bottom figure, the origin corresponds to the center of the vacuum vessel. The plasma axis with the field line and the direction of the injected pellet for the above injection location are also shown. An expanding plasmoid along the toroidal direction and the force on it (vector arrows) in a direction opposite to the injection direction (V_{p}), are indicated in the figure. The calculated force vectors then projected on to the poloidal plane of the plasma. The projected force vectors for the injection location on

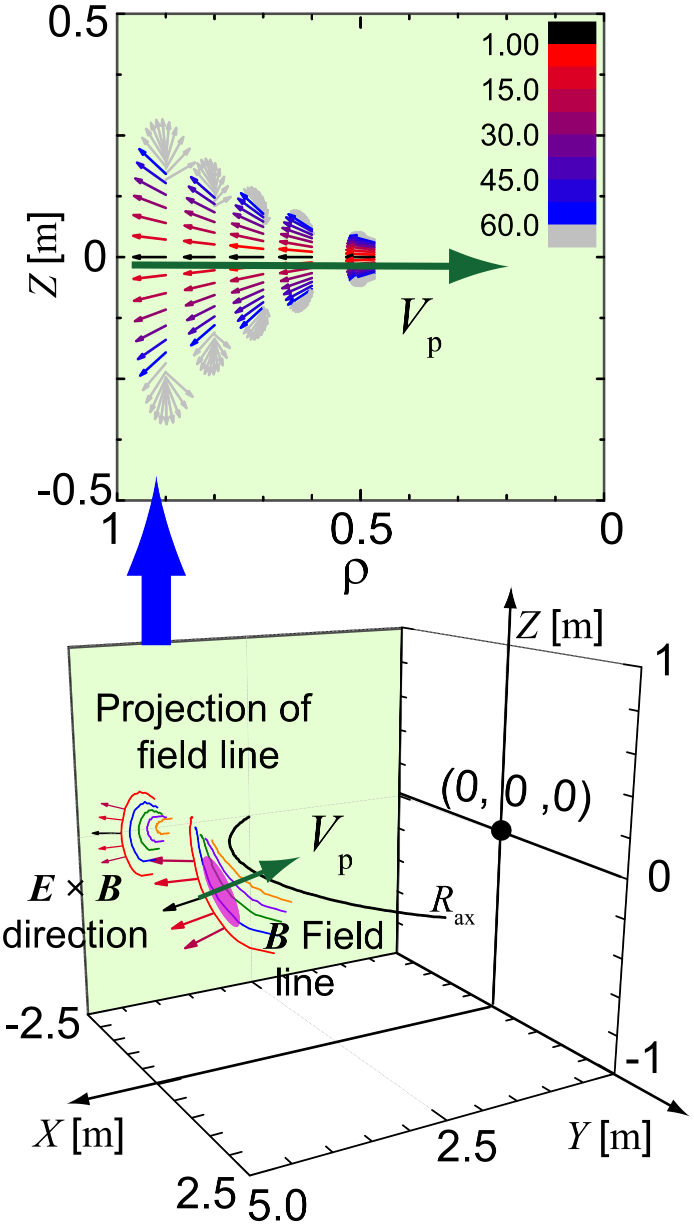

Figure 2.6 Three dimensional view of the $\boldsymbol{E} \times \boldsymbol{B}$ vector direction on the pellet plasmoid for a horizontally elongated outboard section injected pellet (bottom). Projections of the above vector on poloidal plane (Top). Color bar indicates the drift direction within 60 cm expansion of the plasmoid along the toroidal direction.

$\rho - Z$ plane are plotted on top of the figure (Fig. 2.6). The color arrows in the figure indicate the 60 cm expansion of the pellet plasmoid (maximum elongation observed in LHD) along the toroidal direction. The pellet injection direction towards the center of the plasma is also shown. It can be observe that the $\boldsymbol{E} \times \boldsymbol{B}$ force is outward direction to that of the plasma and in-fact this is the LFS location in LHD. The magnetic field structure of this location can be seen in Fig. 2.4(a). Similarly a calculation for horizontally elongated inboard mid-plane has the similar features, and is a LFS injection. The calculation for inboard coil-side at a vertically elongated section is shown in Fig. 2.7. It can be seen that this injection position has significant drift towards the center of the plasma and seems to be the best location to study the HFS injection characteristics. Since this injection location lies under the helical coil, it is impossible to inject a pellet from this location. Therefore in an alternative approach, injection of the pellet from the inboard low field side with an oblique angle to a location close to the helical coil has been considered. The injection geometry

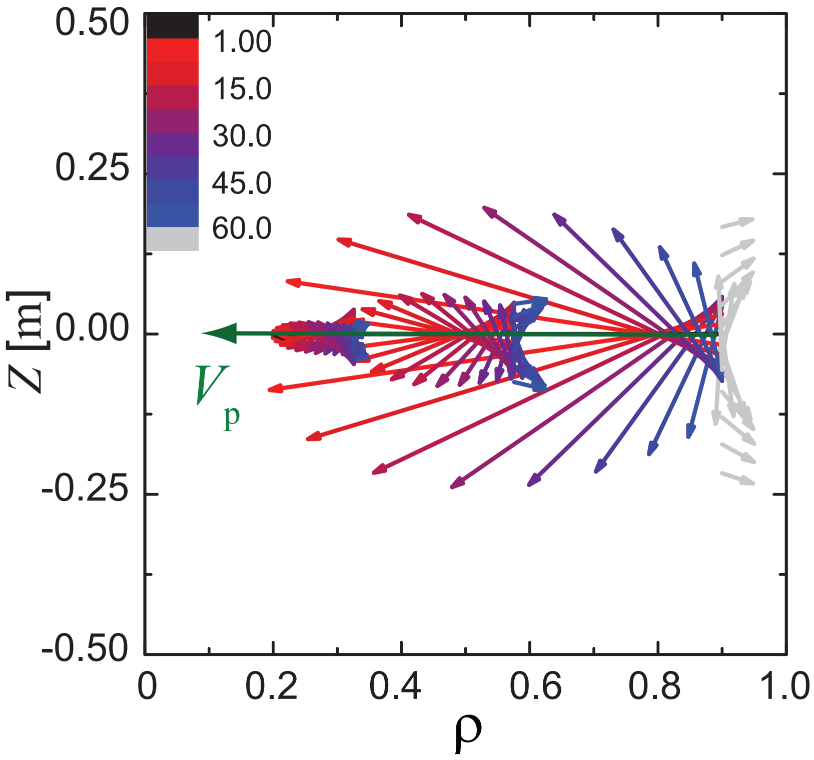

Figure 2.7 Projection of $\boldsymbol{E} \times \boldsymbol{B}$ drift direction for vertically elongated inboard injection.

and the drift force corresponding to this injection scheme are shown in Fig. 2.8. In this figure, the

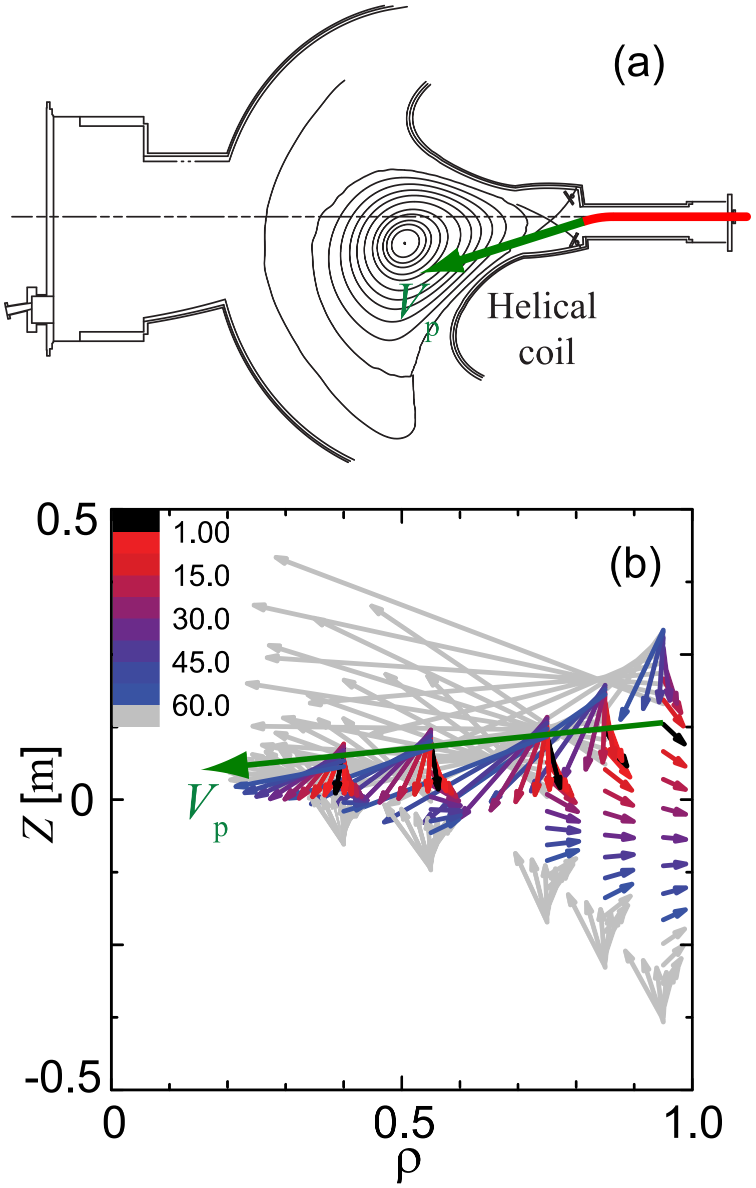

Figure 2.8 (a) Cross section of the alternative injection location: oblique angle injection close to helical coil. (b) Projected $\boldsymbol{E} \times \boldsymbol{B}$ drift direction for this location.

upper one represents the cross section of the plasma (51° horizontally elongated, inboard), where the calculation has been performed. The solid arrow shows the pellet injection direction from the exit of the in-vessel guide tube. The position of the helical coil proximity to the pellet path is also indicated. The calculation result indicates that there is a significant drift force on the pellet plasmoid towards the center of the plasma. Therefore, fueling properties similar to that of the HFS fueling in a tokamak is expected for this injection location. Relying this calculation, another injection position for HFS can be considered is vertically elongated shallow angle upper port injection to a region close to the helical coil. Basing on theses calculations, two injection possibilities are considered for the experiment; (1) Horizontally elongated outer port injection and (2) Horizontally elongated, oblique angle inner port injection. While first one is the LFS injection, the second location considered is the HFS injection location in LHD. To inject a pellet other than outboard side of the torus, long curved guide tubes are needed. During the passage of the pellet inside the guide tube, a stress is exerted on the pellet surface due to its reflection by repetitive collision, and curvature of the guide tube. At higher injection speed, when this stress exceeds the tensile strength limit, there is a possibility the pellet can break. Therefore, a low speed pellet injector is necessary for inboard side injection. Development of the low speed pellet injector and the characterization of the pellet inside the guide tube are detailed in next chapter.

2.6 Summary

The pellet ablation process inside the plasma mainly depends on the electron heat flux on the pellet surface owing to the lesser mass of the electron. The heat flux on to the pellet surface is carried out by the charge particles following the magnetic field. Although, the ablation is governed by the electron heat flux, the presence of the high-energy particles can significantly affect the ablation dynamics. The ablation process inside the plasma can be successfully explained by using the NGS model. From the theoretical point of view, globally observed mass deposition discrepancy is supposed to be due to the $\boldsymbol{E} \times \boldsymbol{B}$ drift force on the pellet plasmoid down the magnetic field gradient of the torus. Owing to this drift, better deposition profile for the HFS injected pellet is demonstrated in tokamak. To explore the enhanced fueling characteristics in the LHD, several injection location around the torus are decided. Since, an ideal HFS exists under the helical in

LHD, injection of a pellet from this location in restricted. To access a HFS location, an alternative approach by injecting a pellet with an oblique angle close to the helical coil has been considered. Considering the ∇B structure of the injection location, a simple calculation of $\boldsymbol{E} \times \boldsymbol{B}$ force on the pellet plasmoid for several injection location is performed and subsequently an injection location is fixed for the experiment.

Chapter 3

Development and characterizations of a low-speed pellet injector

3.1 Introduction

Plasma fueling by pellet injection has extended the operational limit of the fusion machines, which has not been possible by the gas puffing. Developments in the field of the pellet injection technologies have been progressed significantly in the past years. At present, most of the advanced fusion machines like TFTR [50], DIII-D [51, 52], JET [53], ASDEX-U [54], Tore Supra, JT-60 [55] and LHD [56] are equipped with the pellet injectors. Delivery of a pellet into the plasma can be divided into three parts. These are pellet freezing, acceleration, and successful delivery into the plasma. The most common types of freezing techniques used are, *in-situ* pipe gun in case of single pellet or extrusion techniques in case of continuous pellet formation. The leading techniques for pellet acceleration are light gas gun [57] and the centrifuge [58]. Using these techniques pellet speed up-to 1 kms^{-1} or more has been achieved. For very high-speed pellet injection two stage light gas gun is an useful method and the speed up-to 3.5 kms^{-1} has also been reported [59]. Repetitive pellet injectors are developed for plasma fueling in case of steady state operation. In the case of the pellet injected through the straight tube, it is possible to inject a pellet with high-speed. However, the injection of a pellet through the bended tube needs a low speed pellet injection system due to the fracture of the pellet while passing through it. For low speed pellet injection, punch mechanism based technology is a favorable method [60, 61]. Conclusively pellet injectors of injection speed ranging from hundreds of ms^{-1} to few kms $^{-1}$ are operational world wide as per the necessity. A review of the pellet injection technologies can be found elsewhere [62]

Concerning the fueling issues, we want to inject a pellet from the selected locations around the torus in the LHD. The pellets were transferred to these locations through the curved guide tubes. Therefore, the pellet speed should be low in-order to be delivered intact within the curved guide tubes. Considering this fact, a low speed injection system using the mechanical punch method has been developed [106] for alternative location (inboard oblique angle coil side) pellet injection studies in the LHD. In this chapter a detailed design and performance of this pellet injection system is discussed in following sections.

3.2 Design Criteria

The criteria that lead to the eventual design of this injector are

(1) Lower injection speed through curved tube.

(2) Remote operation

The objective of the development of this injector is to carry out the pellet injection from the different injection locations (as discussed in previous chapter) in LHD. An injection location other than outboard side of the torus needs a curved guide tube for pellet transfer, and deterioration of the pellet inside it limits the use of a high-speed pellet injector [64]. Therefore the use of existing high-speed multi barrel pellet injector is limited in LHD, which is used for regular plasma operations by injecting a pellet from the horizontally elongated outboard side of the torus at a speed $\approx$1000 - 1200 ms^{-1} [65]. A pellet needs high pressure to break away from the freezing area inside the barrel. The use of higher pressure accelerates the pellet to high-speed and hence low speed injection, which is the primary objective for the pellet launching through the bended tubes is not feasible. Considering this, a solenoid operated mechanical punch device used at the breach side of the injector seems to be a favorable solution for low speed pellet injection [60]. A pellet can be injected with the combined operation of a mechanical punch and a small amount of propellant gas. In addition, using this method the requirement of a propellant gas is also minimized and hence, it helps to reduce the overall dimensions of the injector. The small amount of propellant gas needed to accelerate the pellet can be removed easily from the injection line. Therefore using the mechanical punch device, a low-speed pellet injector of speed $\approx$100 - 400 ms^{-1} and with the flexibility of pellet injection at a desired speed has been designed for alternative location pellet injection in LHD. Higher injection speed is also possible for higher propellant pressure but the pellet speed during the experiment is limited by considering the intactness of the pellet after passing through the transfer line.

A further criterion for the injector is the remote operation. The LHD experimental hall is not accessible during the plasma operation; therefore the vacuum system including valves and pumps should be operated remotely. Additionally the time difference between two consecutive discharges in LHD is only 180 s, hence the pellet formation and injection require a flexible and effective control that should be synchronized with the LHD plasma discharge.

3.3 Design of the pellet injector

The schematic of the low speed pellet injector with various parts is shown in Fig. 3.1. In following sub-sections a detailed design of the various parts of pellet injector is presented.

3.3.1 Properties of Hydrogen isotopes

Commonly pellets of isotopes of Hydrogen are used for plasma fueling studies. The properties of various isotopes of H_2 at cryogenic temperature are tabulated in Table 3.1. This study is focused

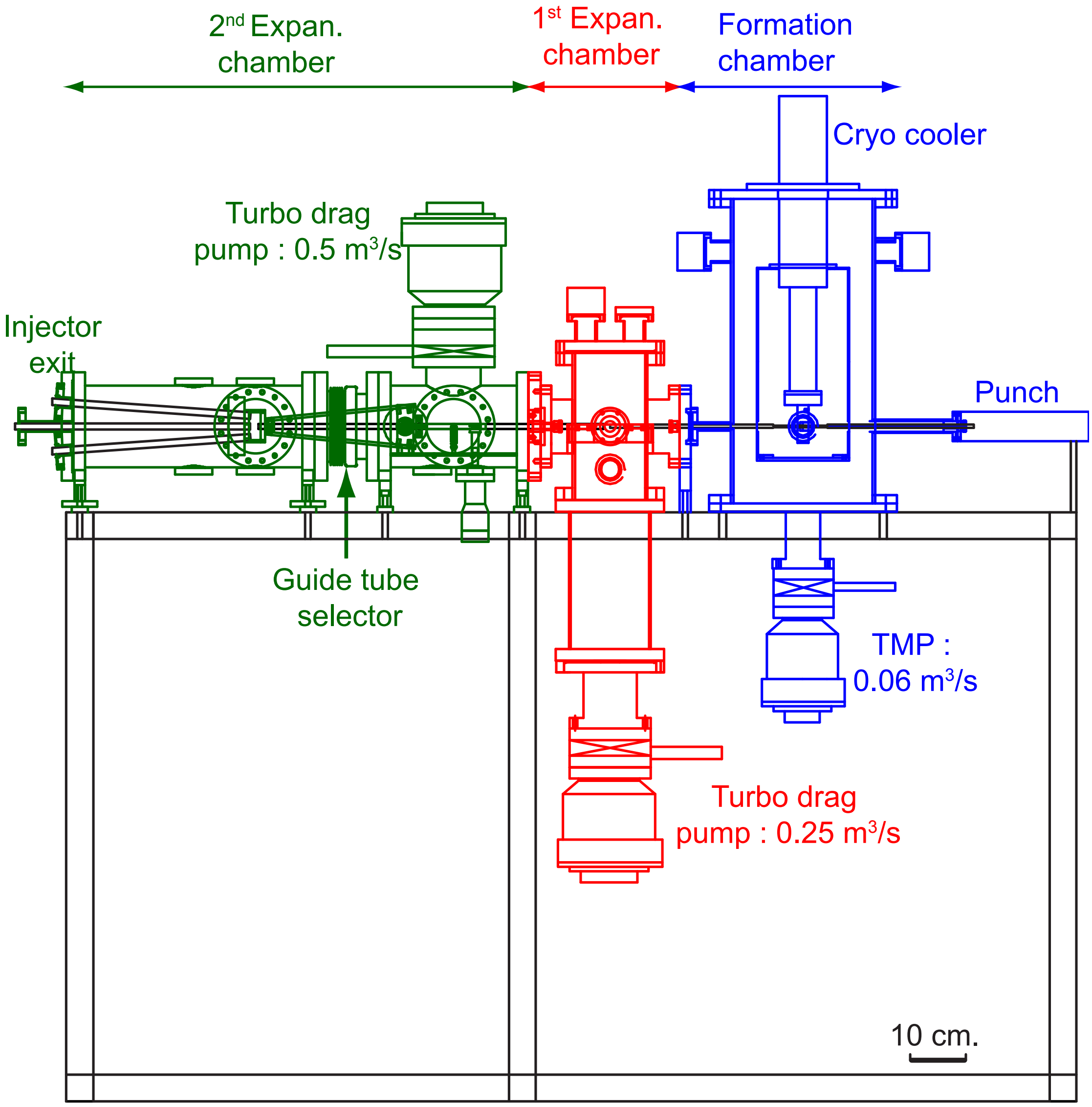

Figure 3.1 Schematic view of the punch-mechanism based low speed pellet injector

only on the H_2 pellets. To form the pellet, proper temperature and pressure are required below its triple point. The phase diagram of Hydrogen is plotted in Fig. 3.2. The triple point of the

Table 3.1 Properties of H_2 isotopes

Isotope	**Triple-point temperature (K)**	**Triple-point pressure (bar)**	**Density (gm/cm^3)**	**Yield strength (bar)**
H_2	13.9	0.072	0.087	0.7-3.5 (at 12.0 to 4.2 K)
D_2	18.7	0.172	0.200	0.7-3.5 (at 16.4 to 4.2 K)
T_2	20.6	0.216	0.320	0.7-3.5 (at 9.0 K)

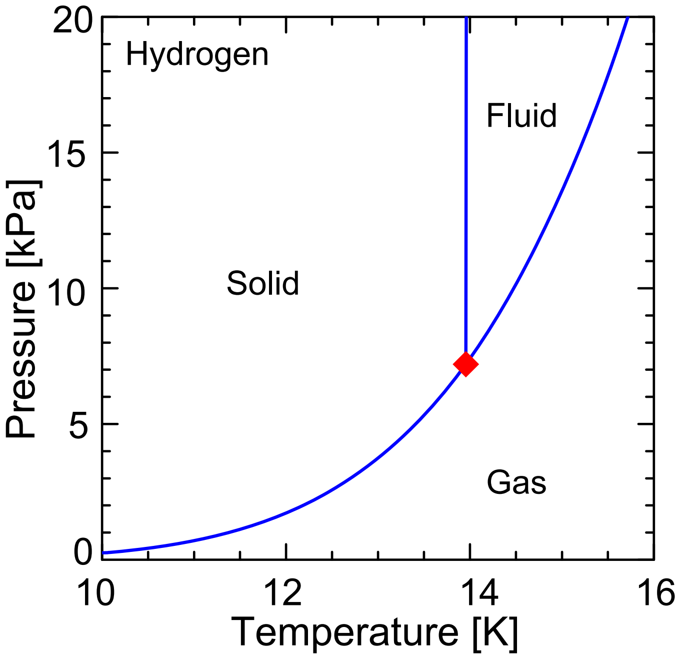

Figure 3.2 Phase diagram of H_2 isotope showing solid, liquid and gas phases. Triple point at a temperature of 13.9 K is indicated by the solid diamond symbol.

Hydrogen at 13.9 K temperature and at 0.072 bar pressure is indicated by the diamond symbol. As the triple point temperature for H_2 is 13.9 K, commonly, a pellet is formed at a temperature within 5-12 K cold head temperature at proper gas pressure. The density of the pellet is 0.087 gm/cm^3 in case of H_2 pellet.

3.3.2 Cryogenic Chamber

The heart of the pellet injector is the pellet formation region. As the pellet forms at very low temperature, it needs either liquid Helium cooled system or closed cycle cryocooler. The pellets are formed at very low temperature; therefore low heat loss and high strength materials should be chosen for the pellet formation region. In this design a Gifford-McMahon cycle compact cryocooler (SHIRDK-415) is being used. The GM-cycle cryo-cooler has the advantage that it is free from replenishment of cooling media such as liquid helium and can be easily and remotely operated by using the common utilities such as cooling water and electricity inside experimental hall. The cooling capacity of this cryocooler is 10 W at 8 K on the second stage. The cryo head heat sink has two stages of temperature 40 K and 4 K, respectively. A 'T'shaped OFHC Cu block is attached to the second stage of the heat sink at 4 K temperature to hold the pellet formation barrel. To make a better contact of the Cu block with the sink head a thin indium foil is inserted between them. The barrel made up of stainless steel of internal diameter 3 mm is connected to the Cu block via a Cu disk brazed onto it. The width of the brazing is 3 mm, so that a cylindrical pellet (3 mm$\ell\times$ 3 mmφ) is formed at the freezing area. The barrel is extended from the pellet acceleration system at the breach side to the subsequent stages at the front side. A Cernox thin film resistance temperature sensor (CX-AA type) from Lake Shore Cryotronics is used to accurately measure the temperature of the pellet formation region. The temperature sensor used is factory calibrated, can make measurements in the range of 0.1 K to 325 K. The measurement accuracy is ±25 mK at cryogenic temperature. Two voltage controlled polyimide thermo-foil flexible heaters are installed on the both side of the Cu block to maintain the temperature of the pellet formation region at the required level. To reduce the heat loss from the system, the pellet formation region is properly enclosed by cylindrical thermal shield, made up of Cu. The shield is connected to the first stage of the cryocooler at 40 K temperature. This cylinder is open just at points where the pellet formation barrel passes through it, so that effective head load to this system is minimized. As the cryo head is connected to single barrel, it efficiently cools the pellet formation region. When more barrels are connected to the heat sink, a proper thermal analysis considering conduction, convection and radiation should be necessary to know the characteristics of the cooling region, otherwise it can affect the quality of pellet formation.

All these cryogenic parts are enclosed within a vacuum chamber as shown in Fig.3.1 (Formation chamber). The vacuum chamber is maintained at a vacuum level of 10^{-5} Pa by employing a turbo-molecular pump of pumping capacity 0.06 m^3s^{-1}. The chamber is also equipped with necessary vacuum gauges and valves for efficient operation. The electrical connection cables inside the vacuum vessel to the temperature sensor and the heater are connected via vacuum feed through, compatible with high vacuum conditions. While connecting the cables to cold region at second stage, it is worthy to wrap it on the 40 K thermal shield so that heat loss due to conduction through these wires is minimized. Due to less heat load to the cryo-cooler, it takes $\approx$ 80 minutes to cool down the barrel from room temperature to 5K and hence, the injector is ready for operation within 90 minutes of switching on. The cooling system should be efficient to be able to form a pellet within the plasma shot timing interval. In LHD, the plasma shots are taken at every 3 s time interval. The injector handles only one pellet and the heat load to the system is very less, therefore the increase in temperature ($\approx$ 0.5 - 0.8 K) during the pellet injection recovers quickly, and the injector gets ready for another pellet formation cycle.

3.3.3 Vacuum and gas feed system

High pressure propellant gas is needed to accelerate the pellet into higher speed. The propellant gas added in this process should be removed from the injection line in-order to restrict it from entering the plasma chamber. A two stage differential pumping system has been installed to remove the propellant gas from the injection line. The volumes of the 1^{st} and 2^{nd} expansion chambers are of 0.015 and 0.02 m^3 respectively. Both the expansion chambers are connected to the turbo-drag pumps of pumping speed 0.25 m^3s^{-1} and 0.5 m^3s^{-1}, respectively. Expansion chamber-1 and expansion chamber-2 are maintained at a vacuum level of 10^{-5} and 10^{-6} Pa, respectively. The injection path extending from the formation chamber and passing through the expansion chambers have two breaks of length 2 cm each for the removal of the propellant gas. The guide tube connecting both the expansion chamber is of length 66 cm. A schematic diagram of the vacuum system with the fueling and propellant gas lines is shown in Fig. 3.3. The filled and unfilled arrows in the

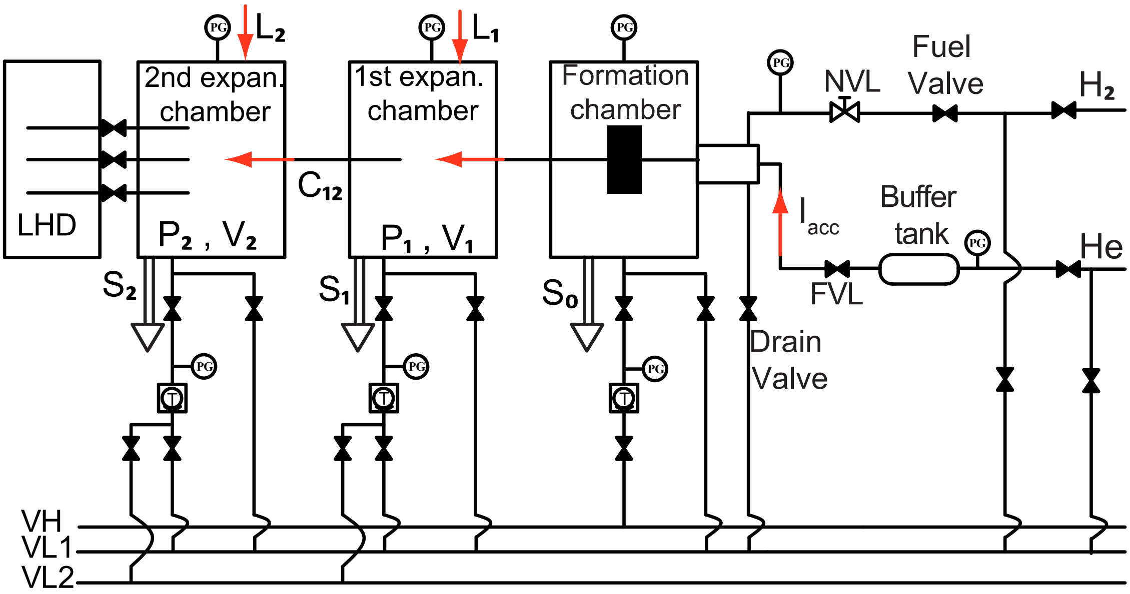

Figure 3.3 Vacuum system of pellet injector showing pellet formation region, two stage differential pumping system and gas (fueling and propellant) feed system.

diagram indicate the inflow (L_1, L_2 and I_{acc}) and out flow (S_1, S_2 and S_3) to the vacuum system, respectively. The inflow of the propellant gas to the formation chamber is restricted, by isolating it from the differential pumping stage. The lines VL1 and VL2 are used for the removal of propellant gas from the differential pumping stage during the injector operation.

Considering a maximum of 2.5 Pam^3 of propellant gas required for single pellet injection, vacuum characteristics for differential pumping system can be calculated from the following equation.

$$\begin{cases} V_1 \frac{dP_1}{dt} = I_{acc} + C_{12}(P_2 - P_1) - S_1 P_1 + L_1 \\ V_2 \frac{dP_2}{dt} = C_{12}(P_1 - P_2) - S_2 P_2 + L_2 \end{cases} \tag{3.1}$$

Where I_{acc}, P_{i}, V_{i}, S_{i}, $C_{\mathrm{i,i+1}}$ and L_{i} denotes the propellant gas inflow rate, pressure of stage i, volume of the stage i, pumping capacity of the stage i, conductance between the stages i and i + 1 which are connected by the guide tube and leak and/or degassing rate of stage i, respectively. The characteristics curve of this vacuum system calculated by using the above equation is plotted in Fig. 3.4. Actual pressure rise during the pellet injection is also shown by the dots with solid symbol. The vacuum characteristics for the differential pumping system infers that the vacuum level of the first stage and final stage deteriorates to 10^2 Pa and 2.5×10^{-2} Pa, respectively. It can be observed from the figure that experimentally observed vacuum levels in both stages are of little

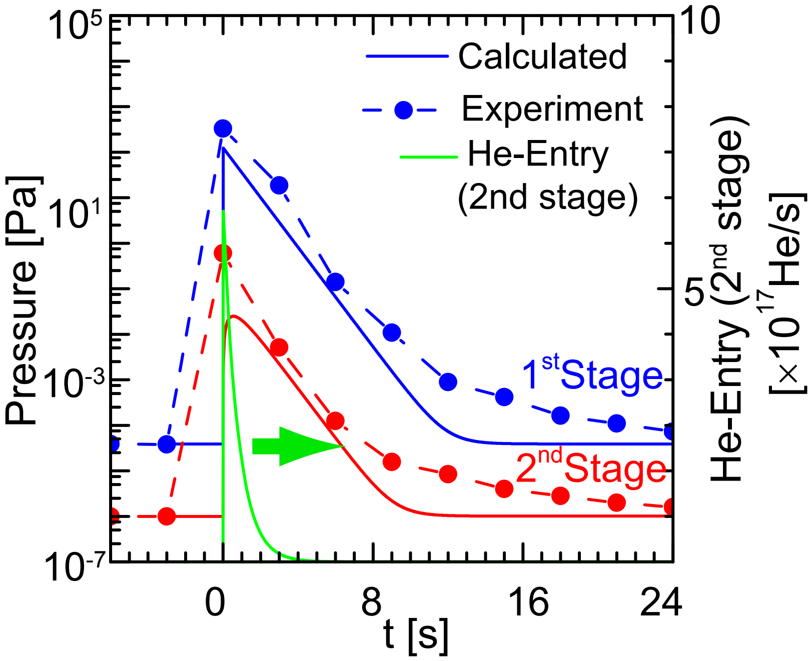

Figure 3.4 Vacuum characteristics curve for two-stage differential pumping system.

higher than the calculated value. This increase is due to the direct inflow of the accumulated gas inside the punch mechanism device through the barrel (which has bad conductance), and evaporation of H_2 gas inside the barrel. The effective inflow of the propellant gas (He) into the final stage is of the order 5×10^{17} atoms per second at a maximum and is reduced with the decay time constant of 2 s. Because the effective inflow is considerably small compared to the pellet mass (10^{21} atoms/s), negative effects of the residual propellant gas is negligibly small. During the pellet injection into the plasma, the increase in the pressure of these chambers by the inflow of propellant gas is recovered within few seconds (typically less than 15 s) after the pellet injection. Therefore it is possible to inject a pellet synchronizing with the LHD discharge timing (180 s).

Pellet guiding tubes of internal diameter 9.25 mm connected to various injection locations are pumped through the second expansion chamber. The length of the guide tube for the outboard side injection port is 2.2 m with two bends. The inner port guide tube is 21 m long with five bending. All the curved guide tubes have a curvature radius of 0.8 m except one of the guide tubes at the inboard location has curvature radius of 0.3 m. A schematic of the pellet injector with guide tubes used for the different pellet injection locations is shown in Fig. 3.5. The second expansion chamber is equipped with a guide tube selector and it can direct the pellet to three different locations. The guide tube selector is controlled remotely to select an injection location.

The solenoid punch used for the pellet breakaway from the freezing zone is connected to the breach side of the barrel. The gas feed system for the injector controls the low-pressure H_2 fuel gas and the high-pressure He propellant gas (Fig. 3.3). The fueling and the propellant gas feed systems are connected to the barrel through the punching device. The needle valve connected to the fueling gas line controls the pellet formation pressure. A 25 cc buffer cylinder just before the fast opening valve is used in the propellant flow line to accelerate the pellet efficiently.

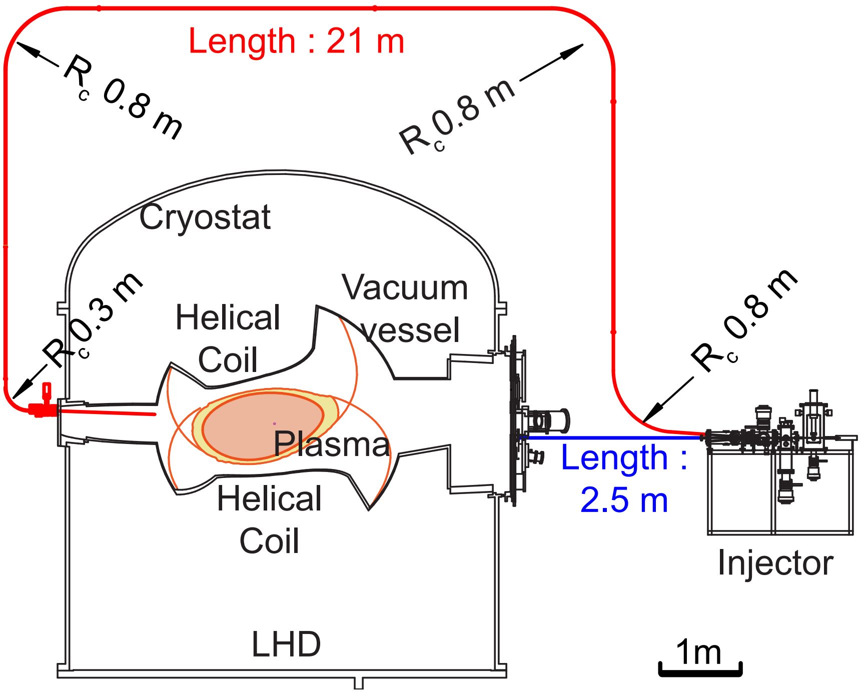

Figure 3.5 Schematic view of LHD with guide tubes connecting between the pellet injector and various injection ports.

3.3.4 Diagnostics

After the pellet is being injected, two basic injection parameters are of interest is the speed and mass of the pellet. For this purpose, the injector is equipped with two light gates to measure the pellet speed by using the time of flight measurement between two fixed positions. Each light gate consists of a laser and a high-speed photodiode. The shadow-graphic system consisting of a CCD camera and a flash lamp of 180 ns pulse width is installed on second expansion chamber to confirm the intactness of the pellet. Also, similar sets of light gate and shadowgraph systems are installed on the inboard side guide tube exit to measure the pellet speed and to check the intactness of the pellet after its passage through the curved guide tube. The inboard side measurements were only considered during the bench test, as it is difficult to operate these devices in presence of high $\boldsymbol{B}$ at the inboard side during the plasma discharges. A schematic view of the pellet speed measurement from the two light gate signals is shown in Fig. 3.6. In this figure Lg-1 and Lg-2 corresponds to the photodiode signals installed at the expansion chamber-1 and 2, respectively. A dip in both the signals corresponds to the time at which the pellet crosses the laser light. By knowing the difference in both the light gate timings (Δt) and the separation length between them (ΔL), the pellet speed can easily be calculated. The light gate signal Lg-2 is also used as the trigger for shadow-graphic camera system to take a picture of the passing pellet. The shape of the pellet calculated from the shadow-graphic image is used for the estimation of the pellet mass, which in turn is useful for the pellet mass deposition analysis inside the plasma.

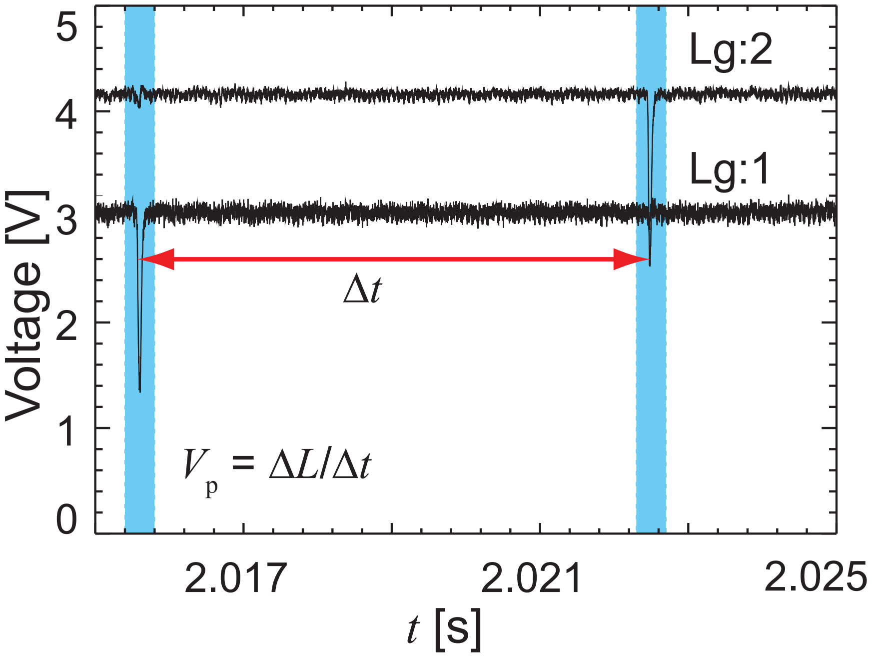

Figure 3.6 Photo diode signal for both light gates used for the calculation of pellet speed

3.3.5 Control and Data acquisition

Due to inaccessibility of the experimental hall during plasma operation, the pellet injector should be operated remotely. A PC based control system is developed on a Microsoft Windows platform by using LABVIEW 8.6 software with National Instruments Compact Field Point (CFP) controller and input-output card. The CFP placed near the injector in the experimental hall can easily be accessed from the LHD control room via an Ethernet network. A block diagram of the injector control and data acquisition system is shown in Fig. 3.7. The cryo-cooler and all the vacuum valves and pumps are controlled remotely using this software. The CFP analog modules acquire the pressure and temperature data of the injector. The acquired analog data and the status of the various devices are stored automatically at 3 s intervals. All the instruments in the injector can be controlled remotely by the graphical user interface in the remote computer. The picture of the user

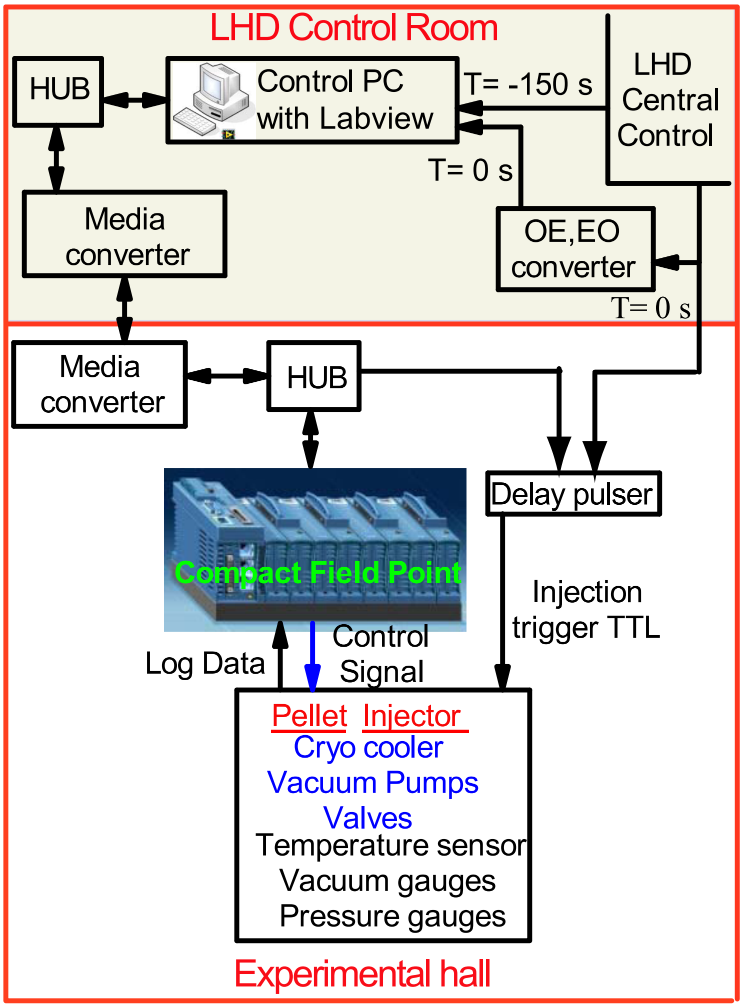

Figure 3.7 Block diagrams of the injector control and data acquisition system

interface control is shown in Fig. 3.8. In LHD, the duration between two discharges is 3 minutes.

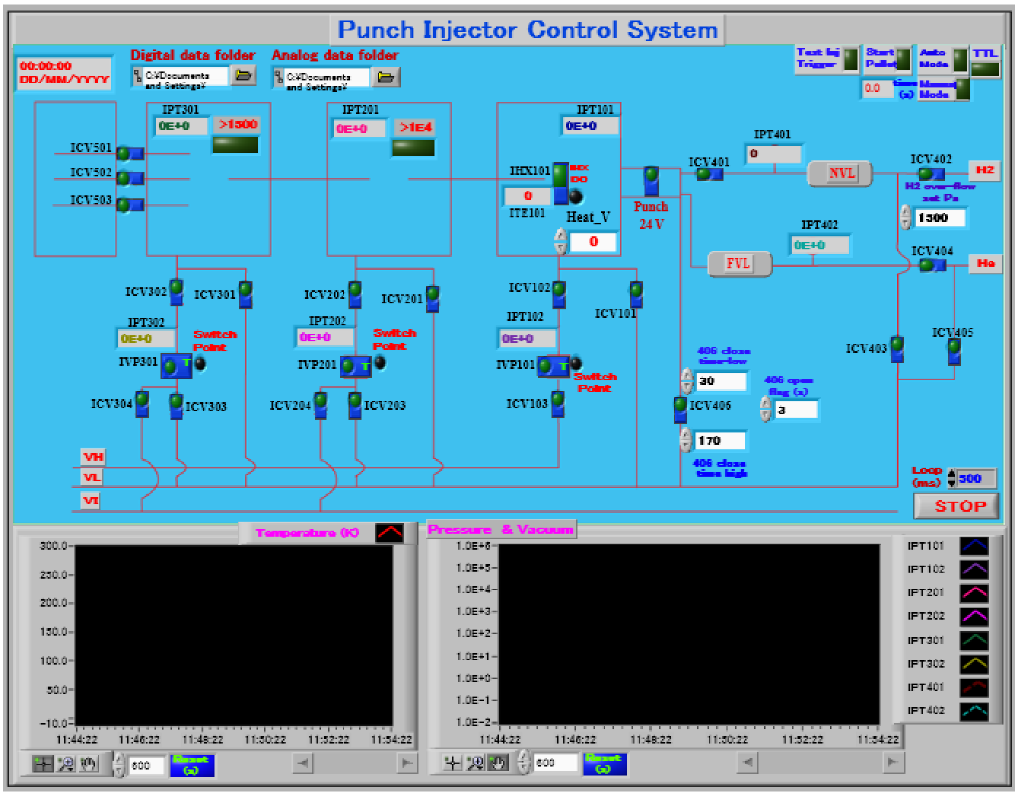

Figure 3.8 LABVIEW based user interface control for the injector remote operation.

The pellet formation cycle is also synchronized with the LHD central control by this software, so that a pellet is being injected at a regular interval of 3 minutes during the plasma discharges. The timing signal for the solenoid punch and the fast valves are controlled by another PLC with a delay pulser. Diagnostic systems such as the light gates, fast camera and fast photodiode data's are acquired by high-speed ADCs.

3.4 Injector Operation and Characterization

After the installation of the pellet injector in the LHD, all the necessary experiments are carried out to check the credibility of the pellet injector. As the major objective of this injector is low speed pellet injection through the curved guide tubes, tests concerning the pellet formation process, speed inside the guide tube and the intact tests at different formation temperatures are done and the results are presented in the following sections. The following section is organized as follows. At first, the pellet formation and injection process is described. After that the pellet speed is modeled using the Ideal gun theory (IGT) approximations. Finally the results from the injector characterization are presented.

3.4.1 Pellet formation and launching

A pellet (3 mm$\ell\times$ 3 mmϕ) contains 10^{21} Hydrogen atoms, hence for a plasma of volume 30 m^3, increase in density of 3×10^{19} is expected. The schematic view of the pellet formation barrel with the injection mechanism is shown in Fig. 3.9. The pellet formation cycle starts with a trigger from

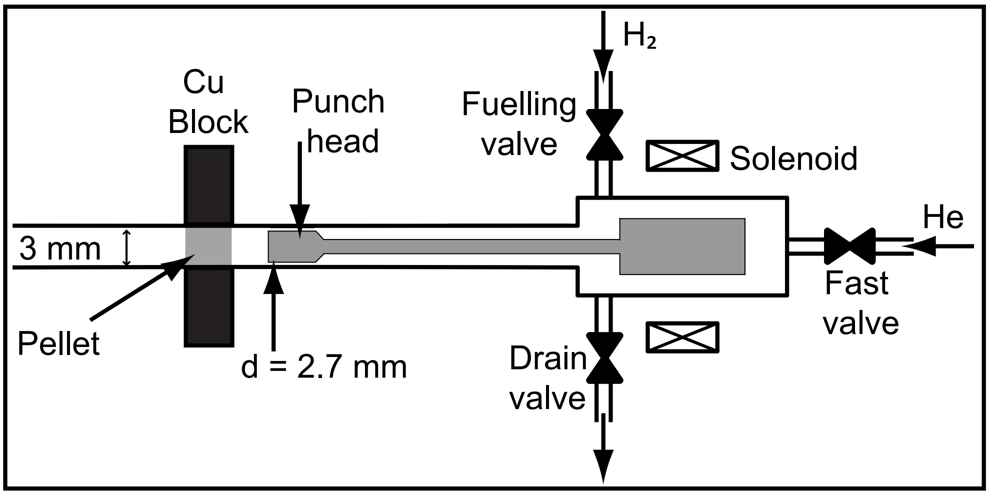

Figure 3.9 Low speed pellet injection mechanism using mechanical punch and pneumatic propellant system.

the control system at 160 s prior to the plasma discharge. At first the fueling valve is opened to allow the gas flow through the barrel towards first expansion chamber. As the gas passes through the cold region below the heat sink, a pellet of desired size is formed. It takes around 50 - 60 s to freeze one pellet at a pellet formation temperature (T_{p}) of 8 K. The freezing time also depends on the cryo head temperature and the fueling gas pressure. As soon as a pellet forms, it blocks the gas flow to the other side and the pressure in the fueling line increases. This increase in pressure is used as an indication for the pellet formation inside the barrel. Consequently the fueling valve (Fig. 3.9) is automatically closed at a preset pressure level. The remaining fuel gas inside the barrel then drained out through the drain valve. Few ms before the injection, the drain valve is closed, and the injector is ready for injection. Pellet breakaway from the freezing zone starts with the activation of the punch head. A few ms (3 - 7) later the fast valve is opened, and the He propellant flows into the barrel and accelerates the pellet to higher speed. By varying the propellant gas pressure, the speed of the pellet is controlled. The pellet is directed to the different injection locations by using the remotely operated guide tube selector, installed in the second expansion chamber.

3.4.2 Pellet speed and Ideal gun theory

The pellet speed inside the barrel can be modeled with the help of the Ideal gun theory (IGT) approximations. In the framework of the IGT, the flow inside a cylindrical pipe is assumed to be one-dimensional and the change in flow variables is small and gradual. The projectile (pellet) inside the tube moves due to the expansion of the gas in the volume confining it. The name Ideal is based on the assumption that the non-ideal effects such as friction at the projectile tube interface, heat transfer through the tube wall, viscosity and the leakage of the gas are neglected. Considering the flow as adiabatic and one-dimensional (V_{y} and $V_{\mathrm{z}} = 0$), the pressure inside the tube can be written as, [66]

$$P(t) = P_0[1 - \frac{1}{2}(\gamma - 1)|U|/C_0]^{2\gamma/(\gamma-1)}, \tag{3.2}$$

where, $P(t)$ is the pressure at a particular section as a function of time, P_0 is the initial pressure at time $t = 0$, U is the velocity of the gas, C_0 is the sound speed of the gas at $U = 0$, and γ is the ratio of heat constants. Using the above equation, the equation of motion of the pellet by the sudden application of gas inside the gun barrel can be written as,

$$\frac{m_\mathrm{p}}{A_\mathrm{p}}\frac{dV_\mathrm{p}(t)}{dt} = P_0[1 - \frac{1}{2}(\gamma - 1)V_\mathrm{p}(t)/C_0]^{2\gamma/(\gamma-1)}. \tag{3.3}$$

Integrating the equation of motion, the speed of the pellet $V_\mathrm{p}(t)$ after a time t is,

$$V_\mathrm{p}(t) = \frac{2C_0}{\gamma - 1}\left[1 - [1 + \frac{(\gamma+1)P_0A_\mathrm{p}}{2m_\mathrm{p}C_0}t]^{-\frac{(\gamma-1)}{(\gamma+1)}}\right], \tag{3.4}$$

where, A_p and m_p denotes the base area and the mass of pellet, respectively. The maximum attainable speed (V_p^{max}) by the pellet can be calculated from the equation (3.4) by setting the applied gas pressure to zero expansion as,

$$V_\mathrm{p}^{max} = 2C_0/(\gamma - 1). \tag{3.5}$$

For ideal gas conditions, $C_0 = \sqrt{\gamma RT/m}$, where R is the universal gas constant, T is the temperature, and m is the molecular weight of the propellant gas. Therefore, the light gases act as good propellant. With increase in temperature, if C_0 exceeds the speed of the sound at that temperature, the pressure to the pellet surface decreases and there is no increase in the pellet speed. Using He as the propellant gas, theoretically, the maximum speed can be attainable is 3000 ms^{-1}. However, due to the non-ideality in the system, the attainable speed is lower in practice. Therefore, the optimization of the barrel length is needed for a given projectile and propellant conditions. Using the Eqn. 3.4, the net acceleration path length L, in-terms of the muzzle velocity V_m (speed at the exit of the barrel) can be written as,

$$\begin{aligned} L(V_\mathrm{m}) &= \int V_\mathrm{m}(t)dt \\ &= \frac{2C_0}{\gamma - 1}\left[t - \frac{MC_0}{A_\mathrm{p}P_0}(1 + \frac{(\gamma+1)A_\mathrm{p}P_0}{2MC_0}t)^{\frac{2}{(\gamma+1)}}\right] + \frac{2MC_0^2}{(\gamma - 1)A_\mathrm{p}P_0}. \end{aligned} \tag{3.6}$$

Defining the characteristic time $\tau = [(\gamma - 1)\mathrm{V}_\mathrm{p}^{max}M]/[(\gamma + 1)A_\mathrm{p}P_0]$ and a constant $L_c = \frac{2MC_0^2}{(\gamma-1)A_\mathrm{p}P_0}$ of dimension in length, the above equation can be written as,

$$L(V_\mathrm{m}) = tV_\mathrm{max} - L_\mathrm{c}(1 + \frac{t}{\tau})^{\frac{2}{(\gamma+1)}} + L_\mathrm{c}. \tag{3.7}$$

It can be inferred from the Eqn. 3.3 that, that, higher pellet speed can achieved at a relatively small gas pressure. Using the Eqn. 3.7, the barrel length can be optimized for the desired range of pellet speed.

3.4.3 Characterization of the pellet injector

At the first step to characterize the pellet injector, the response of the pellet speed to the propellant pressure is checked. The speed of the pellet is calculated from the light gate barriers as discussed in Sec. 3.3.4. Figure 3.10 shows the variation of the pellet speed as a function of the propellant gas pressure. It can be observed from the figure that there is a large deviation of the experimentally observed pellet speed (solid circles) from the Ideal gun theory approximation (solid line) [57]. This observed variation may be due to the over estimation of the barrel length ($L = 0.35$ m) for the pellet

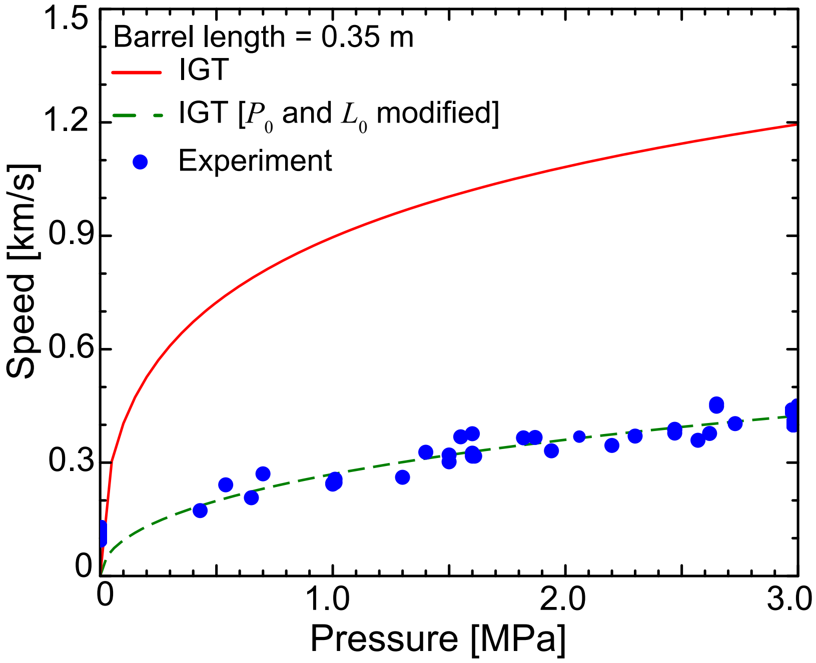

Figure 3.10 IGT approximation of pellet speed at different propellant pressure (Solid line). The dashed curve indicates the IGT speed after pressure, P_0, and barrel length, L_0, correction. Solid circles indicating the experimentally observed pellet speed.

acceleration in the IGT calculation. Since there is a finite delay in the fast valve operation after punch activation, the effective barrel length for the IGT approximation is modified by considering the punch speed and delay time. Also there is a certain flow of the propellant gas into the punching head volume, as the propellant gas line is connected to the barrel through the punch head. Therefore the effective pressure (P_0) for the pellet acceleration is also reduced. Hence, a pressure drop factor and an effective barrel length term are introduced in the IGT calculation. The modified pellet speed by considering the above aspects matches (dashed line) well with the experimental data.

To measure the pellet speed and intactness, a set of light gate and a shadowgraph system are installed at the vessel inboard guide tube exit. An intact pellet size of $\approx$ 2.7 mm has been confirmed from the shadow-graphic image. Figure 3.11(a) shows an intact pellet for V_p = 348 ms^{-1} and Fig. 3.11(b) shows a broken pellet for V_p = 380 ms^{-1} at T_p = 6.5 K. Although there is no direct measurement of pellet mass loss inside the curved guide tube, the shadow-graphic image suggests $\approx$ 10 % mass loss, which agrees well with the measurements in Ref. [64]. Concerning with the pellet mass, μ-wave cavity method is an efficient and more exact method for pellet mass determination. Using the two μ-wave cavity detectors, pellet mass loss calculation with good accuracy has been reported by Combs [67]. In that report it has been also reported that, it is possible to identify the intact / broken pellet simultaneously, using this method.

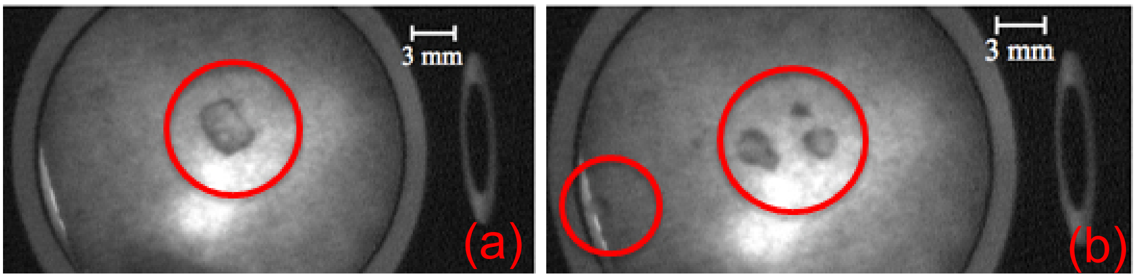

Figure 3.11 Shadow-graphic image of (a) an intact pellet at 348 ms^{-1} and (b) a broken pellet at 380 ms^{-1} taken at inboard side guide tube exit. The circles on both figure indicate the position of pellet / pellet fragments on the image.

Effect of the pellet formation temperature on its characteristics has been studied. The variation of the pellet speed with the propellant gas pressure at different T_p is shown in Fig. 3.12. The pellet speed variation with pressure is similar for all temperatures. In the figure, a filled symbol corresponds to the minimum speed at which a broken pellet has been observed at a particular pellet formation temperature. Pellets having speed below that of the symbol are intact and above it are both intact and broken. The pellet speed variation of 85 - 115 ms^{-1} has been observed using the solenoid punch only. Therefore 100 ms^{-1} in the figure refers to the speed of the pellet using the solenoid punch only. A comparison of pellet muzzle speed (filled symbols) with the speed at the guide tube exit is shown in Fig. 3.13. The solid line indicates the case when there is no speed loss inside the guide tube. The figure indicates that the pellets slowed down inside the curved guide tube and the measured speed loss (open symbols) is less than 6 %. No significant dependence of pellet speed loss on the pellet formation temperatures has been observed.

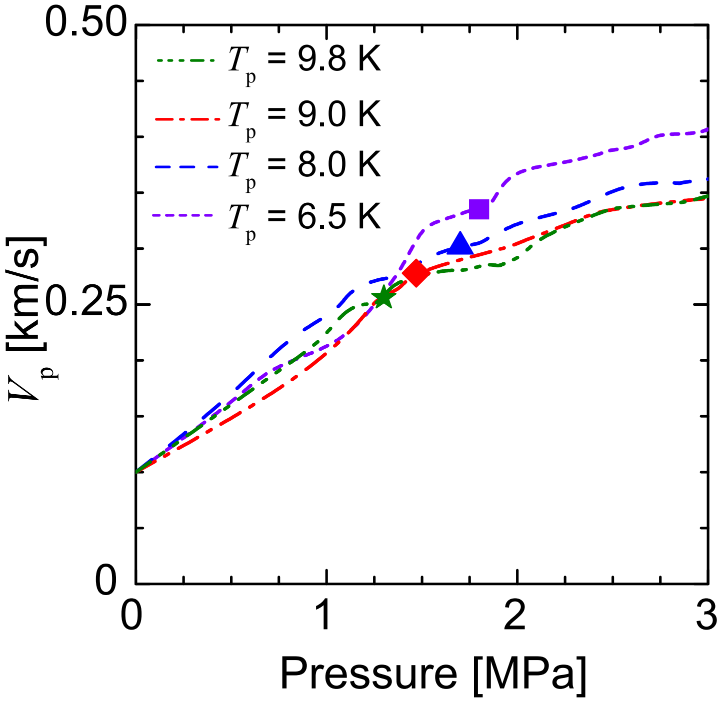

Figure 3.12 Change of pellet speed with propellant pressure at different T_p.

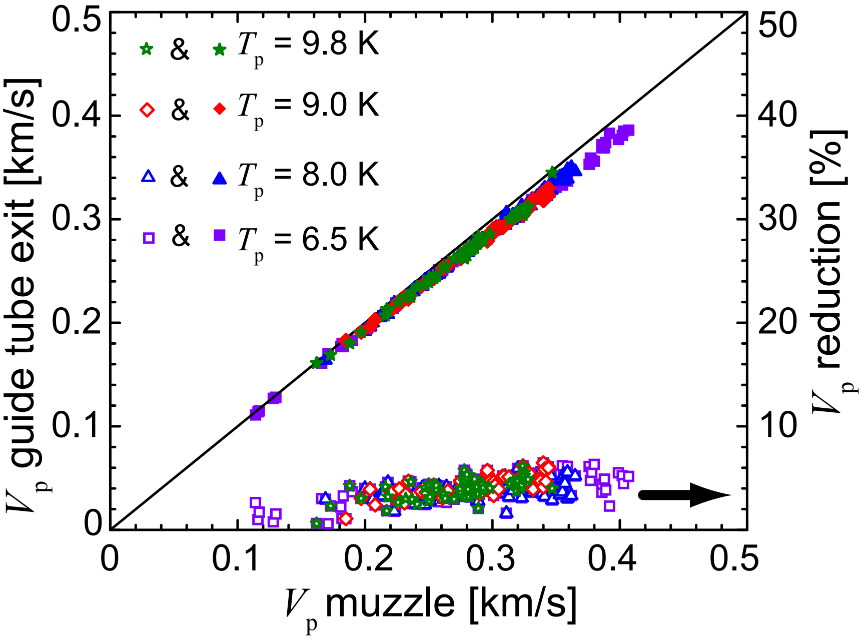

Figure 3.13 Comparison of V_p at curved guide tube exit with pellet muzzle speed (filled symbols) at different T_p. Pellet speed reduction (%) with muzzle speed (open symbol)

The dependence of the intact pellet speed limit on the pellet formation temperature has been studied for four different temperatures. The fraction of the pellets that were found to be intact (intact pellet fraction) is calculated by taking a ratio between the number of intact pellets at the guide tube exit and total number of the injected pellets. The variation of the intact pellet fraction with the injection speed is plotted in Fig. 3.14. More than 75 test shots were considered in the calculation for each pellet formation temperature. A horizontal bar on the line corresponds to a bin size of 30 ms^{-1} over which the intact pellet fraction is calculated. The number of shots used in the intact pellet fraction calculation for each bin size is shown over the horizontal bar. It can be observed from the figure that the intact pellet fraction at a particular temperature decreases with increase in injection speed. As the data points correspond to the center of the bin size in the calculation, falling of the curves from the intact line (intact pellet fraction =1) before a broken pellet has been observed is obvious. The minimum speed at which a broken pellet has been observed

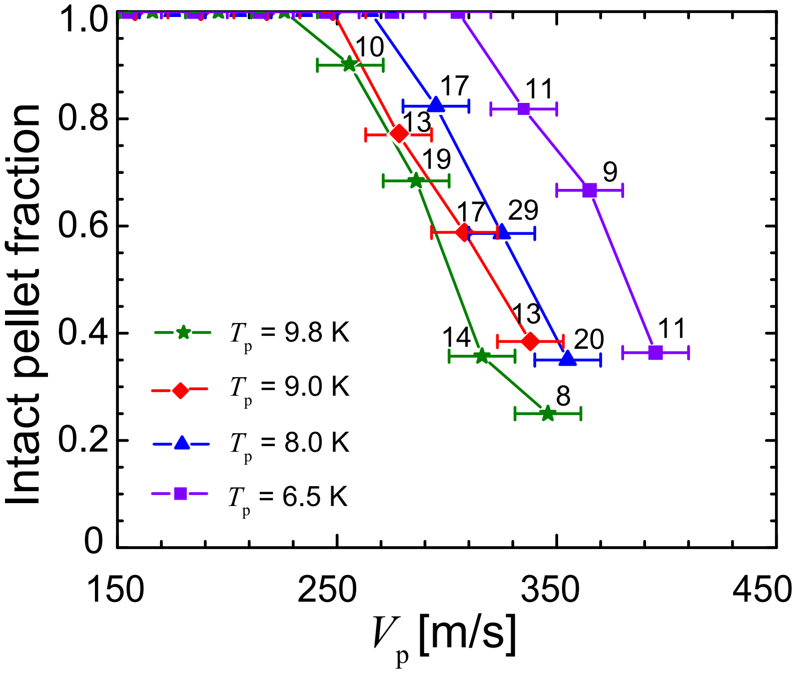

Figure 3.14 Intact pellet fraction plotted against injection speed at different T_p. The horizontal bars indicate the bin size of the speed taken to estimate the intact pellet fraction.

varies from 335 ms^{-1} at T_p = 6.5 K to 256 ms^{-1} at T_p = 9.8 K. A study with similar pellet size (2.7 mm) and guide tube configuration has been reported earlier [64]. The lower speed limit for an intact pellet at the temperature range 8 to 9 K discussed here is in good agreement with the previously reported observation, where it is 270 ms^{-1}. The higher speed limit over which all the broken pellets can be observed has not been found because of inability to achieve the higher speed for the existing barrel length. Since the pellet conditions are similar in the temperature region 8-9 K, it is most likely that the upper speed limit for intact pellets would be similar to the previously reported observation, where the highest speed that a pellet can survive was found to be 470 ms^{-1}. Considering pellet erosion by the centrifugal force due to the curvature of the guiding tube, above observations can be explained by performing a simple physical model calculation. The relation between the pellet tensile strength σ_t and the centrifugal force can be written as [68],

$$\sigma_t = \frac{m_p {V_p}^2}{A R_c} \tag{3.8}$$

Where m_p is the mass of the pellet, V_p is the velocity of the pellet, A is the area of the pellet in contact with guide tube wall, and R_c is the curvature radius of the guide tube. Considering A = 10 % of total surface area, the relation between V_p and R_c can be written as $V_p = 400\sqrt{R_c \sigma_t}$ ms^{-1}, where σ_t varies in the range of 0.7 - 3.5 bar at T_p = 12.0 - 4.2 K [62] for H_2 pellet. The guide tube used for pellet transfer to the launching locations has several bends of bending radius 0.8 m and one bend of curvature radius 0.3 m. Therefore considering the minimum curvature radius in the calculation, the speed at which a pellet can be delivered intact has been calculated at different T_p. A comparison between observed (solid circle) and calculated (solid line) intact pellet speeds at different pellet formation temperatures are shown in Fig. 3.15. From the figure it can be

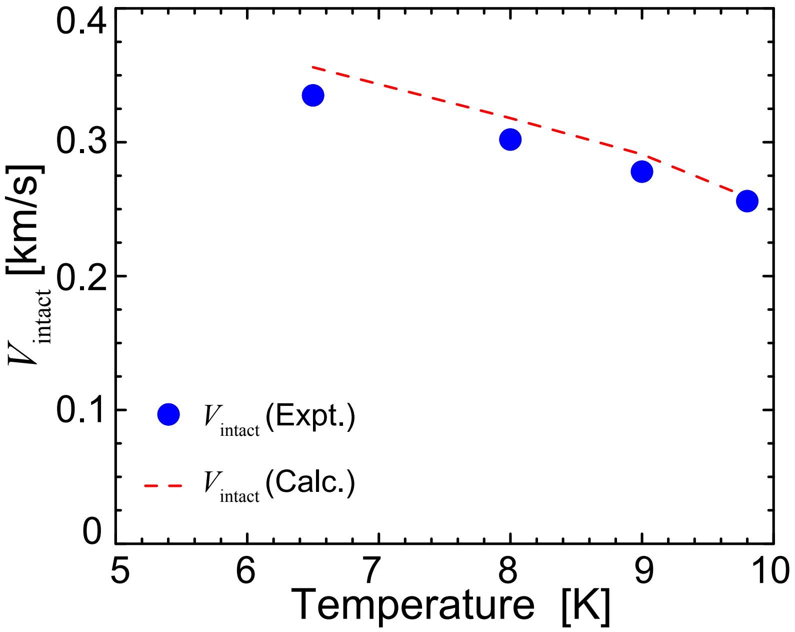

Figure 3.15 Comparison of experimentally obtained intact speed (Solid circle) with calculated intact speed (Broken line) at different T_p

inferred that the experimental points follows the calculation. In addition to this, another possible mechanism may contribute to pellet fracture is from multiple collisions inside the guide tube as the pellet possibly bounces in it. Although the model described here is a simplistic one but it appears to be reasonably good to predict the pellet fracture inside the curved guide tube. While optimizing the pellet transfer tubes for the HFS injection in ASDEX-U, it has been reported that impact angle of the pellet with the guide tube is an important factor for the survivability of an intact pellet inside it [69]. The impact angle needs to be such that the impact stress should not exceed the plastic flow regime. This fact leads to the conclusion that, the corresponding perpendicular pellet speed should be less than 40 ms^{-1} during pellet impact with the guide tube wall.

3.5 Summary

A low speed single barrel pellet injector using a mechanical punch device at the breach side of the barrel has been designed for alternative injection in LHD. Considering the three dimensional nature of the LHD magnetic field, alternative (HFS) injection locations around the torus are chosen to carry out pellet injection and fueling studies. A number of curved guide tubes of curvature radius R_c = 0.8 m and 0.3 m are being used for the pellet transfer to the respective pellet injection locations. Pellet transfer characteristics through the guide tube are tested at different pellet formation temperatures. Pellet speed loss within the guide tube is found to be less than 6 %. The intactness of the pellet is verified by comparing the shadow-graphic image and light gate signals at the injector and the curved guide tube exit. The observed variation of the minimum speed at which a broken pellet has been observed at different pellet formation temperatures, is comparable to the calculated intact speed by considering the pellet yield strength at that temperature. However the maximum intact pellet speed limit (after which all the pellets are broken) has not been demonstrated due to the inability of the injector to achieve higher pellet speed. The possible cause may be the shorter barrel length. With this, the injector is able to inject a pellet (< 275 ms^{-1}) through the curved guide tube to the alternative injection locations in LHD.

Chapter 4

Stereoscopic Diagnostics

4.1 Introduction

It is well established that, the pellet injection is a favorable method for core plasma fueling [70]. In order to get a deeper knowledge into the physics of pellet dynamics inside the plasma, such as pellet ablation [71], cloud dynamics [72], trajectory of the injected pellet [73], efficient diagnostic systems are necessary. The pellet ablation process inside the plasma lasts for few milli seconds. Therefore diagnostics of high spatiotemporal resolution is necessary to understand the pellet ablation dynamics in sub milli second time scale. In several fusion machines, high frame rate fast imaging camera with optical imaging fiber is used to study the pellet ablation process inside the plasma. In the past, using gated - intensified charge coupled device (CCD) camera, measurement of the pellet cloud characteristics was also reported [74]. Apart from the information regarding the cloud characteristics, measurement of the pellet trajectory and speed are also very important. In this regard, pellet trajectory measurement using position sensitive detectors or photo multiplier tube arrays has been reported by many authors [75–77]. In order to measure these quantities simultaneously, three-dimensional diagnostic system basing on the fast framing camera from two different observation points has been reported from ASDEX-U tokamak [78].

In LHD, as the magnetic confinement field is generated by the external helical coils, the plasma cross section varies three dimensionally between a horizontal and vertical elongated section throughout the torus. Additionally, the fast ions generated by the NBI heating play a significant role in the pellet ablation process. Therefore in presence of such a three-dimensional plasma, a complicated pellet-plasma interaction can be predictable. In order to get the three-dimensional information about a system, tomography is an accurate and powerful method [79]. In the case of tomography, multiple views on the same poloidal plane are necessary. Since, perpendicular observation ports are limited by the helical coil, stereoscopic principle has been applied to obtain the three-dimensional information about an ablating pellet in LHD [80]. Stereoscopy is a technique to extract the three-dimensional information about a system from the discrepancy of two or multiple images taken from different locations.

4.2 Stereoscopic principle

A camera is a mapping between the 3D world coordinate (object) and a 2D image coordinate. This kind of projection is called the perspective projection. The three-dimensional point $\boldsymbol{M}_\mathrm{c}$ = [X_c, Y_c, $Z_\mathrm{c}]^T$ in camera frame is imaged to the two-dimensional image point $\boldsymbol{m}_0 = [u, v]^T$ under the pinhole camera model by the following relation [81].

$$\begin{bmatrix} u \\ v \\ s \end{bmatrix} = \begin{bmatrix} f & 0 & 0 & 0 \\ 0 & f & 0 & 0 \\ 0 & 0 & f & 0 \\ 0 & 0 & 0 & 1 \end{bmatrix} \begin{bmatrix} X \\ Y \\ Z \\ 1 \end{bmatrix} \tag{4.1}$$

or

$$s\widetilde{\boldsymbol{m}}_0 = \boldsymbol{P}_0\widetilde{\boldsymbol{M}}_\mathrm{c} \tag{4.2}$$

where, s, is an arbitrary scale factor. The symbols with the tilde represent the respective coordinates in homogenous form. A homogenous coordinate is obtained by adding another element of magnitude 1 in the existing coordinate system. An example of this, the two-dimensional point $\boldsymbol{m}_0$

in the homogenous form can be written as $\widetilde{\boldsymbol{m}}_0 = [u, v, 1]^{\mathrm{T}}$. Equivalently the homogeneous points are scaled as (su, sv, s), and we can get back the original coordinates by dividing s.

In general, points in space are expressed in a coordinate system (world coordinate) different from the camera coordinate system. These two coordinate frames are related via a rotation and a translation. If $\boldsymbol{M}_{\mathrm{w}} = [X, Y, Z]^{\mathrm{T}}$ represents world coordinate, the corresponding point in the camera coordinate $\boldsymbol{M}_{\mathrm{c}}$ can be written as,

$$\widetilde{\boldsymbol{M}}_{\mathrm{c}} = \boldsymbol{D}\widetilde{\boldsymbol{M}}_{\mathrm{w}}. \tag{4.3}$$

Where $\boldsymbol{D} = \begin{bmatrix} \boldsymbol{R} & \boldsymbol{t} \\ 0_3^T & 1 \end{bmatrix}$ is the transformation matrix. The matrix $\boldsymbol{R}$ (3 × 3) and $\boldsymbol{t}$ are the rotation and translation matrix respectively.

In ideal conditions the image axes are perpendicular but due to electronic acquisition system, pixels are not square. If the image axes are not perpendicular and θ is the angle between image coordinates, a scale factor k_u and k_v can be introduced to correct the image coordinates. The old image coordinate $\boldsymbol{m}_0$ can transform to the new coordinate $\boldsymbol{m}$ by the following relation.

$$\widetilde{\boldsymbol{m}} = \boldsymbol{H}_{\mathrm{r}}\widetilde{\boldsymbol{m}}_0 \tag{4.4}$$

The image rectification matrix $\boldsymbol{H}_{\mathrm{r}}$ is written as $\begin{bmatrix} k_u & -k_v cot\theta & u_0 \\ 0 & k_v/sin\theta & v_0 \\ 0 & 0 & 1 \end{bmatrix}$.

Here u_0 and v_0 are the coordinates of the principal point. Combining the equations $[4.2 - 4.4]$, the complete camera transformation equation between a world and an image coordinates can be written as ,

$$s\widetilde{\boldsymbol{m}} = \boldsymbol{H}_{\mathrm{r}}\boldsymbol{P}_0\boldsymbol{D}\widetilde{\boldsymbol{M}}_{\mathrm{w}} = \boldsymbol{P}\widetilde{\boldsymbol{M}}_{\mathrm{w}}. \tag{4.5}$$

Where, $\boldsymbol{P} = \boldsymbol{H}_{\mathrm{r}}\boldsymbol{P}_{\mathrm{o}}\boldsymbol{D} = \begin{bmatrix} P_{11} & P_{12} & P_{13} & P_{14} \\ P_{21} & P_{22} & P_{23} & P_{24} \\ P_{31} & P_{32} & P_{33} & P_{34} \end{bmatrix}$, is known as the camera projection matrix.

Hence the camera is considered as a system that depends upon the five intrinsic parameters (fk_u, fk_v, u_0, v_0 and θ), and six extrinsic parameters (three each for rotation and translation), which transform a world coordinate to an image coordinate.

Let us consider a stereoscopic system consists of two cameras. A schematic of this stereoscopic system is shown in Fig. 4.1. The symbols used in this figure have the usual meaning as described in previous paragraphs. The full stereoscopic equation for these two views can be set-up by applying the pinhole camera equation (Eq. 4.5) to each of the 3D to 2D projective transformation. Applying the camera equation to the observation point-1 and expanding the matrix, one can get a relation for the image coordinates u and v of the form,

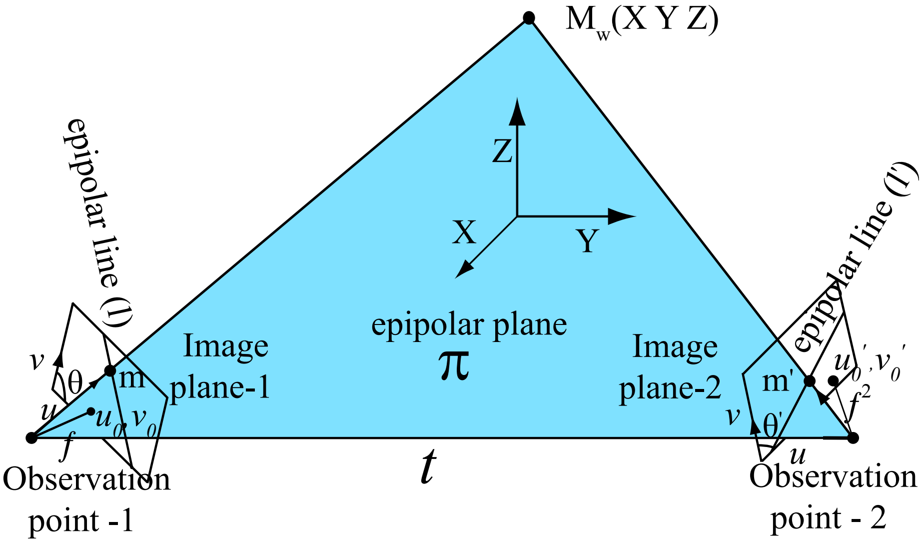

Figure 4.1 Schematic of stereoscopic measurement principle.

$$\begin{cases} P_{14} - uP_{34} = (uP_{31} - P_{11})X + (uP_{32} - P_{12})Y + (uP_{33} - P_{13})Z \\ P_{24} - vP_{34} = (vP_{31} - P_{21})X + (vP_{32} - P_{22})Y + (vP_{33} - P_{23})Z. \end{cases} \tag{4.6}$$

Similarly, applying the above procedure for the observation point-2 ($s'\widetilde{\boldsymbol{m}}' = \boldsymbol{P}'\widetilde{\boldsymbol{M}}_{\mathrm{w}}$), the relation for the image coordinates *u'* and *v'* can be written as,

$$\begin{cases} P'_{14} - u'P'_{34} = (u'P'_{31} - P'_{11})X + (u'P'_{32} - P'_{12})Y + (u'P'_{33} - P'_{13})Z \\ P'_{24} - v'P'_{34} = (v'P'_{31} - P'_{21})X + (v'P'_{32} - P'_{22})Y + (v'P'_{33} - P'_{23})Z. \end{cases} \tag{4.7}$$

Combining the Eqn. 4.6 and Eqn. 4.7 and writing it in matrix form, the complete stereoscopic equation can be written as,

$$\begin{bmatrix} P_{14} - uP_{34} \\ P_{24} - vP_{34} \\ P'_{14} - u'P'_{34} \\ P'_{24} - v'P'_{34} \end{bmatrix} = \begin{bmatrix} uP_{31} - P_{11} & uP_{32} - P_{12} & uP_{33} - P_{13} \\ vP_{31} - P_{21} & vP_{32} - P_{22} & vP_{33} - P_{23} \\ u'P'_{31} - P'_{11} & u'P'_{32} - P'_{12} & u'P'_{33} - P'_{13} \\ v'P'_{31} - P'_{21} & v'P'_{32} - P'_{22} & v'P'_{33} - P'_{23} \end{bmatrix} \times \begin{bmatrix} X \\ Y \\ Z \end{bmatrix}. \tag{4.8}$$

By knowing the projection matrix, and the image coordinates for each camera, the world point ($\boldsymbol{M}_{\mathrm{w}}$ = [X Y Z]) can be found easily from the above relation.

4.3 Pixel correspondence

In previous section, a detail about the stereoscopic principle has been described. At this point, another problem comes in the stereo problem is the pixel correspondence between two camera images. Simply to say, if the image point of the world scene in one of the camera image is known; we have to find the image coordinate corresponding to the world point in other camera image. As there are large number of pixel points in each image, it is time consuming as well as difficult to find out the exact image coordinate. This problem can be solved by the use of epipolar geometry concept [82].

The epipolar geometry is the intrinsic projective geometry between two camera views. It is independent of scene structure, and only depends on internal parameters and relative pose of the cameras'. As shown in Fig. 4.1, suppose a point $\boldsymbol{M}_{\mathrm{w}}$ in 3D-space is imaged in two views, at $\boldsymbol{m}$ in the image-1, and $\boldsymbol{m}'$ in the image-2. It can be seen from the figure that the image points $\boldsymbol{m}$ and $\boldsymbol{m}'$, space point $\boldsymbol{M}_{\mathrm{w}}$, and the camera centers are coplanar. Let us denote this plane as π. From above discussion we can say that the ray corresponding to the unknown point $\boldsymbol{m}'$ lies in π, hence the point $\boldsymbol{m}'$ lies on the line of intersection $\mathbf{l}'$ of π with the second image plane. This line $\mathbf{l}'$ is the image in the second view of the ray back-projected from $\boldsymbol{m}$. Therefore to search the point corresponding to $\boldsymbol{m}$, we need not to cover the entire image plane but can be restricted to the line $\mathbf{l}'$ only. The mathematical representation of the epipolar geometry can be formulated by the using fundamental matrix.

For a given a pair of images, to each point $\boldsymbol{m}$ in one image, there exists a corresponding epipolar line $\mathbf{l}'$ in the other image. Any point $\boldsymbol{m}'$ in the second image matching the point $\boldsymbol{m}$ must lie on the epipolar line $\mathbf{l}'$. Thus, there is a map ($\boldsymbol{m} \mapsto \mathbf{l}'$) between point and line. This projective mapping from point to line is represented by a matrix $\boldsymbol{F}$, called the fundamental matrix. For any point $\boldsymbol{m}$ in the image-1, the corresponding epipolar line is $\mathbf{l}' = \boldsymbol{F}\widetilde{\boldsymbol{m}}$. Similarly, $\mathbf{l} = \boldsymbol{F}^T\widetilde{\boldsymbol{m}}'$ represents the epipolar line corresponding to $\boldsymbol{m}'$ in the second image

The fundamental matrix satisfies the condition that, for any pair of corresponding points $\boldsymbol{m}$ and $\boldsymbol{m}'$ in the two images

$$\widetilde{\boldsymbol{m}}'^{\mathrm{T}}\boldsymbol{F}\widetilde{\boldsymbol{m}} = 0. \tag{4.9}$$

The application of this equation for fundamental matrix calculation and stereo point extraction is described in next section

4.4 Instrumentation and Camera Calibration

The application of the stereoscopic principle makes it possible to observe the pellet ablation behavior three-dimensionally in LHD. Application of the above technique for 3D measurement is divided into two parts such as (1) Instrumentation, and (2) Calibration.

4.4.1 Instrumentation

The lifetime of the pellet in the plasma is of few milli-second, and the dynamics of the pellet changes in microseconds time scale, therefore a fast camera is needed for the pellet ablation studies. The camera used in this system (Vision Research, Inc. Phantom v710) is equipped with a 12-bit self-resetting complementary metal-oxide semiconductor SR-CMOS sensor. The resolution of this camera is (512 × 232) pixels. The camera is operated at a frame rate of 20-50 kHz with 5-20 μs exposure time. A bundled imaging fiber with bifurcation at the imaging end is used for the pellet ablation imaging. To maintain the simultaneity of the measurement, the images from the two locations are focused on to a single fast camera. A schematic diagram of the complete stereoscopic camera system is shown in Fig. 4.2. The overall length of the fiber is 15 m including the bifurcation end of 5 m length. Each of the bifurcated ends has an objective lens of field of view 15°. The bundled end has an imaging lens mounted to the camera, which can project the image pair onto the imaging sensor.

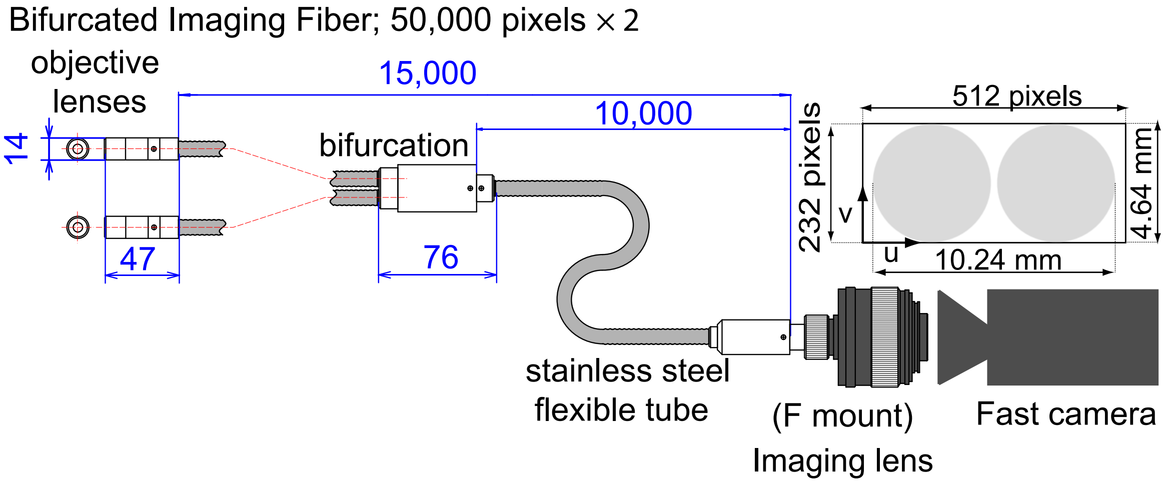

Figure 4.2 Stereoscopic diagnostic setup with fast camera and bundled fiber.

4.4.2 Camera Calibration

The calibration of the stereogram is basically finding of the projection matrix for each camera view, and the Fundamental matrix between the image pairs. These matrixes are calculated by following procedure.

At the first step, a model plane of 5×5 squared grid points is taken for the camera calibration process. The origin of the camera set-up is fixed at one of the imaging port. The Z - direction of the set-up is considered as the pellet injection direction. The X and Y coordinates represent the vertical and toroidal direction of the plasma, respectively. The points in the model plane are separated by 80 mm in both directions. A schematic of this calibration set-up is shown in Fig. 4.3. For any

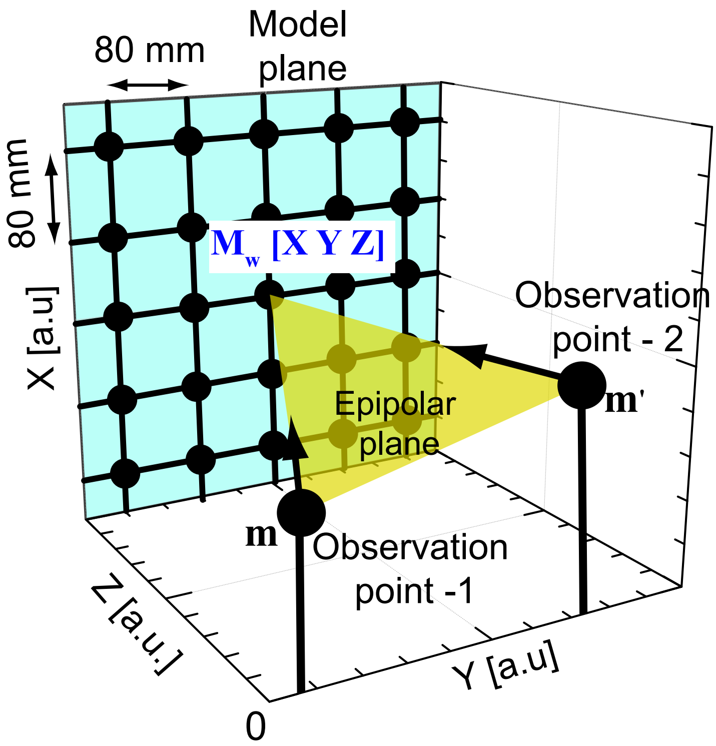

Figure 4.3 Camera calibration setup. The coordinates X, Y and Z represent the plasma vertical, toroidal, and the pellet injection direction of the plasma, respectively. The epipolar plane corresponding to a world coordinate is also indicated.

world point $\boldsymbol{M}^{\mathrm{j}}_{\mathrm{w}}$, the relation (Eq. 4.6) between the three-dimensional point on the model plane and the two dimensional point on the image plane can be written as,

$$\begin{cases} X_jP_{11}+Y_jP_{12}+Z_jP_{13}+P_{14}-u_jX_jP_{31}-u_jY_jP_{32}-u_jZ_jP_{33}-u_jP_{34}=0 \\ X_jP_{21}+Y_jP_{22}+Z_jP_{23}+P_{24}-v_jX_jP_{31}-v_jY_jP_{32}-v_jZ_jP_{33}-v_jP_{34}=0 \end{cases} \tag{4.10}$$

The projection matrix contains 12 elements; therefore at least six pairs of image points are needed to solve the above equation for matrix elements. However, a better solution can be obtained by including more number of known calibration points. In this calibration, the image of the model plane is taken at 14 different Z values, ranging from 2.35 m to 3.0 m. Therefore a total of (5×5×14) 350 points are used to estimate the projection matrix. For n pairs of 3D to 2D correspondence, n equations can be set up as in Eq. 4.10, and can be written as,

$$\mathbf{Ap} = \mathbf{0}. \tag{4.11}$$

Here,

$$\mathbf{A} = \begin{bmatrix} X_1 & Y_1 & Z_1 & 1 & 0 & 0 & 0 & 0 & -u_1X_1 & -u_1Y_1 & -u_1Z_1 & u_1 \\ 0 & 0 & 0 & 0 & X_1 & Y_1 & Z_1 & 1 & -v_1X_1 & -v_1Y_1 & -v_1Z_1 & v_1 \\ \vdots & \vdots & \vdots & \vdots & \vdots & \vdots & \vdots & \vdots & \vdots & \vdots & \vdots & \vdots \\ X_n & Y_n & Z_n & 1 & 0 & 0 & 0 & 0 & -u_nX_n & -u_nY_n & -u_nZ_n & u_n \\ 0 & 0 & 0 & 0 & X_n & Y_n & Z_n & 1 & -v_nX_n & -v_nY_n & -v_1Z_n & v_n \end{bmatrix},$$

and $\mathbf{p} = [P_{11}, P_{12}, P_{13}, P_{14}, P_{21}, P_{22}, P_{23}, P_{24}, P_{31}, P_{32}, P_{33}, P_{34}]^T$.

The solution of the above equation is given by the eigenvector of $\mathbf{A}^T\mathbf{A}$ associated with smallest eigenvalue. The solution of this equation gives the matrix elements of the projection matrix. After finding the projection matrix for both the camera, another important matrix needed is the fundamental matrix between the two camera views. This can be obtained by applying the following procedure.

For any pair of correspondence between $\boldsymbol{m} \leftrightarrow \boldsymbol{m}'$, the fundamental matrix is defined by the relation $\widetilde{\boldsymbol{m}}'^{\mathrm{T}}\boldsymbol{F}\widetilde{\boldsymbol{m}} = 0$. As the matrix $\boldsymbol{F}$ has 9 components, at least 9 corresponding points between the two images are necessary. In particular, writing the left and right image coordinates in its homogenous form $\widetilde{\boldsymbol{m}} = [u, v, 1]^T$ and $\widetilde{\boldsymbol{m}}' = [u', v', 1]^T$, the fundamental relation can be expanded as,

$$u'uf_{11} + u'vf_{12} + u'f_{13} + v'uf_{21} + v'vf_{22} + v'f_{23} + uf_{31} + vf_{32} + f_{33} = 0. \tag{4.12}$$

Above equation can be expressed as a vector inner product, $(u'u, u'v, u', v'u, v'v, v', u, v, 1)\mathbf{f} = 0$. For a set of n matching points (350 points in calibration), the set of linear equations is of the form,

$$\mathbf{Af} = \begin{bmatrix} u'_1u_1 & u'_1v_1 & u'_1 & v'_1u_1 & v'_1v_1 & v'_1 & u_1 & v_1 & 1 \\ \vdots & \vdots & \vdots & \vdots & \vdots & \vdots & \vdots & \vdots & \\ u'_nu_n & u'_nv_n & u'_n & v'_nu_n & v'_nv_n & v'_n & u_n & v_n & 1 \end{bmatrix} \mathbf{f} = 0. \tag{4.13}$$

The solution of this equation can be found by the similar mathematical procedure followed in case of the projection matrix estimation. Before calculating the projection matrix or fundamental matrix, if input data points (3D or 2D) are normalized, a better solution can be obtained [83].

After the estimation of the fundamental matrix, the robustness of this solution is checked by drawing the epipolar lines on the right image, corresponding to a number of points in the left image. An example of this is shown in Fig. 4.4. The figure represents one image frame of the model plane, taken by the fast camera from two different locations during the calibration process. The left half image (here after, "left image") and the right half image (here after,"right image") of this figure correspond to the camera image taken from the observation point-1 and -2 respectively. A solid circle indicates the origin of reference of the model plane with arrows in the left and right image. The cross symbols in the left and right image within the rectangle are the points used in the calibration process to estimate the fundamental matrix $\boldsymbol{F}$. The epipolar lines for a number of point in the left image (calibrated and uncalibrated) are calculated by using the fundamental matrix $\boldsymbol{F}$, and is shown on the right image. In the right image small squares of side 3 pixel length are plotted around the actual model plane points. It can be infer from the figure that the epipolar lines calculated, lies very close to the actual points with error less than ±3 pixels. This proves the effectiveness of the calibration matrixes.

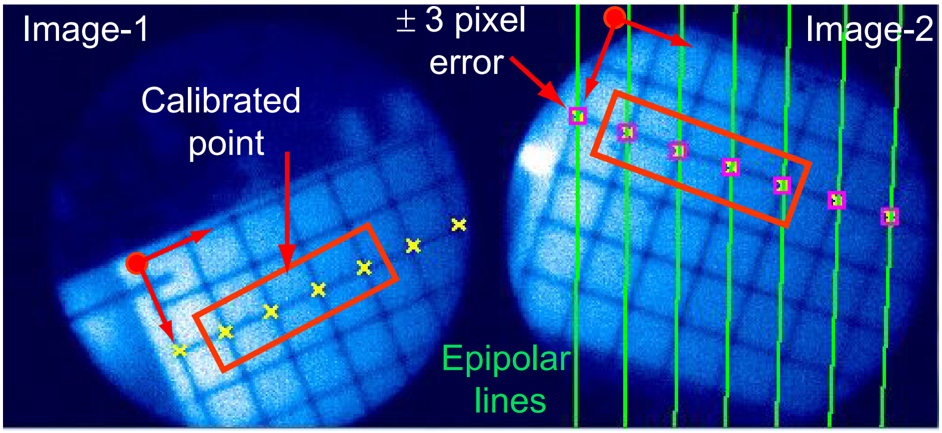

Figure 4.4 Epipolar lines (in right half image) corresponding to a number of points in the left image shows the closeness of the estimated points to the actual points.

After the estimation of the projection matrixes and the fundamental matrix, the accuracy of the stereoscopic measurement system is evaluated by comparing the reconstructed 3D points with the model plane coordinates. Initially the pixel error was ±3 pixels, but following a least square optimization process using the Levenberg - Marquardt algorithm [84], the error reduces to $< \pm 1$ pixel. The reconstructed 3D-position error in the direction of the pellet penetration (Z- direction) to the plasma and transverse to it, is shown in Fig. 4.5. In Figure 4.5 (a), only seven Z - position ($25 \times 7 = 175$) data points are shown. The error bar corresponds to the error of ±20 mm. The maximum error along the Z - direction is estimated as, ±18 mm. Figure 4.5 (b) shows the model plane and the reconstructed $X - Y$ plane coordinates for all 350 points used in the calibration. A bounding circle of same radius indicates an error of 10 mm. Each circle contains 14 recalculated Z - data points. The reconstructed X, Y points are well inside the circle and the reconstruction error is $< \pm 5$ mm. The pellet plasmoid (ablated ionized pellet cloud) size is approximately 50 cm long and 20 cm wide. Therefore this accuracy is sufficient to measure the pellet dynamics inside the plasma.

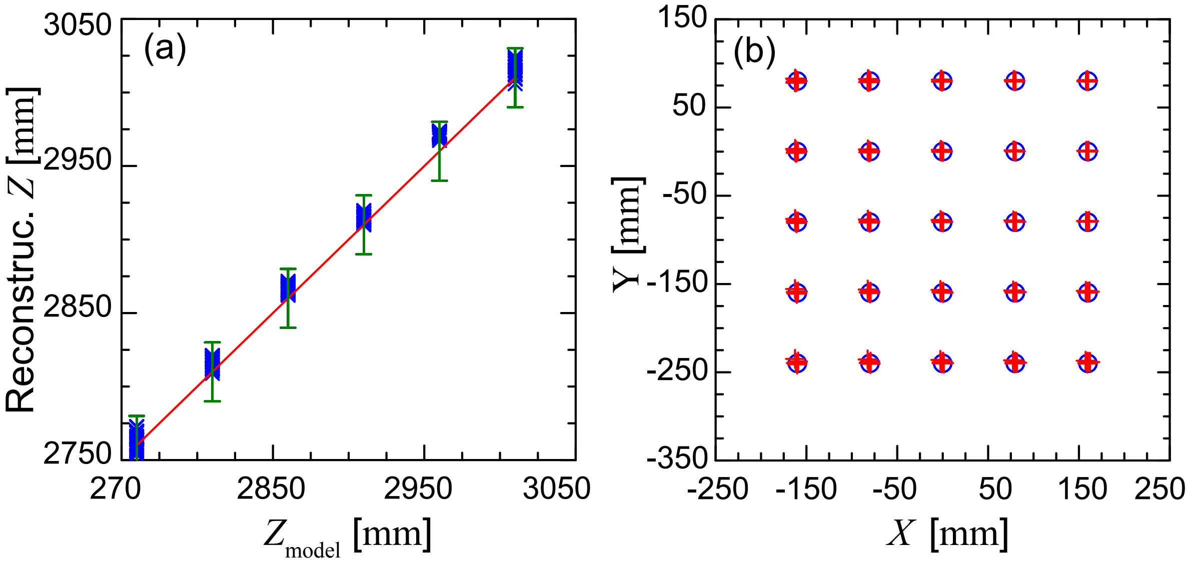

Figure 4.5 (a) Stereo reconstructed error along Z direction (Maximum error ±18 mm). (b) Error in in $X - Y$ direction for all Z-positions. An error of 10 mm is indicated by the bounding circles of 10 mm radius.

4.4.3 Application to pellet ablation study

The application of the stereoscopic camera to an ablating pellet in the LHD plasma is demonstrated in Fig. 4.6. This figure shows the typical stereo pair of an ablating pellet cloud inside the plasma. It can be observed that the pellet ablation cloud intensity has a peaked profile. Considering a strong intensity of the ablating cloud near the pellet surface, it can be assumed that pellet lies in the brightest part of the image. Accordingly, a cross in the left image indicates the position of the pellet. To find the corresponding point in the right image; an epipolar line is drawn by using the equation 4.9. The pixel coordinates of the pellet in the right image (cross symbol) is calculated by assuming that it lies on the brightest point along the epipolar line. By knowing the coordinates for both image and using the projection matrix, the three-dimensional position of the pellet can be found from the Eqn. 4.8. Using the above method, the pellet motion inside the plasma is calculated and is plotted in Fig. 4.7. The solid line in the figure represents the presumed pellet

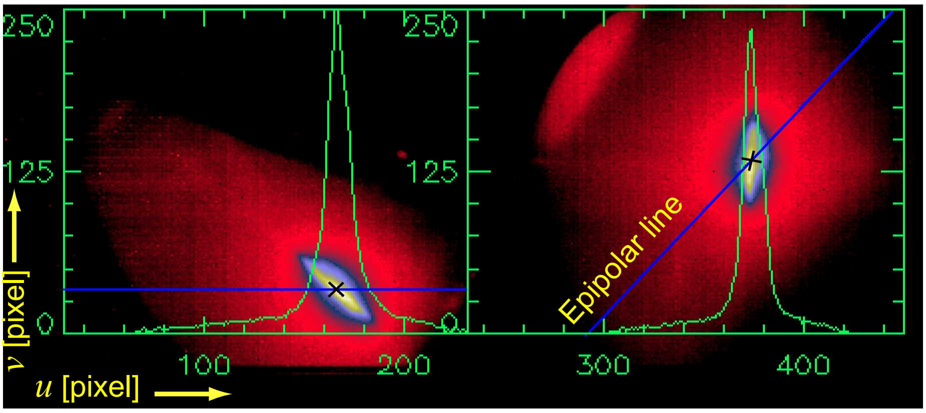

Figure 4.6 A typical picture of an ablating pellet image taken from two different locations. The epipolar line corresponding to the pellet position in left image is shown on right image

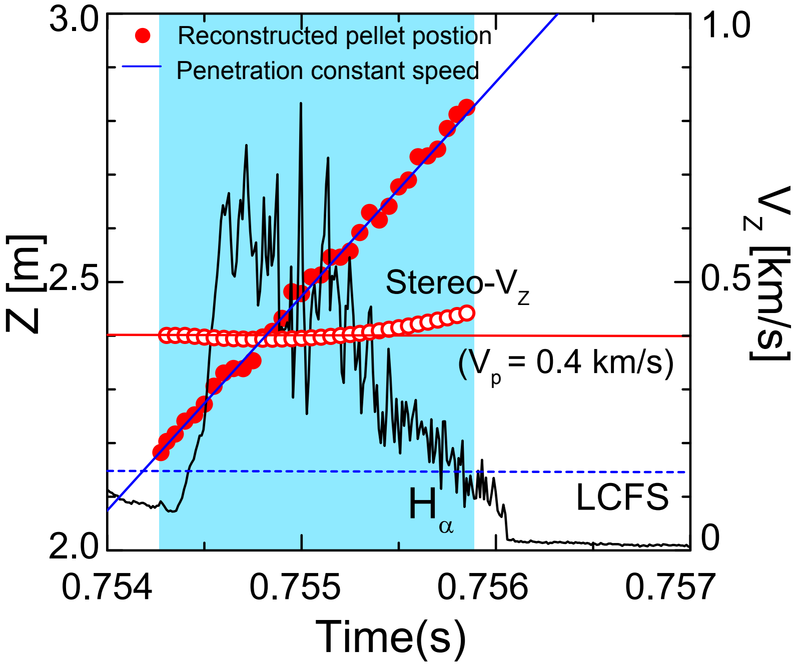

Figure 4.7 Time evolution of the stereo reconstructed pellet position and H_α ablation intensity. Predicted pellet position by considering the constant pellet speed is indicated by the solid line. The open circles show the stereo reconstructed pellet penetration speed.

position inside the plasma by considering the constant pellet speed along the pellet path. The H_α light originated due to the pellet ablation is also shown. The pellet speed along the penetration direction is calculated by polynomial fitting of the pellet position data, and matches well with the pellet injection speed. It can be said that, the pellet ablation dynamics inside the plasma can be successfully diagnosed by using this stereoscopic diagnostic method. Pellet ablation study applying this technique is discussed in subsequent chapters.

4.5 Summary

In LHD, due to three-dimensional plasma configuration, complicated pellet plasma interaction can be predicted. The external helical coils restrict the use of perpendicular observation ports for three-dimensional pellet ablation imaging on the same poloidal location. Therefore, a three-dimensional diagnostics by applying the stereoscopic principle is calibrated to study the pellet-plasma interaction in LHD. In this technique, the ablation pellet cloud is imaged from two arbitrary locations by using a single fast camera and bifurcated coherent bundle fiber. Stereoscopic observation system has been calibrated by using a model plane of 25 grid points for fourteen different Z positions along the pellet injection direction. In the calibration process, two projection matrixes for each observation point and a fundamental matrix relating the two camera images has been estimated with good accuracy. The stereo reconstructed error is found to be ±18 mm along the pellet injection direction and ±5 mm transverse to it. Successful application of this diagnostic to the pellet injection experiments is demonstrated by comparing the estimated pellet position with the predicted position by considering the constant speed of the pellet along its injection direction.

Chapter 5

Stereoscopic observation of the pellet ablatant in LHD

5.1 Introduction

In order to understand the fueling process in the plasma, study of the pellet ablation is very important, as it governs the pellet penetration inside the plasma. The pellet injected into high temperature plasmas is mainly ablated by thermal electrons. The energetic ions produced in the presence of external heating plays a significant role in the ablation process. High temperature plasmas with higher heating power increases the pellet ablation rate due to increase in the heat flux on its surface, which in turn reduces the pellet penetration. With increase in heating power, degradation of the fueling efficiency has also been reported from tokamak [85]. In addition, the pellet trajectory deviation from its injection direction can also affect the fueling factor by reducing the pellet penetration into the plasma. In simplistic assumption, the pellet penetration depth inside the plasma is measured by the product of H_α intensity time duration, and the injection speed, owing to the fact that pellet travels with constant speed along its injection path. In the case of a non ideality in the pellet trajectory (change in speed and / or deviation from injection direction), this simple assumption for estimation of the pellet trajectory may cause an error in measured penetration depth [86]. The non ideality in the pellet trajectory is inherently depends on the distribution of the energetic particles inside the plasma. The heat flux by the plasma particles onto the pellet surface is carried along the magnetic field lines through the ablation cloud. The particles with smaller gyro radius than the cloud radius can penetrate in to the plasma. Therefore the ablation characteristics depend on the energy distribution of these particles. In converse, the pellet trajectory deflection has been used as a tool to estimate the distribution of energetic particles in Reverse Field Experiment (RFX) [87], and current distribution during magnetic reconnection in tokamak [88]. The pellet trajectory deflection using a Carbon pellet is also used as a diagnostic tool to measure the local current density profile in the T-10 Tokamak [89]. In order to study the pellet ablation process in high temperature plasmas, a clear understanding of the interaction between the pellet and the energetic particles is necessary.

LHD, a heliotron type device has a three dimensional magnetic field configuration. Since, NBI is the main source of the plasma heating in the pellet injected discharges, the fast ions generated due to it plays a significant role in the pellet ablation process [90]. In connection with this, two dimensional observation of the pellet trajectory in the presence of NBI has been reported earlier in LHD [91]. In that study it had been reported that, the trajectory of the pellet deflects along the toroidal direction with respect to the tangential neutral beam direction. In the case of a three dimensional magnetic configuration, deflection of the pellet trajectory in 3D plane cannot be ruled out. Due to monocular observation, previous study performed in LHD by using the fast camera cannot reveal the three dimensional characteristics of the ablating pellet. Therefore, in order to get a deeper understanding of the pellet penetration process inside the plasma, a three-dimensional measurement system is necessary. Using the perpendicular observation ports from the tangential view and the poloidal view, three dimensional pellet imaging studies have been performed with the help of the position sensitive detector or the CCD camera in RFX and AUG tokamak, respectively [76,78]. Using a 2D position sensitive detector, and knowing the injection speed and lifetime, 3D position of the pellet had been estimated, in LHD [77]. In presence of non-ideality in the pellet penetration, estimation of the local pellet position considering the constant pellet speed can lead to wrong result. Therefore, this diagnostic is not able to measure the exact penetration depth of the pellet independent of its injection history. In presence of the helical coils perpendicular observation ports are limited. Therefore, stereoscopic technique has been applied as a diagnostic tool to analyze the pellet ablation behavior in the LHD [80].

5.2 Experimental setup

In LHD, neutral beam injection is used as the main source of auxiliary heating in pellet injected discharges. LHD is equipped with three negative-ion based tangential NBI systems of total power 15 MW with a beam energy of 150 -180 keV for plasma heating [26]. While NBI-1 and NBI-3 are operated in counter clock wise (CCW) direction, NBI-2 is operated in clock wise (CW) direction. The pellet ablation behavior has been investigated in presence of two types of NBI heated plasmas such as CW NBI and CCW NBI. In the case of the CW NBI, the plasma major radius and the toroidal magnetic field is of 3.65 m and 2.71 T, respectively. The corresponding values in the case of the CCW NBI are 3.75 m and 2.64 T, respectively. The plasma averaged minor radius is 0.6 m. Since the magnetic confinement field is generated externally by $l/m = 2/10$ continuous superconducting helical coils, the magnetic flux surface rotates between a horizontally and vertically elongated elliptical plasma cross-section. Due to high rotational transform at the plasma edge, the pitch of the magnetic field line maximum at the plasma edge and it continues decreasing towards the plasma center. A three dimensional view of the LHD plasma with helical coils and pellet injection position is shown in Fig. 5.1(a). LHD is equipped with three different types of pellet injectors namely; a multi barrel pipe gun pellet injector [65], a repetitive pellet injector [56], and a punch mechanism based low speed pellet injector [106]. For the experimental results presented in this study, cylindrical pellets (size: 2.5 mm cylindrical and speed: 150-550 m/s) from the repetitive pellet injector were used. A pellet contains 6.6 $\times 10^{20}$ atoms. The pellets were injected in the mid-

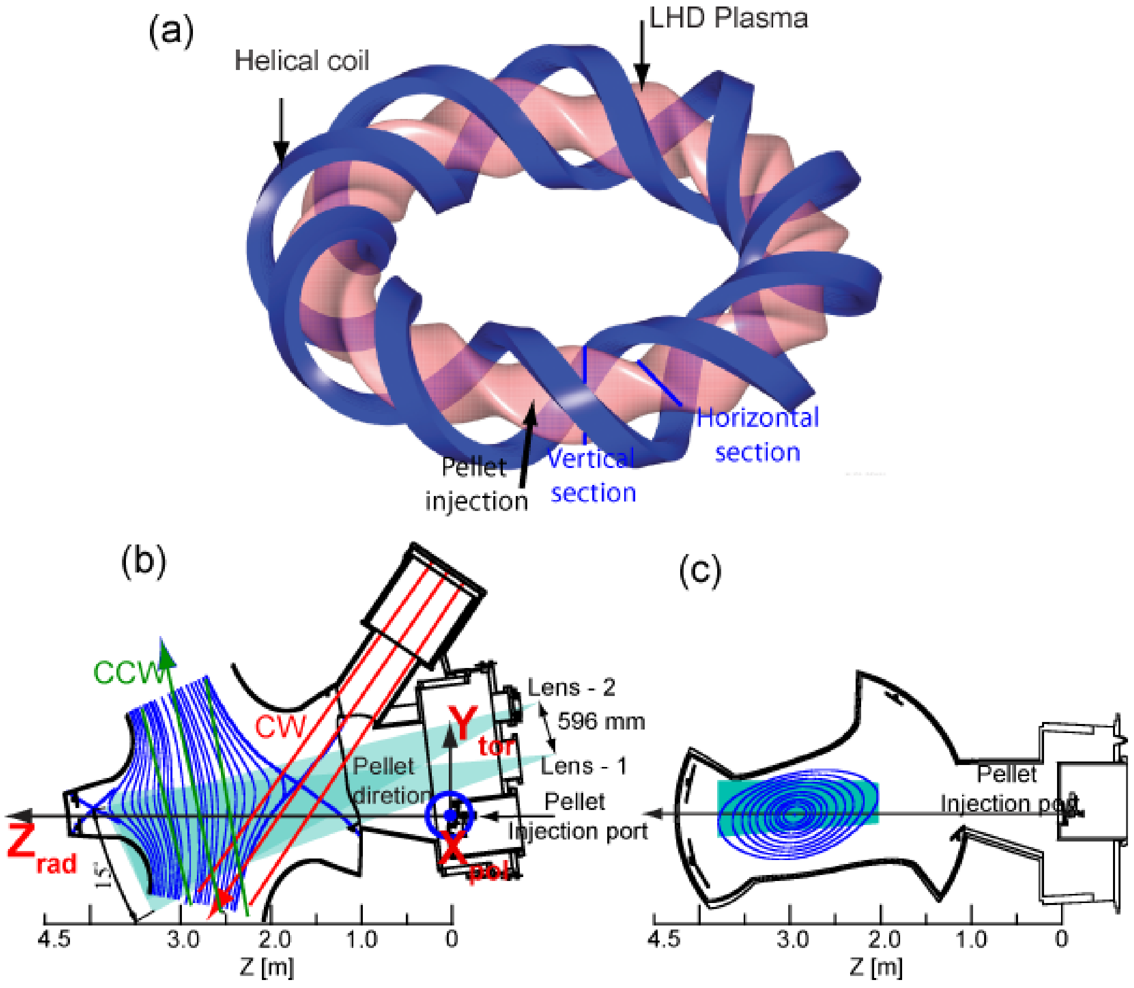

Figure 5.1 (a) Three dimensional view of the LHD plasma with helical coils, (b) Mid-plane top view of pellet injection showing plasma flux surface, pellet injection direction and stereoscopic observation system. (c) Vertical view of injection cross section. Field of view of the camera lenses is shown by the hatched region.

plane of the horizontally elongated section from the torus outboard side, which is the LFS pellet injection in LHD. The Plasma minor radius along the pellet path at this injection cross-section, a, is 0.85 m. A schematic of LHD mid plane (top view) and poloidal section with pellet injection port and the diagnostic ports are shown in Fig. 5.1(b) and (c), respectively. The tangentially applied neutral beam (NB) directions are shown by the parallel bounding lines with arrows at the beam center. The arrows pointing downward and upward, represent the beam direction in the case of CW and CCW NB respectively. The entrance point of the pellet into the LHD vacuum vessel (indicated by a blue circle) is taken as the center of reference of the ablating pellet position inside the plasma. The coordinate axes X_{pol} and Y_{tor} in this reference frame represent the vertical and toroidal direction of the plasma, respectively. The Z_{rad}-coordinate indicated in meters is taken as the pellet injection direction along the negative major radial direction of the vessel. A pellet enters into the plasma at $Z_{\text{rad}} \approx 2.15$ m with respect to the center of reference.

The position of the ablating pellet is measured by using the stereoscopic diagnostic presented in Chap. 4. As shown in the Fig. 5.1(b), a pair of stereo image is obtained from two observation points by using a coherent bundled fiber with bifurcation at the imaging end. The position of each imaging fiber on the observation port is indicated by lens-1 and lens-2, respectively. The two lens positions are separated by 660 mm toroidally and 1030 mm vertically. Each of the bifurcated ends is fitted with an objective lens of field of view 15°. The simultaneity of the two images is maintained by focusing it on to a single fast framing camera. The fast camera (Phantom v710, Vision Research Inc.) used in this system is equipped with a 12 bit self-resetting complementary metal oxide semiconductor (SR-CMOS) sensor. The images are obtained with spatial resolutions of (464 × 192) pixels and temporal resolutions of 50 μs with a 2 μs exposure time. The stereo-reconstructed error of this diagnostic system is approximately 5 mm, 6 mm and 15 mm along X_{pol}, Y_{tor} and Z_{rad} directions, respectively. The initial injection speed of the pellet is obtained by the time of flight between two light gates. A Si-PIN photo diode fitted with a H_α filter (center wavelength: 656.5 nm / half bandwidth: 9.2 nm) measures the pellet ablation light at a time resolution of 1

μs. The plasma electron temperature (T_e) and density (n_e) are measured by 200 point Thomson scattering diagnostics installed at the horizontally elongated section in the plasma mid plane [38].

5.3 Experimental Results

The pellet ablation behavior is investigated in presence of two types of NBI heated plasmas in LHD. The types of discharge considered are CW NBI of 3.7 MW (shot #60825) and CCW NBI of 2.8 MW (shot #59515). The central electron temperatures for these two discharges are 0.95 keV and 0.65 keV, respectively. Typical waveforms for both type of discharges showing deposited NBI power, central electron temperature (T_{e0}), chord averaged density ($\bar{n}_e$), and H$_\alpha$ signal of the ablating pellet is plotted in Fig. 5.2. The T_{e0} is obtained from the Thomson scattering diagnostic, where as the $\bar{n}_e$ is taken from the FIR interferometer signal. The shaded regions in both the figures correspond to the injected pellet timing considered in this study. The H$_\alpha$, and the time integrated camera frame intensity signal for an ablating pellet in both NBI conditions are shown in Fig. 5.3. The pellet ablation time obtained from the H$_\alpha$ signal and the last closed flux surface (LCFS) (where the pellet enters into the core plasma) are indicated by the dashed lines in each figure. A bulging structure in both H$_\alpha$ and camera intensity signals can be observed [Fig. 5.3(a)] outside the LCFS for the CW NBI discharge. However, this kind of structure is absent in the other case [Fig. 5.3(b)]. Similar kinds of structures reappear in both signals in the case of balanced NBI discharges. From the geometry of the injection (Fig. 5.1(b)), it can be seen that the CW NBI beam crosses the injected pellet path before entering into the plasma. The duration of this peak is $\approx$ 0.6 ms, which corresponds to the path length of 0.252 m corresponding to the pellet injection speed of 420 ms^{-1}. The calculated length is comparable to the path of the pellet trajectory under the direct influence of the NB, deduced from the injection geometry. Therefore one can conclude that, the observed bulging structure is due to the direct heating of the pellet by the neutral beam. Furthermore, the contribution of the direct impact of NBI beam to the ablation process can be evaluated as follows. The maximum fast ion density along the toroidal direction in the plasma (n_f) is 1.1×10^{17} m^{-3}

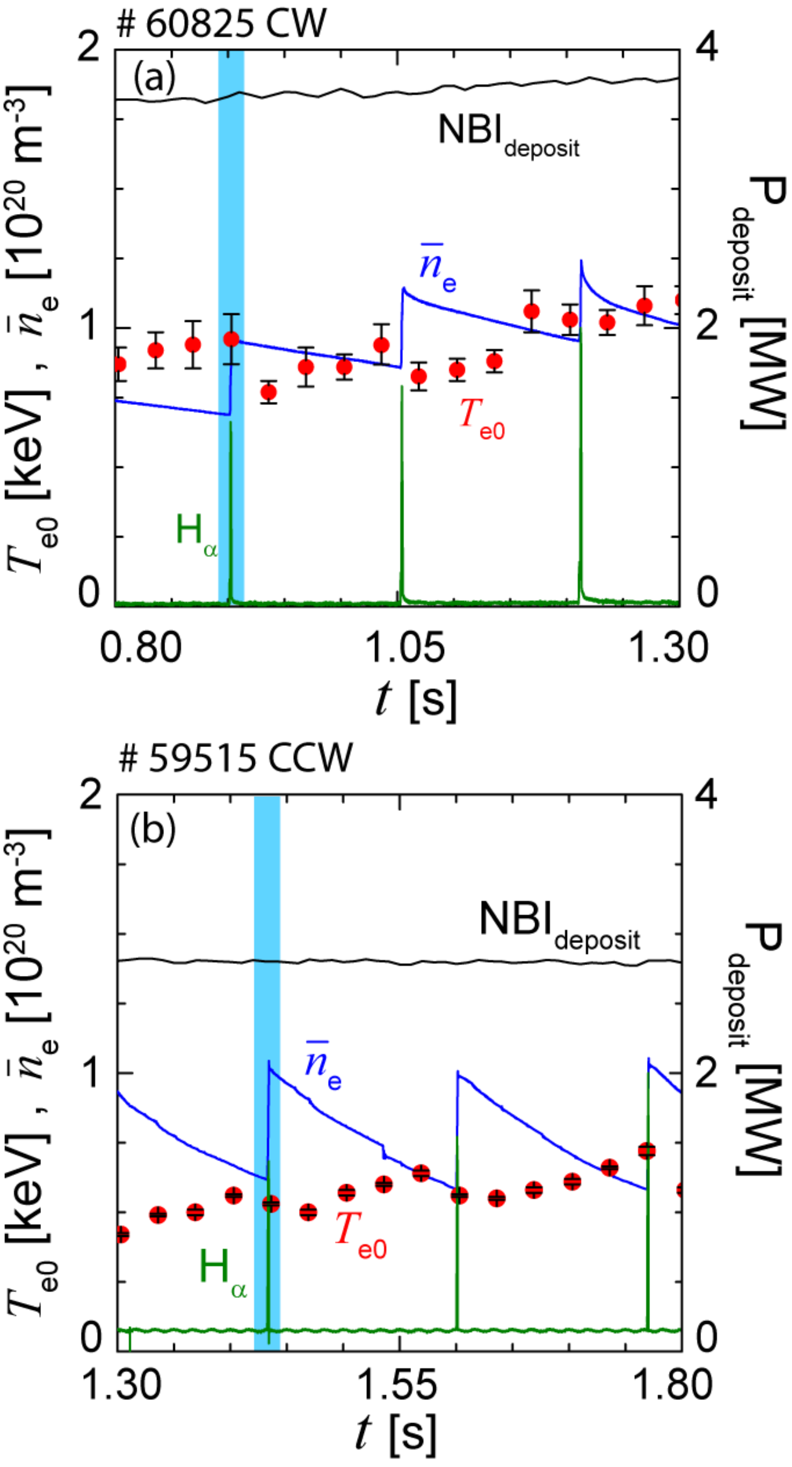

Figure 5.2 Temporal evolution of a typical pellet injected discharge (# 60825: CW-NBI and # 59515: CCW NBI). Shaded region corresponds to the pellet timing considered in this study.

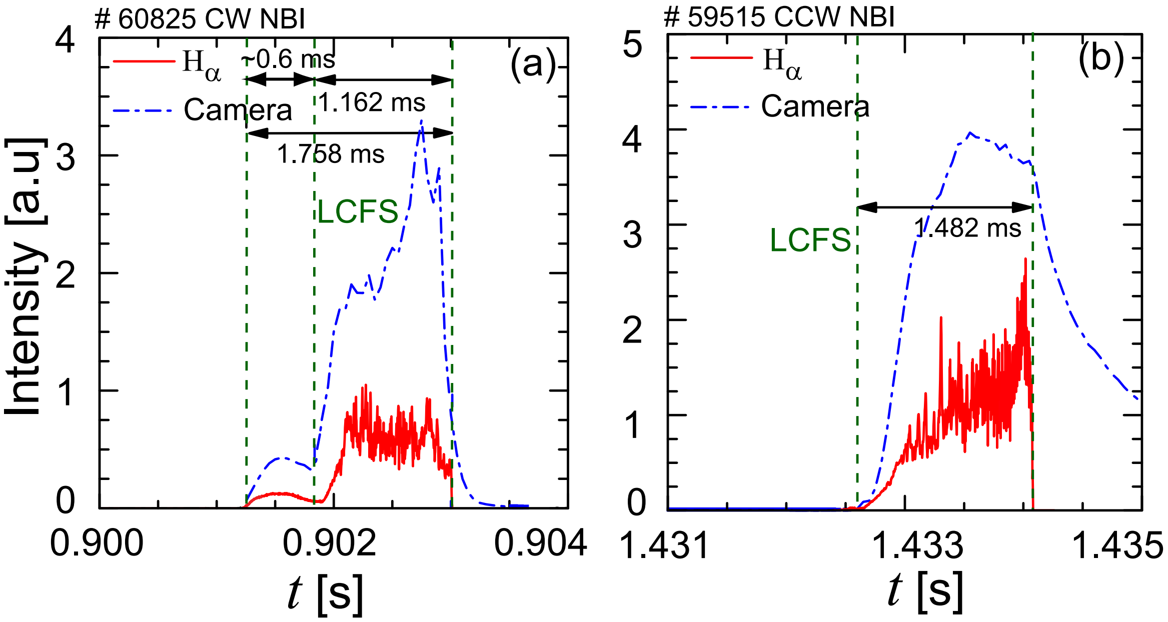

Figure 5.3 H_α and camera intensity signal for CW and CCW NBI case. The last closed flux surface (LCFS) and pellet ablation time are indicated by dashed line in both figure.

(in section 5.4.1). The beam density of the NB (n_b) on its path outside the LCFS is calculated by taking the energy of the beam, E_b = 170 keV, and port through power, P_{port} = 3.7 MW, is 8 $\times 10^{13}$ m^{-3}. Let L_1 is the geometrical path length of the pellet crossing the beam cross section outside LCFS, and L_2 is the path length of the pellet traveling inside the plasma. The values of L_1 and L_2 are 30 cm and 34 cm, respectively. For a simple estimation considering the ablation rate proportional to $n_\mathrm{f}^{1/3}$ [92], the fraction of the contribution (F_th) to the pellet ablation due to the direct heating of the NBI beam can be written as,

$$F_\mathrm{th} = \frac{C_1}{2^{3/2}C_2}\left(\frac{n_\mathrm{f}}{n_\mathrm{b}}\right)^{1/3}\left(\frac{L_1}{L_2}\right). \tag{5.1}$$

The factor $2^{3/2}$ is divided to include the fast ion slowing down factor considering the steady state contribution. Assuming the constants $C_1 = C_2$, and using the corresponding values in Eqn. 5.1, F_th calculated is $\approx$ 3 %. Although, the pellet ablation light measured by the H_α diagnostic depends upon the atomic process in the plasma, for a crude assumption it can be assumed that the H_α signal is proportional to the pellet ablation rate.

At this point, it is worth to consider the contribution of the fast ions and electrons to the pellet ablation. Since the pellet regression rate is a function of the incident particle heat flux, for crude estimation, this contribution is calculated by taking the ratio of the attenuation of the heat source in the cloud from the fast ions and electrons ($R_{\mathrm{f,i}} \equiv W_{\mathrm{f}}/W_{\mathrm{e}}$). This ratio is estimated by taking, $n_{\mathrm{e}} = 5 \times 10^{19}\mathrm{m}^{-3}$ and $T_{\mathrm{e}} = 1$ keV, in present discharge conditions. For simplicity we assume the energy $E = 2T$. Prior to this ratio calculation, the energy loss function and the effective cross section for the electron and the fast ion are evaluated. The effective cross-section for the electrons and ions is given by $\Lambda_{\mathrm{e}}(E_{\mathrm{e}}) \equiv \hat{\sigma}_T + 3L_{\mathrm{e}}(E)/2E_{\mathrm{e}}$, and $\Lambda_{\mathrm{f}}(E_{\mathrm{f}}) \equiv 3L_{\mathrm{f}}(E)/2E_{\mathrm{f}}$, respectively. Here $\hat{\sigma}_T$ represents the total cross section for the elastic back scattering of the electron, and $L(E)$ with subscripts represent the loss function of the corresponding particles in the cloud. The loss function for electrons [46] and fast ions [93] is shown in Fig. 5.4; the effective cross section for electrons and fast ions are also shown. The energy transport to the pellet also depends on the ratio of the

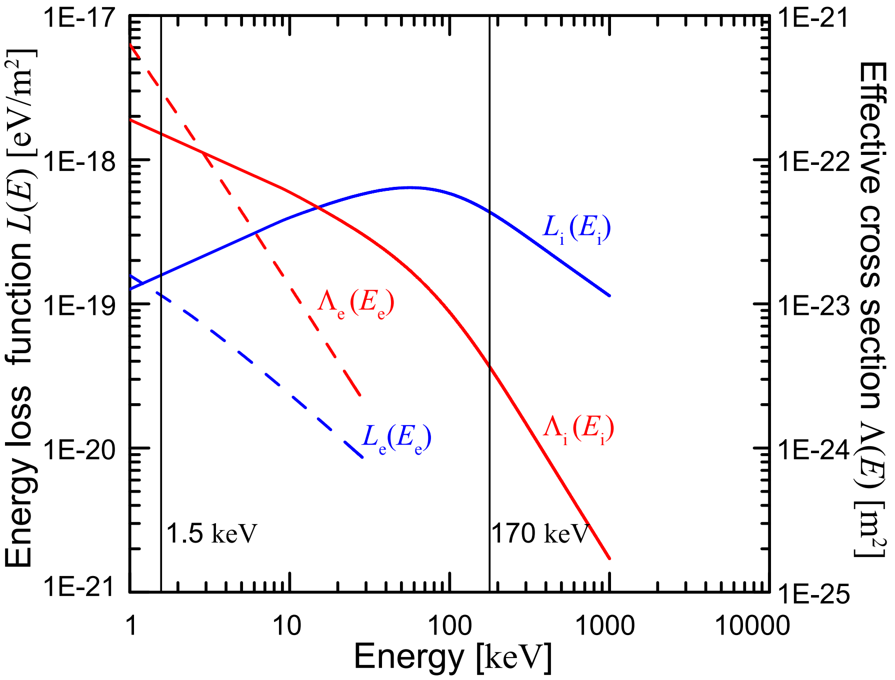

Figure 5.4 Loss function $L(E)$ and effective cross-section $\Lambda(E)$ of electrons and ions

$\sqrt{m_\mathrm{i}/m_\mathrm{e}}$. For low ion energies, since the effective cross section for the electron is comparable with the ions and the mass ratio is less, the electron heat flux is dominant in this region. However, in presence of fast ions with energy 170 keV (in our experiment), the effective cross section for the ions is of two order lower than the electrons. At this situation the ratio, $R_\mathrm{f,i}$, estimated is of the order of 10^{-3}. From the ratio, $R_\mathrm{f,i}$, it can also be evaluated that, at fast ion energies lower than 100 keV, ablation due to electron is dominant. Therefore, the major contribution to the ablation is from the fast ions at higher ion energies. Returning to the discussion for ablation due to the direct impact of NBI, the ratio between the bumped part of the signal outside the plasma and the main signal inside the plasma can be taken as an indicator to calculate the ablation fraction. Taking the time integration of H_α in both the region, ablation fraction from the experiment (F_{exp}) is calculated as $\approx$ 9.5 %, which is 6.5 % more than the theoretical value. Therefore, contribution from direct impact of NBI on the pellet ablation is negligibly small.

The pellet penetration into the plasma is calculated by the stereoscopic image pair. It is well known that the pellet plasmoid (high density ablation cloud) expands along the magnetic field line while entering into the plasma. This fact can be used as a tool to recheck the effectiveness of this diagnostic system by comparing the angle of the elongated plasmoid to the local pitch angle of the magnetic field lines. Since the magnetic confinement field is generated by the external helical coils and LHD plasma has the current-less characteristics, the pitch of the field lines is determined from the magnetic field line tracing. The elongation of the pellet plasmoid along the toroidal direction on the magnetic flux surface for $\rho = 0.8$ is shown in Fig. 5.5(a). Here, a stereo image pair obtained in case of balanced NBI discharge is taken into consideration (the effect of unbalanced case on pellet trajectory will be discussed latter). The left and right images in the figure are of the same pellet taken from two different locations. At first, the position of the pellet at a particular time is estimated by using the stereoscopic diagnostic. This estimated position matches well with the pellet position considering the constant pellet speed and the ablation time. After that, the flux surface (half section of the poloidal view) corresponding to the calculated pellet position is projected (solid lines) on

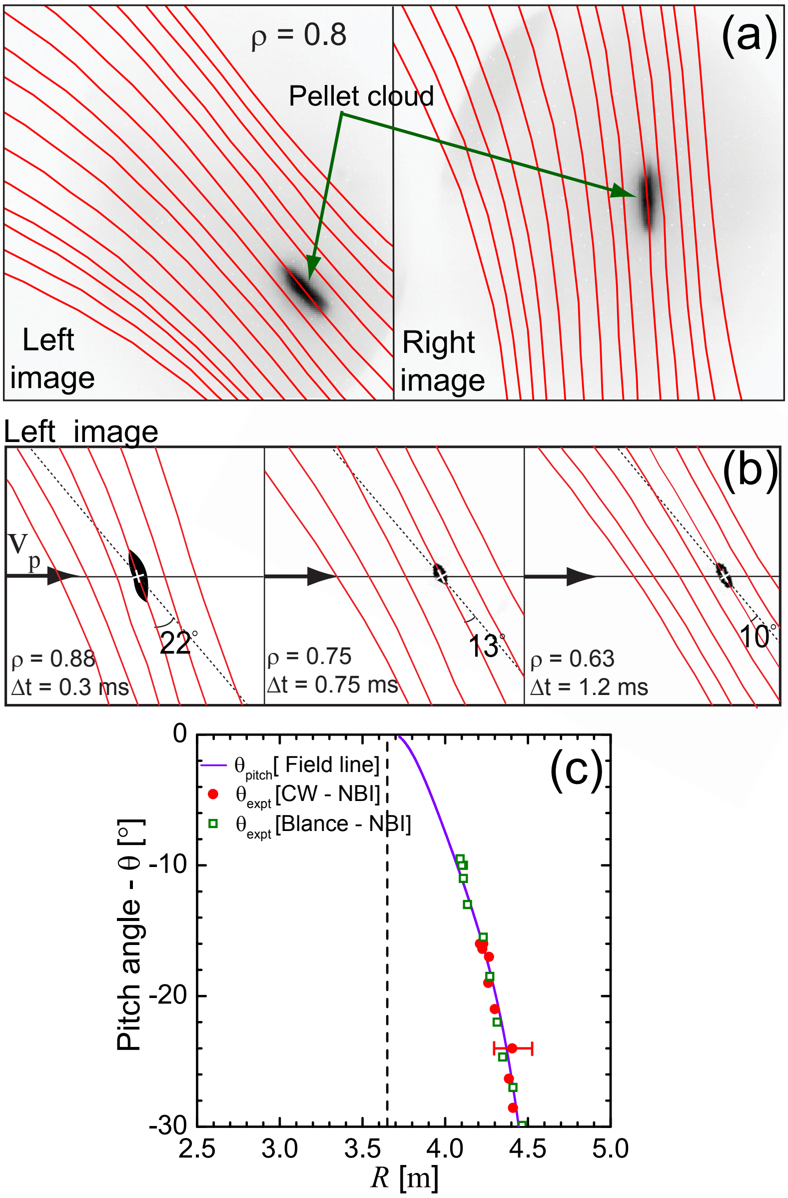

Figure 5.5 (a) & (b) Projection of the magnetic flux surface on the camera image showing elongation of the pellet cloud along the magnetic field lines (solid lines). (b) Change in plasmoid angle with the plasma mid-plane while penetrating into the plasma. (c) Comparison of the pitch of the magnetic field line and the plasmoid angle with the plasma mid-plane, along *R*.

to the image plane on both images. The expansion of the pellet cloud along the toroidal direction matches well with the projected field line with an accuracy of ±2°. Therefore, it validates the effectiveness of this diagnostic system. By taking a sequence of images of the same pellet (Left image), it has been observed that the pellet ablation cloud penetrates into the plasma with some angle to the mid plane and the angle goes on decreasing with penetration (Fig. 5.5(b)). The angle subtended with the mid plane is in close agreement with the pitch of the magnetic field lines. The pitch angle of the magnetic field line is calculated as, $\tan^{-1}[(r/R)(\iota/2\pi)]$. Where r, is the pellet position from the major radius R, and $\iota/2\pi$, is the rotational transform at the corresponding pellet position. A comparison between the ablation cloud angles with the plasma mid plane at various penetration depths along the major radius is shown in Fig. 5.5(c). The error bar (±50 mm) in the figure represents the maximum uncertainty in pellet penetration depth estimation. From this discussion it can be concluded that, the cloud angle with the mid plane can also be used as a parameter to know the approximate location of the pellet inside the plasma.

The trajectory of an ablating pellet in the case of the CW and CCW NBI injected plasma is shown in Fig. 5.6. The pellet position in three dimesnion for CW NBI beam is shown on top of the figure. The planes, $Z_{\text{rad}} - Y_{\text{tor}}$ [5.6(a)] and $X_{\text{pol}} - Z_{\text{rad}}$ [5.6(b)] corresponds to the plasma mid plane (top view) and the poloidal plane, respectively, with respect to the vessel center. The magnetic flux surfaces and the ideal trajectory of the injected pellet are shown by the curved lines and arrows, respectively. The shaded area in these figures represents the viewing area of the observation system. The pellet positions on these planes are calculated with the help of the stereoscopic diagnostic and are shown by the solid circles. The error in measured pellet position, shown in these figures is obtained by considering the width of the ablation light intensity in each image frame. The deflection in pellet trajectory along the toroidal and the poloidal directions in the case of the CW NBI injection is up-to 17 cm and 10 cm, respectively. A similar kind of figure for the pellet in the case of the CCW NBI plasma on the toroidal and vertical plane is shown in Fig. 5.6(c) and 5.6(d), respectively. In this case, although the toroidal deflection is almost similar to that of the

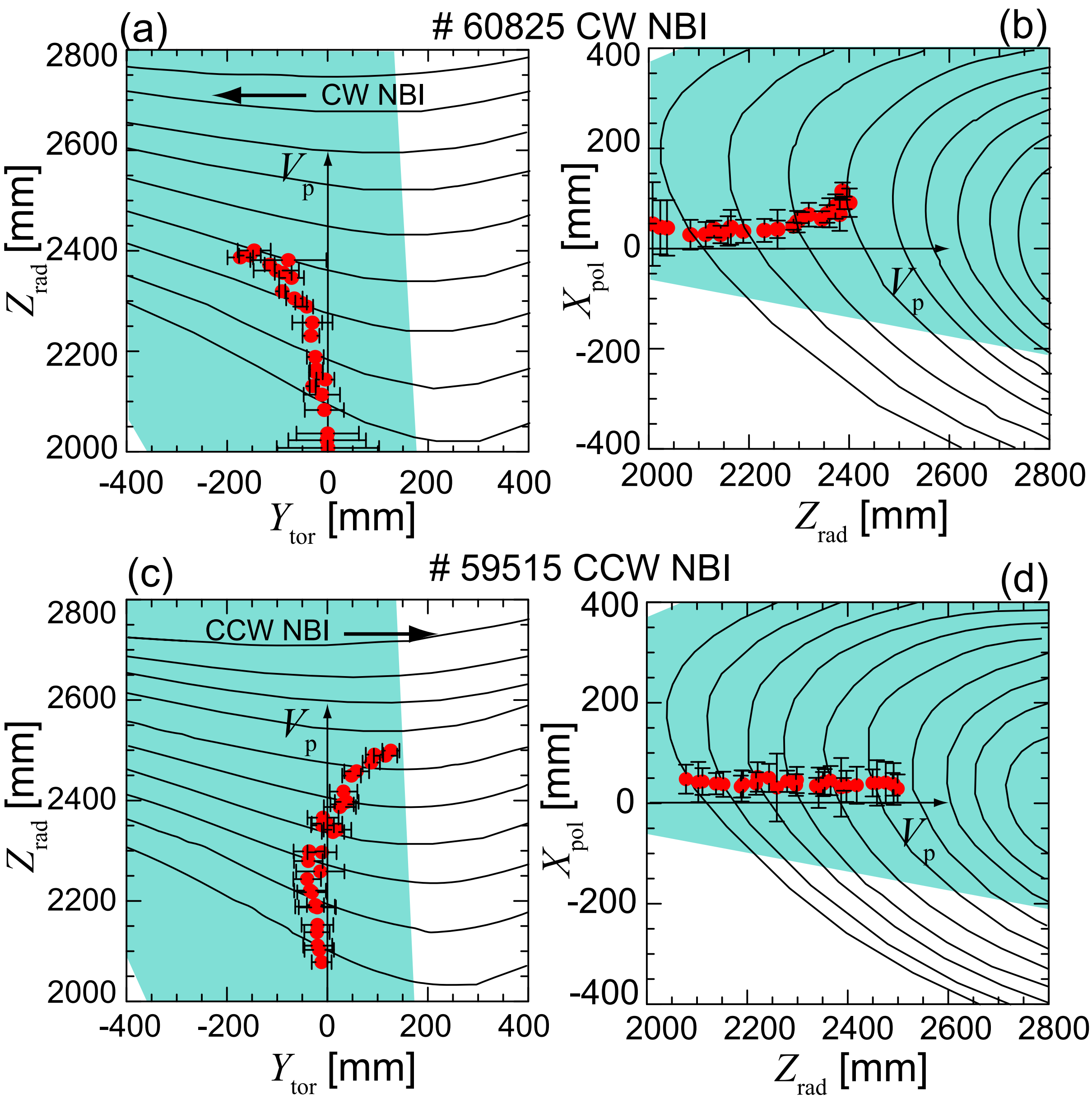

Figure 5.6 (Top) Reconstructed pellet trajectory on (a) toroidal (mid-plane view) and (b) vertical plane of the LHD for CW-NBI injection. Shaded area indicates the viewing area of the observation system. Direction of the pellet injection and tangential NBI are indicated by the arrows. (Bottom) The pellet trajectory on (c) toroidal (mid-plane view) and (d) vertical plane, in the case of the CCW-NBI injection.

CW NBI case, there is no or very less deflection in the vertical direction. Where as the vertical deflection is towards the top of the vessel for CW-NBI, it is downward direction in the case of the CCW-NBI. A case for the small deflection along the vertical direction in the case of the CCW-NBI is shown in Fig. 5.7. The cause of this is discussed in the latter sections. Another observation, that can be marked from the figure is that the radius at which the pellet starts deviating from the injection path (here after it will be designated as "deflection radius") is different in the two cases. A histogram showing the position of the deflection radius for both NBI case is shown in Fig. 5.8. The histograms are obtained by using 20 different pellets for each NB conditions with slightly varying neutral beam powers. On average the curving of the pellet trajectory starts at $\rho \approx 0.84$ - 0.92 in case of CW NBI. Similarly the average deflection radius is more inside the plasma at $\rho \approx$ 0.68 - 0.78 in the CCW NB case. The arrows in the figure represent the deflection radius of the two pellets, presented in this study. Also it has been found that, if the curving of the pellet trajectory starts further out in the plasma (in the CW NBI case), the poloidal deflection is higher. Figure

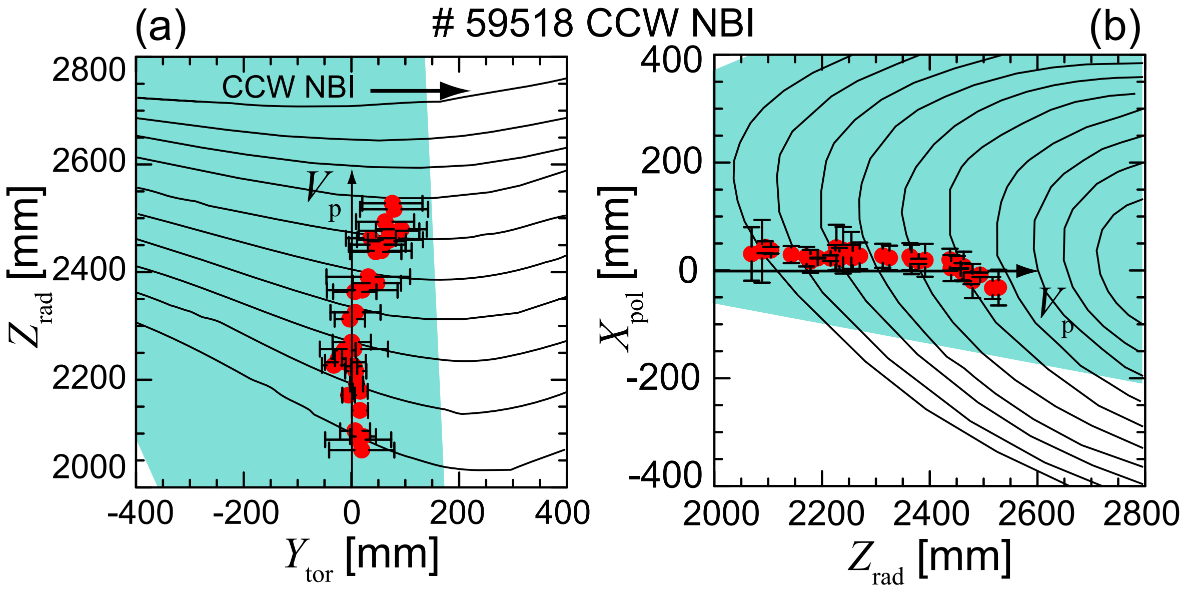

Figure 5.7 Reconstructed pellet trajectory on (a) toroidal (mid-plane view) and (b) vertical plane of the LHD for CCW-NBI injection.

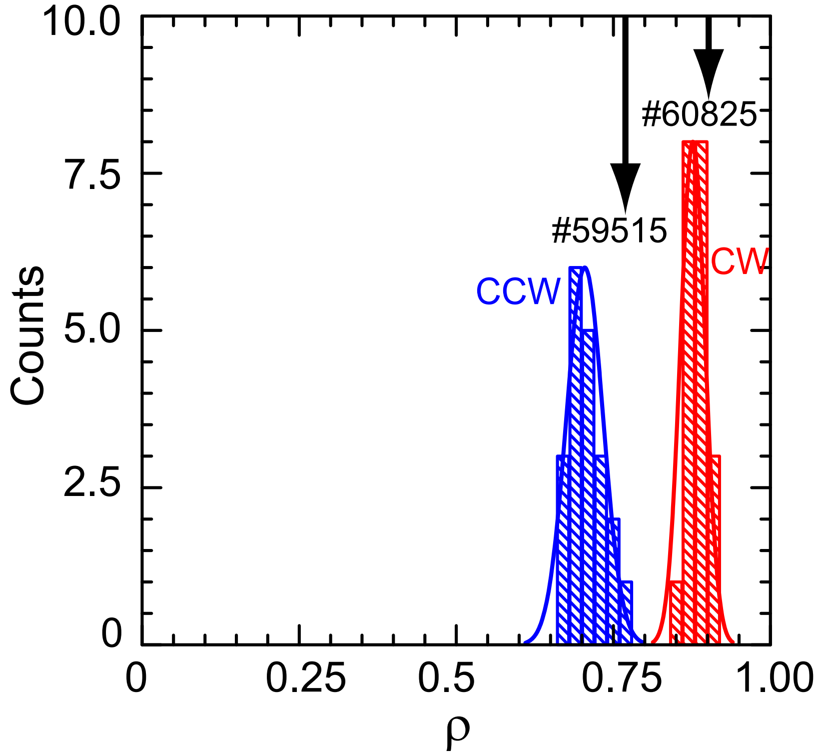

Figure 5.8 Histogram (20 pellets for each case) showing the variation of the deflection radius in presence of CW and CCW NBI conditions. Deflection radii of the two discharges analyzed in this study are indicated by the arrows.

5.9(a) & (b) shows the pellet velocity calculated from the fitted trajectory data along three directions in case of CW and CCW NBI beam, respectively. The positive velocities for V_{pol}, V_{tor} and V_{rad} represent the vertically up, counter clock wise toroidal and negative major radial directions of the plasma, respectively. In the time axis, 0 ms, corresponds to the fast camera image frame when the pellet just penetrates inside the LCFS. The stereo reconstructed pellet speed along the injection direction, V_{rad}, in its initial stage of motion is comparable to the injection speed of 420 ms^{-1} and 300 ms^{-1}, respectively for CW and CCW NBI injection. In the case of CCW NBI, the pellet penetrates into the plasma with almost constant speed, however a sharp decrease in pellet speed has been observed in CW NBI case. Normally the toroidal deflection speed up-to 400 ms^{-1} has been observed in both cases. The toroidal acceleration of the pellet in both cases is plotted

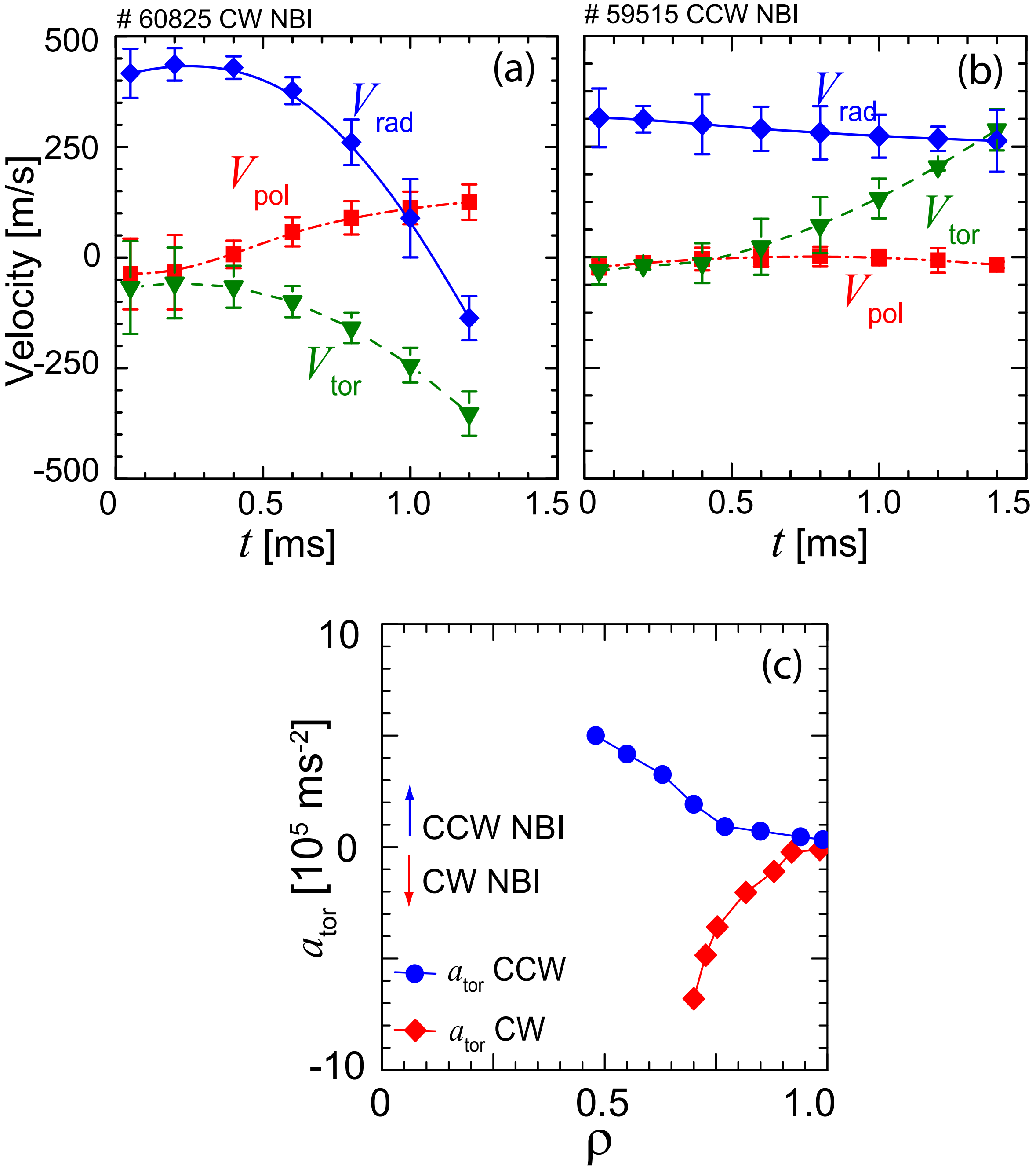

Figure 5.9 Pellet speed along vertical (V_{pol}), toroidal (V_{tor}) and negative major radial (V_{rad}) direction of the plasma for (a) CW and (b) CCW NBI injection.(c) Pellet toroidal acceleration in both NBI conditions, negative acceleration means CW direction.

in Fig. 5.9(c). The negative acceleration in the figure corresponds to the pellet deflection in the CW direction. The toroidal acceleration of the pellet starts at $\rho \approx 0.9$ in the CW NBI case and $\rho \approx 0.77$ in case of CCW NBI. The maximum accelerations achieved are 0.75 $\times 10^6$ ms^{-2} and 0.5 $\times 10^6$ ms^{-2} in the case of CW and CCW NBI conditions, respectively. The cause of the pellet toroidal deflection is discussed in the next section. For the time being it can be said that fast ions generated due to the neutral beam injection cause this deflection. Dependence of the maximum toroidal deflection speed ($V_{\rm tor}^{\rm max}$) on the plasma parameters such as temperature and density has also been observed. Figure 5.10 shows the variation of the maximum deflection speed with respect to the fast ion collision time ($\propto T_{\rm e}^{1.5}/n_{\rm e}$) at nearly equal NBI power of 3.5 - 3.7 MW . A power

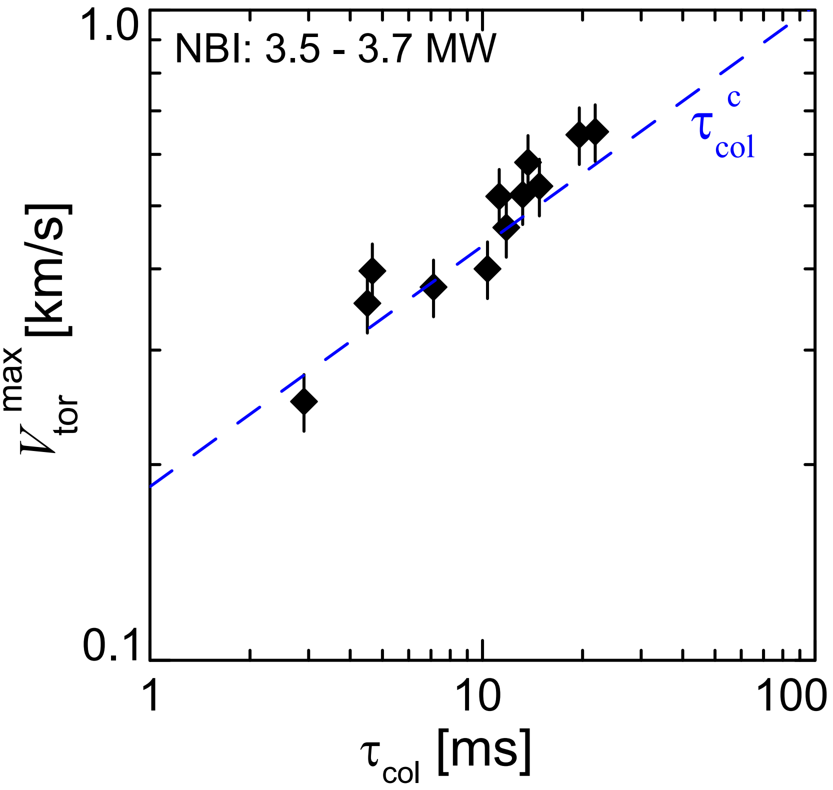

Figure 5.10 Variation of maximum toroidal deflection speed with fast ion collision time.

function fitting of the collision time is shown by the dashed line. Here, the constant c, is the fitting parameter. It is very clear from the figure that, the toroidal deflection speed increases with increase in collision time. In the case of high density plasmas with lesser collision time the attenuation of the fast ion density is significant and hence the contribution to the toroidal acceleration is lesser. Therefore the toroidal deflection reduces in low temperature and high density plasmas with higher collision frequency.

The stereo reconstructed pellet penetration depth into the plasma is estimated as $\approx$ 30 cm in the case of CW NB, whereas, it is $\approx$ 42 cm in case of CCW NB. The pellet penetration depth considering the constant pellet speed along the radial direction is compared with observations and is plotted in Fig. 5.11. Assuming a constant pellet speed inside the plasma, the maximum

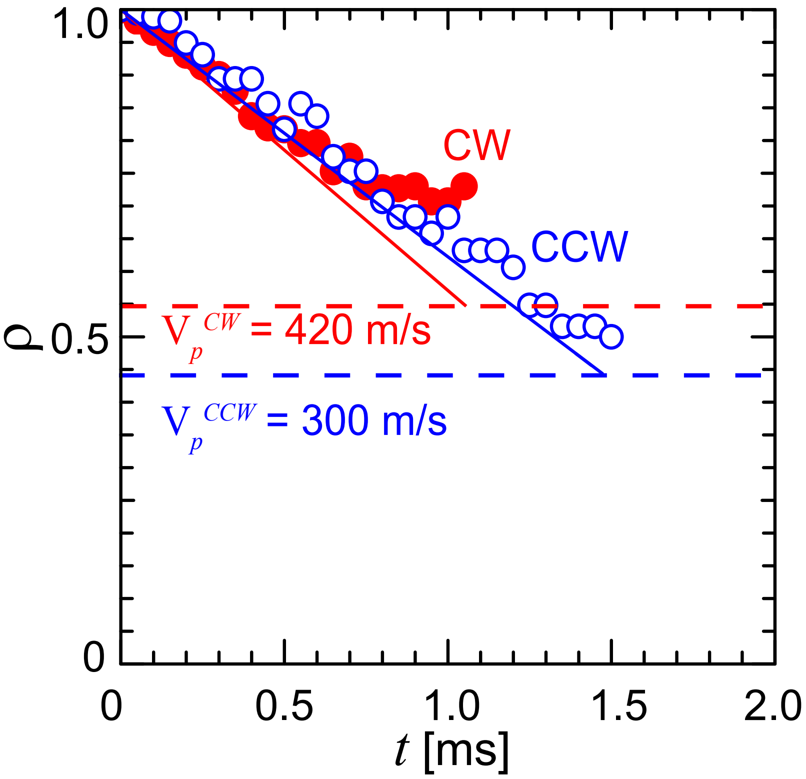

Figure 5.11 Time evolution of the pellet penetration in plasma under two NBI conditions.

achievable penetration radius and the calculated paths are represented by the dashed and solid lines, respectively. The solid and open circle shows the stereo reconstructed pellet position for CW and CCW NBI, respectively. In the case of the CW NBI, initially the pellet follows the presumed path, but just at the start of the toroidal deflection, penetration slows down and asymptotically reach ρ = 0.7 - 0.75. The observed penetration depth is ρ = 0.7, in comparison to 0.55 for a constant speed approximation. The achieved penetration depth (ρ= 0.49) for the CCW condition is closer to the constant speed penetration (ρ = 0.44). The radial electron temperature and deposited pellet density profile, obtained by using the Thomson scattering diagnostic in the case of CCW NBI injected pellet discharge is shown in the Fig. 5.12. The vertical dashed line in the figure represents

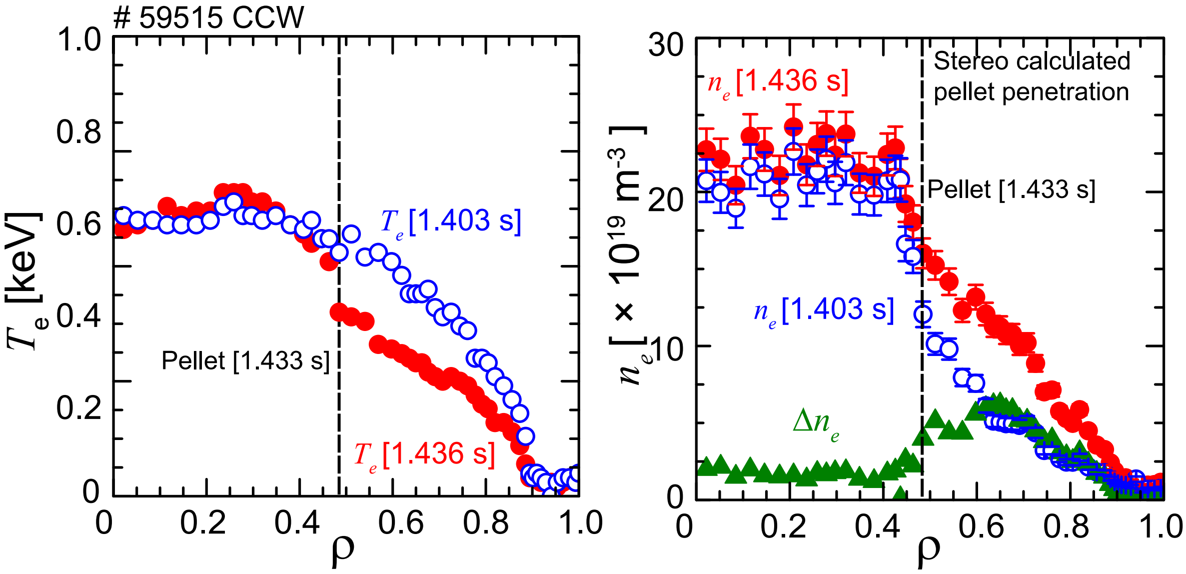

Figure 5.12 Radial profiles of T_e and n_e before and after the pellet injection in the case of CCW NBI plasma. Observed penetration depth is indicated by the vertical dashed line. The difference in two density profiles (Δn_e) shows the effective pellet mass deposition.

the observed pellet penetration depth obtained from stereoscopic measurement. It can be seen that the perturbation in the temperature and the density profile matches well with the measured penetration. The difference in the density profile, Δn_e, which indicates the effective deposition profile is shown by the solid triangles. The deposited particle inside the plasma calculated by integrating the Δn_e profile is 85 % of the injected pellet particles. Although the pellet penetrates to half of the plasma radius, the peak of the Δn_e profile lies just outside of ρ = 0.6. This indicates the outward redistribution of the deposited pellet mass as observed earlier in LHD [16] and is discussed in Chapter-6.

5.4 Discussions

The explanations regarding the key observations such as the cause of pellet deflection, difference in bending location and the poloidal deflection, from the observational points of view are presented in this section. Three dimensional motion of the pellet ablatant presented here is consistent with the two dimensional observations reported earlier for H_2 pellet in LHD [91]. Similar kinds of deflections are also reported in AUG tokamak for D_2 pellets [78] and in CHS for impurity pellets [94] in the presence of NBI heated plasmas. A review of the pellet trajectory deflection in tokomaks can be found in Ref. 73.

5.4.1 NBI Heating and Fast ion in LHD

It is known that the suprathermal electrons generated in tokomaks are responsible for the pellet deflection. In normal plasma conditions ($n_{e0} \approx$ 5-10 $\times$ 10^{19} m^{-3}) these suprathermal electrons are generated due to RF heating such as lower hybrid current drive. In LHD, the magnetic confinement field is generated by the helical coils and hence plasmas have current-less characteristics. Therefore, the possibility of any toroidal asymmetry in the electron distribution function cancels out. In this experiment, there is no RF heating and hence generation of the suprathermal electrons is limited. Since, NBI is the major source of the plasma heating in the pellet injected discharges; the fast ions generated by the neutral beam are significant. The effect of the fast ions on the pellet ablation can be observed by analyzing the ablation profile in the presence of NBI heated plasma in LHD. The pellet ablation profiles calculated in the presence of electrons and electrons plus fast ions by using the ABLATE [46] code in the frame work of NGS model [17] are plotted in Fig. 5.13. In

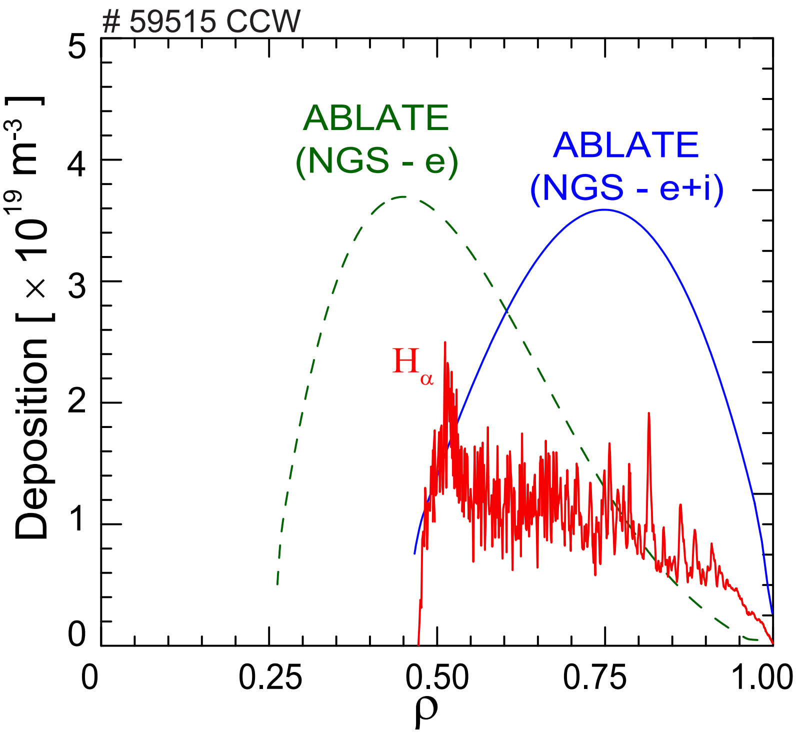

Figure 5.13 Pellet ablation profile calculated by using ABLATE code signifies the effect of fast ion on the pellet ablation process.

this figure, the pellet ablation profile is obtained for the CCW NBI, where the pellet travels with nearly constant speed. It can be observed from the figure that the ablation profile calculated by considering only the electrons predicts a much deeper penetration than the observed ablation profile deduced from the H_α time evolution. Including the effect of the fast ions, the density profile in the calculation gives a result comparable with the observation. A scaling of the pellet penetration depth considering the stored energy of the fast ions in the plasma center (W_{fo}) in the plasma is carried out by Hoshino in the LHD [77]. The stored energy of the fast ions is calculated as $W_{\mathrm{fo}} = P_{\mathrm{dep}} \times \tau_{\mathrm{slowdown},\,0}$, where, P_{dep} and $\tau_{\mathrm{slowdown},\,0}$ are the NBI power deposited and the slowing down time at the plasma center, respectively. It has been reported that, when the W_{fo} exceeds several percent of the total energy of the plasma, shallow penetration then the NGS model (electrons only) has been observed.

Therefore, the fast ions generated by the NBI heating contribute significantly to the ablation process in LHD. While considering the ablation due to the high energy particles, the effect from the particles gyro orbit should be taken into account. Considering the pitch angle (θ) of the gyro orbit of these energetic particles, direct heating of the pellet from its lateral surface cannot be ruled out [95]. A plot showing the interaction of the energetic ions with the ablating pellet is shown in Fig. 5.14. At this point two things to be considered for the pellet and fast ion interaction are

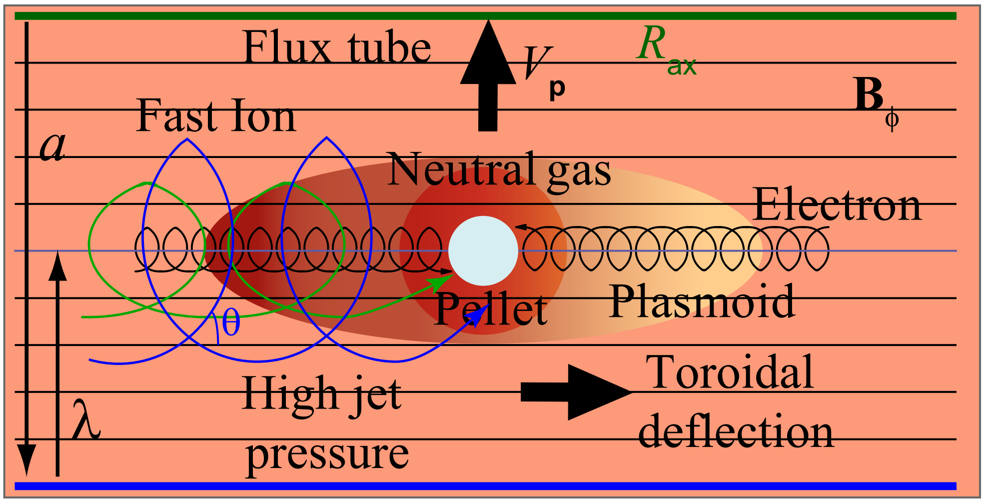

Figure 5.14 Formation of a rocket effect due to assymmetric ablation by the fast ions.

Larmor radius (ρ_l), and pitch angle of these energetic particles. From the figure, it can be observed that the fast ions having higher pitch angle (blue trajectory) have the higher probability to heat the pellet from its lateral side, compared to the pellet with lower pitch angle (green trajectory). The off-axis energetic particles with higher ρ_l and pitch angle have also the probability of direct heating of the pellet on its lateral side. For these particles, due to lesser shielding on lateral side, the effective surface area of the collection increases and hence the ablation can be spherically symmetric. Therefore the pitch angle distribution of the ion Larmor radius at different energy levels should be taken into account in presence of the energetic particles. In our experiment, since the applied NBI is in the tangential direction of the torus, the pitch angle of the passing fast ions are very less. Considering a nominal pitch angle, and beam energy of 180 keV, the maximum limit of ρ_l is $\approx$ 5.25 mm. With lesser pitch angle, the particles with smaller gyro radius have the higher probability of heating the pellet from fast ion side and subsequently, this leads to higher ablation and more pellet deflection. The off-axis particles with lower ρ_l cross the pellet in parallel direction. The particles with smaller pitch angle and higher ρ_l can also cross the pellet. Therefore in LHD, the probability of the lateral heating of the pellet surface is lesser in presence of fast ions generated due to the NBI heating.

5.4.2 Rocket Effect and Pellet Toroidal Deflection

The deflection of the pellet trajectory in the toroidal direction is modeled by using the rocket equation. From the linear momentum conservation, the one dimensional equation of motion can be written as [96],

$$m_\mathrm{p}(t)\frac{dV_{||}}{dt} = F_\mathrm{CW} - F_\mathrm{CCW}. \tag{5.2}$$

Here m_p is the mass of the pellet, $V_{||}$ is the toroidal deflection speed of the pellet, F_CW and F_CCW are defined as the thrust function on CW and CCW side of the pellet, respectively. The thrust function F is defined as,

$$F = \dot{G}|V_\mathrm{abl}| + p_\mathrm{abl}A_\perp. \tag{5.3}$$

Here, $\dot{G}$ is the local ablation rate of the pellet, V_abl is the ablatant velocity measured in the pellet reference frame, p_abl the ablatant pressure, and $A_\perp$ is the pellet surface area normal to the magnetic field. The local ablation rate $\dot{G} = |V_\mathrm{abl}|\rho_a A_\perp$ and $\dot{G}_\mathrm{CW} + \dot{G}_\mathrm{CCW} = \dot{m}_\mathrm{p}$, where $\dot{m}_\mathrm{p}$ is the total mass ablation rate of the pellet and ρ_a is the density of the ablatant. Assuming equal pressure on both sides of the pellet, and combining Eqn. 5.2 and Eqn. 5.3,

$$m_\mathrm{p}(t)\frac{dV_{||}}{dt} = F_\mathrm{CW} - F_\mathrm{CCW} = [\dot{G}V_\mathrm{abl}]_\mathrm{CW} - [\dot{G}V_{abl}]_\mathrm{CCW}. \tag{5.4}$$

Dividing Eqn. 5.4 by the mass of the cloud particles,

$$N_\mathrm{p}(t)\frac{dV_{||}}{dt} = F_\mathrm{CW} - F_\mathrm{CCW} = [\dot{N}_\mathrm{p}^\mathrm{CW}(t)V_\mathrm{abl}] - [\dot{N}_\mathrm{p}^\mathrm{CCW}(t)V_\mathrm{abl}], \tag{5.5}$$

where, N_p is the total particle content of the ablation cloud surrounding the pellet. The ablatant velocity, $V_\mathrm{abl} = \mathrm{f}(\gamma T_\mathrm{N}/m_\mathrm{p})$. Therefore the thrust function in the Eqn. 5.5 depends on the pressure inside the neutral cloud. Assuming the uniform ablation due to electrons on both sides of the pellet, the toroidal acceleration (a_ϕ) due to the ablatant pressure on the fast ions side can be written as,

$$a_\phi = P_\mathrm{f}\pi r_\mathrm{p}^2/m_\mathrm{p}. \tag{5.6}$$

Where, $P_\mathrm{f} = n_\mathrm{N}kT_\mathrm{N}$ is the jet pressure and T_N is the neutral cloud temperature. In a simplistic assumption, assuming the constant ablation rate of the pellet, the neutral jet density is given by the relation

$$n_\mathrm{N} = N^\mathrm{ab}/(V_\mathrm{N}\Delta t\pi r_\mathrm{p}^2). \tag{5.7}$$

Here N^ab is the ablation rate in the presence of fast ions; V_N is the neutral cloud expansion velocity, $\Delta t(\approx 1.2\text{ ms})$ is the total ablation time and r_p is the radius of the pellet. The cloud expansion velocity can be calculated as

$$V_\mathrm{N} = \sqrt{\gamma kT_\mathrm{N}/m_{\mathrm{H}_2}}, \tag{5.8}$$

where, γ is ratio of the specific heat constant and m_{H_2} is the molecular mass of H_2.

Using the NGS model the pellet ablation scaling laws in MKS unit can be written as [17],

$$\dot{r}_\mathrm{p} = 7.98 \times 10^{-14} r_\mathrm{p}^{-2/3} n_\mathrm{e0}^{1/3} T_\mathrm{e0}^{1.64}\ \mathrm{m/sec} \tag{5.9}$$

$$n_\mathrm{N} = 4.4 \times 10^{16} r_\mathrm{p}^{-1} T_\mathrm{e0}^{1.68}\ \mathrm{m}^{-3} \tag{5.10}$$

$$T_\mathrm{N} = 2.41 \times 10^{-11} r_\mathrm{p}^{2/3} n_\mathrm{e0}^{2/3} T_\mathrm{e0}^{-0.14}\ \mathrm{eV} \tag{5.11}$$

Here, n_e0 and T_e0 are the plasma core electron density and temperature, respectively. Therefore by using the scaling for the temperature and density, the scaling law for the neutral pressure cloud can be written as,

$$p_\mathrm{N} = 1.7 \times 10^{-13} r_\mathrm{p}^{-1/3} n_\mathrm{e0}^{2/3} T_\mathrm{e0}^{1.54}\ \mathrm{N/m}^2 \tag{5.12}$$

Where, n_N, T_N and p_N represent the neutral cloud density, temperature and pressure at the sonic radius, respectively. In sonic approximation, it is considered that the flow beginning at the pellet surface is subsonic, and is accelerated continuously up to a sonic radius, at which point the effects of heating and area increase exactly balance and flow becomes supersonic. From the pressure equation it can be seen that the pressure inside the cloud is as strong function of the electron temperature. In the NGS model it has been assumed that the heat flux is from mono-energetic electrons of average energy $E = 2kT_{e0}$. While in presence of the energetic particles, accounting the Maxwellian distribution and shielding due to the cold plasma outside the neutral gas, a new model has been formulated as neutral gas and plasma shielding (NGPS) model [43]. It has been shown in the Ref. 97 that the ablation rate in the NGPS model differs from the NGS model by a factor two only, but the NGS model highly overestimates the temperature of the neutral gas cloud. Therefore, for the cloud temperature a more accurate scaling based on the frame work of the NGPS model is proposed in the limit of $\beta \ll 1$, where β is the fraction of background electron flux that reaches the neutral gas cloud. Accordingly, the scaling laws for the neutral gas density and the cloud temperature is given by [97],

$$n_{\mathrm{N}} = 3.84 \times 10^{24} \alpha^4 Z(Z+1)^{-1} r_{\mathrm{p}}^{-1} T_{\mathrm{e0}}^{2}\ [\mathrm{m}^{-3}]. \tag{5.13}$$

$$T_{\mathrm{N}} = 0.32\alpha^{-4}(Z(Z+1) r_{\mathrm{p}} n_{\mathrm{e0}} T_{\mathrm{e0}}^{-1/2} \mu_{\mathrm{I}}^{1/2} T_{\mathrm{p}}^{1/2} E_{\mathrm{i}}^{-1}\ [\mathrm{eV}], \tag{5.14}$$

Here, $\mu_I = 2$, Z = 1, α = 3-5 (considering Maxwellian distribution), and T_{p} is the plasma cloud temperature surrounding the neutral cloud. The neutral cloud temperature (T_{N}) predicted by the NGS model is of the order of 0.1 eV, however, using the NGPS model, the cloud temperature of one order less than the former case has been obtained. The experimental conditions and the constants used in the equation (5.14) are $n_{\mathrm{e0}} = 10 \times 10^{19}$ m^{-3}, $T_{\mathrm{e0}} = 0.6$ keV, α = 3, T_{p} = 1 eV, E_{i} = 13.6 eV, and the pellet radius r_{p} = 1.25 mm. Using these values, the neutral cloud temperature T_{N}, and the velocity V_{N} (Eqn. 5.8), calculated are $\approx$ 0.02 eV and 2.6 $\times 10^3$ ms^{-1}, respectively. Considering total ablation of the pellet (N_{ab} = Total particle content of the pellet), and using the equation (5.7), the jet density calculated is 4.8 $\times 10^{25}$ m^{-3}. The jet density obtained here is comparable to the density calculated (5.25 $\times 10^{25}$ m^{-3}) from the scaling laws in Eqn. 5.13. Using these values calculated here, and with the help of the Eqn. 5.6, the acceleration estimated in the case of the CW

NBI is $\approx 1.2 \times 10^6$ ms^{-2}. The calculated acceleration is comparable to the observed acceleration of 0.75×10^6 ms^{-2}. It has been demonstrated in the CW H$_\alpha$ signal that the direct impact of the neutral beam on the pellet is very weak, therefore the observed trajectory deflection is only due to the rocket effect generated by the fast ions. The acceleration observed in the case of CW NBI (3.7 MW) 0.75×10^6 ms^{-2} is higher than the acceleration of 0.5×10^6 ms^{-2} in case of CCW NBI (2.7 MW). The difference in the acceleration in both cases can be explained from the fast ion density profile. The fast ion density profile calculated with the help of a simplified model presented by Rome [98] is shown in Fig 5.15. It can be observed from the figure that the fast ion density is higher in case of the CW NBI than the CCW NBI and hence higher is the acceleration. The rocket effect discussed here can also be used as a potential candidate to explain the speed loss along the radial direction (in CW NBI case) as reported in [99]. In the case of the outboard injected

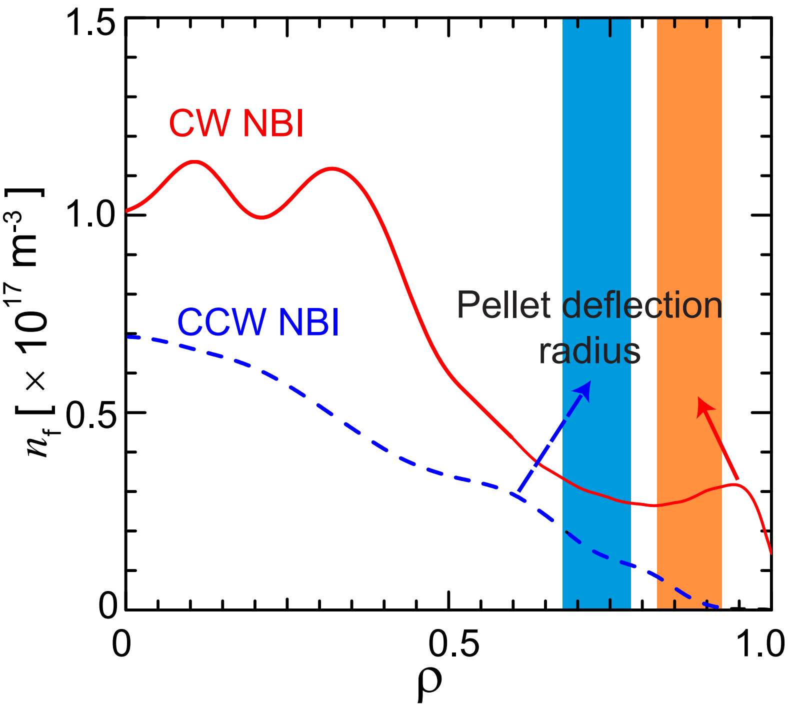

Figure 5.15 Calculated fast ion density profiles along the pellet trajectory. Shaded area corresponds to the bending radius in the cases of CW and CCW NBI conditions.

pellet, expulsion of pellet particles to the vessel outward direction has been observed in LHD. The expelled particles can cool the outer flux surface and hence the low field side of the pellet has more shielding and less ablation pressure than the high field side. Therefore, there is a rocket force opposite to the pellet injection direction and the pellet experiences a reduction in speed. Contrary to this, any speed loss in the case of CCW NBI has not been observed, although it is an LFS injection. Therefore, more systematic observations and favorable explanations are needed in order to have a clear understanding in this regard.

The variation in pellet bending location can also be explained by the difference in the fast ion profile at the plasma edge. The shaded area in Fig. 5.15 indicates the deflection radius, where on average the pellet deflection starts in both cases. The fast ion density in the case of CW injection is significantly higher at the plasma edge in comparison to the other case and hence deflection of the pellet starts at the outer plasma layer. It should be noted here that, the deflection depends on the ablation characteristics of the pellet, which are determined by local factors and mainly by the particle heat flux onto the pellet surface.

5.4.3 Field Geometry and Pellet Vertical deflection

In the present study it can be assumed that, two factors may contribute to the pellet motion inside the plasma: (1) the ablation process, and (2) the geometry of the field lines. An advanced model describing the pellet ablation process in the presence of high energy particles has been reported in Ref. 95. The importance of additional shielding by the ionized cloud in the presence of high energy particles has been described in that article. Therefore a detailed modeling is necessary in-order to have a better knowledge of the pellet plasma interaction in LHD. However in a simplistic assumption, the effect of the geometry of the field lines cannot be neglected due to the following reasons. In the case of CW NBI, the pellet deflects in the clock-wise direction to a vertically elongated cross section, where the plasma has a squeezed section in the horizontal plane and an elongated section in the vertical plane. Also there is a vertical deflection of the pellet in this case. Therefore, the pellet resides on the flux surfaces which do not vary significantly. However, in the other NBI case deflection of the pellet occurs more inside the plasma to an expanding (horizontally elongated) cross section in the mid plane, where the field lines are quite flat and hence the penetration has not been significantly affected by the geometry of the field lines. Therefore, the observed pellet penetration is significantly less in comparison to the constant speed approximation in the case of CW NBI. The vertical deflection of the pellet is explained by the structure of the magnetic field lines. The vertical deflection of the pellet in CW and CCW (small deflections wherever observed) NBI cases are in the upward and downward directions of the plasma, respectively, which is in close agreement with the structure of the field lines. Experimentally observed vertical deflections (absolute value) for a number of pellets in both cases are plotted (solid symbols) against the deflection radius in Fig. 5.16. Poloidal shift of the field lines (absolute value) within the pellet deflection region (a few degrees toroidally) at each plasma radius for CW and CCW directions are shown by the dashed lines. It can be inferred from the figure that the poloidal shift of the field lines is more in the outer layer of the plasma due to the high pitch angle of the field lines and it gradually decreases towards the center of the plasma. Similar is the case for the vertical deflection obtained from the experiment. In the case of CW NBI as the pellet deflects toroidally in the outer layer of the plasma, the vertical deflection is higher in comparison to the CCW NBI, where the toroidal deflection of the pellet starts deeper inside. Therefore it can be concluded that in addition to the ablation process, the geometry of the field lines can also contribute significantly to the pellet dynamics in LHD.

5.5 Summary

The stereoscopic diagnostic has been applied successfully to measure the three dimensional motion of an ablating pellet in the presence of the NBI heated plasma in LHD. The expansion of the pellet ablation cloud along the magnetic field direction has also been confirmed. Toroidal as well as the poloidal deflection of the pellet trajectory with respect to the tangential NBI (CW or CCW) has been observed. The observed toroidal deflection is similar in both cases, however an asymmetry

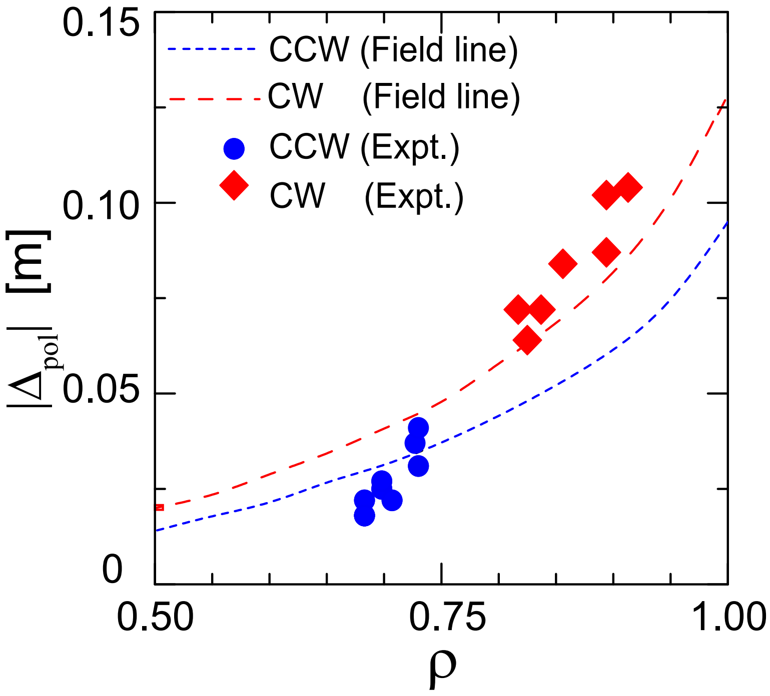

Figure 5.16 Comparison of the observed vertical deflection (filled symbols) and poloidal shift (absolute value) of the field lines, calculated from the field line tracing (dashed lines) within the pellet life time at different pellet deflection radii.

in the poloidal deflections has been observed in the case of CCW NBI. Predominance of fast ions generated by the NBI on the pellet ablation process in LHD plasmas has been demonstrated by using the NGS model with fast ions. Deflection of the pellet trajectory in the presence of neutral beam is explained by the formation of the rocket effect due to one-sided ablation of the pellet surface by the fast ions. The observed acceleration along the toroidal direction is of the order 10^6 ms^{-2} and is in close agreement with the calculated acceleration from a simple rocket effect model. The fast ion density profile helps us to explain the variation in pellet deflection radius in two different NBI conditions. The difference in the vertical deflection of the pellet is believed to be due to the pitch of the helical $\boldsymbol{B}$ field lines.

The reduction of the total pellet speed, which is mainly contributed by the speed loss in the penetration direction, is still unclear as it has been only observed in the case of CW-NBI. Although the simplistic assumptions presented in this study are able to explain the pellet deflections, a more detailed theoretical study considering the interaction between the pellet and the fast ions is necessary in order to address the complete dynamics in the presence of the NBI heated plasmas in LHD.

Chapter 6

Pellet injection studies from multiple injection locations

6.1 Introduction

Pellet injection has been proven as an inexpensive method for plasma fueling. Using the pellet injection, improved confinement properties and the fueling efficiency (ε_f) have been demonstrated in many fusion devices including tokomak and helical system [10, 13, 14, 16], and is also planned for ITER [18, 100]. One of the primary requirements for the good ε_f is the deep penetration of the pellet into the plasma. Apart from the dependence of the pellet penetration on local plasma conditions, and the history of the injection parameters, it is also affected by the non-ideality in trajectory due to the unbalanced ablation by the energetic particles in the plasma [86]. An anomalous mass deposition profile in comparison to the pellet penetration radius in the case of the Low field side (LFS) injection has been reported earlier on JET and TFTR [40]. This anomaly suggests an outward redistribution of the ablated pellet mass and subsequently, deposition of the mass at outer layer of the plasma. This redistribution is supposed to be due to the $\boldsymbol{E} \times \boldsymbol{B}$ drift of the plasmoid in its self consistent $\boldsymbol{E}$, arises from $\boldsymbol{B} \times \nabla B$ drift of ions and electrons in the vertical direction [101]. Considering this fact, an improved fueling efficiency has been first demonstrated in AUG-tokamak [102] for the high field side (HFS) pellet injection studies. Using the fiber arrays diagnostic, pellet plasmoid drift towards the LFS of the torus has been directly observed in RFX for LFS [103] and in ASDEX-Upgrade (AUG) tokamak for LFS and HFS pellet injection [104]. These results suggest that, owing to the ∇B drift of the ablated mass, a better fueling efficiency can be obtained for the HFS injection location. This drift can also help more penetration for HFS injection indirectly by cooling the plasma surface in front of the pellet, which leads to a slower ablation rate and longer life time of the pellet [105]. Since, there is a strong dependence of the pellet penetration on electron temperature over its injection speed, fueling of the reactor scale plasmas will be a great challenge for the conventional LFS injection with higher velocity. Therefore consideration of the fueling location optimization is important rather than to maximize the pellet injection velocity.

In LHD, the magnetic confinement field is generated by the external helical coils. Therefore, one cannot simplify the magnetic field strength distribution like, $B \propto 1/R$, as in axis symmetric tokamak field. A complementary study, focusing on the differences of the magnetic field configuration between the helical device and the tokamak is one of the approaches to understand the effect of the pellet plasmoid drift on the fueling efficiency. In an attempt to explore the ∇B induced HFS fueling characteristics in LHD, pellet injection experiments have been performed for the outboard coil side injection [91]. In that observation, a correspondence between the pellet ablation and mass deposition radius had been reported. Due to the lack of local density measurements (Thomson scattering profile), it is still premature to conclude this observation quantitatively, from the view point of the fueling efficiency. In-order to explore the possibility of enhanced ε_{f} by considering the ∇B induced drift, pellet injection experiments have been carried out from different injection locations in LHD.

6.2 Experimental setup

The pellet injection experiments were performed in LHD for the plasma configuration namely the major radius (R_{ax}), averaged minor radius (a_{ave}), plasma volume (V_{plasma}), and the magnetic field strength on the axis of 3.75 m, 0.6 m, 26 m^3 and 2.64 T, respectively. In the pellet injected discharges, the plasma heating is mainly performed by the tangentially operated negative ion based neutral beam injectors (NBI-1, NBI-2 and NBI-3) of total power up-to 15 MW [26]. The maximum energy of each neutral beam is of 180 keV. The procedure followed for deciding an injection position is detailed in Chapter-2. The injection position chosen for the HFS is an oblique angle inboard side launching, from a horizontally elongated section to the proximity of the helical coil [49]. By using the newly developed punch mechanism based low-speed pellet injector [106], a pellet is injected from the LFS (horizontally elongated outboard) and the HFS location. Since a pellet is transferred to the respective injection locations through the bended guide tube, the injection speed is limited to, $V_{\text{p}} \approx 275\ \text{ms}^{-1}$, in-order to be delivered intact. In addition to the low-speed pellet, high-speed pellet injection ($V_{\text{p}} \approx 1100\ \text{ms}^{-1}$) by using the multi barrel pipe gun type pellet injector [65] is also carried out from the low field side of the torus. The typical size of an injected pellet at the injector exit is 3 mmℓ × 3 mmφ, and it contains 10^{21} atoms.

A PIN photodiode with an H_α filter (centre wavelength 656.5 nm/half band width 9.2 nm) installed at the outer port of the vacuum vessel measures the pellet ablation light at a time resolution of 1 μs. A stereoscopic observation system [80] is employed to measure the pellet ablation dynamics inside the plasma. A schematic of top view of the LHD mid-plane with the pellet injection directions and the stereoscopic camera positions (Lens-1 and Lens-2) is shown in Fig. 6.1(a). The directions of the CW and CCW NBI beam, and the position of the helical coils are also indicated in the figure. The entry point of the pellet into the vacuum vessel in the poloidal cross-section, for outboard LFS and inboard HFS injection is shown in Fig. 6.1(b). Directions of the ∇B are indicated by the solid arrow. A pair of stereo image is obtained by using a single fast camera, and coherent bundled fiber having bifurcation at the imaging end. The spatial and temporal resolution of the

(a) Top view of Mid-plane

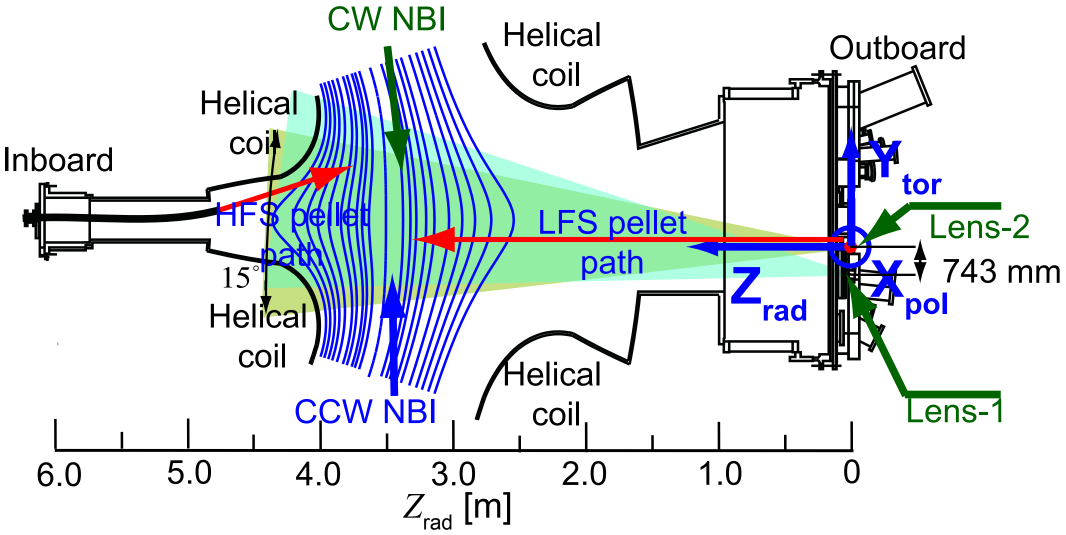

(b) Vertical View

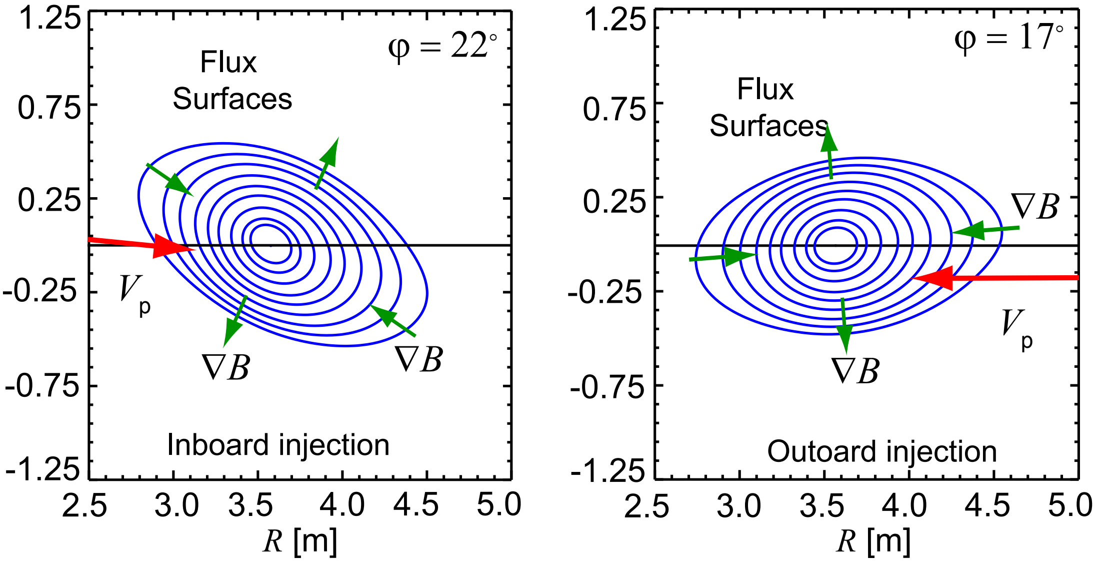

Figure 6.1 Schematic of the pellet injection cross-section for LFS and HFS injection showing, (a) top view of mid-plane and (b) vertical view. Origin of the pellet position (X_{pol}, Y_{tor}, Z_{rad}) inside the vessel is taken at the Lens-2 camera port. The shaded portions (in top figure) represent the viewing area of each camera.

fast camera is (512 × 232) pixels and 20μs, respectively. The pellet positions inside the plasma is measured with respect to a center of reference situated at the right camera position (Lens-2). The coordinate axes X_{pol} and Y_{tor} in this reference frame represent the vertical and toroidal direction of the plasma, respectively. The Z_{rad}-coordinate indicated in meters is taken along the negative major radial direction of the vessel. The shaded regions on the figure represent the viewing area of the two camera. The calibration error of this observation system is ±5 mm in X_{pol} and Y_{tor} directions, and ±17 mm along the pellet injection direction (Z_{rad}). Radial profiles of the plasma electron temperature (T_{e}) and density (n_{e}) are measured by using the 200 point Thomson scattering diagnostic installed at the horizontally elongated section of the plasma mid-plane [38] at 20 ms intervals. The high resolution chord integrated density data obtained from the FIR interferometer signal installed at a vertically elongated section 180° from the pellet injection port, are used for the mass redistribution analysis [35].

6.3 Results and Discussion

In order to investigate the pellet ablation and mass deposition behavior in LHD, pellets were injected to similar plasma configurations from the LFS and the presumed HFS of the torus. The range of plasma parameters (n_{eo} and T_{eo}) analyzed in this study are plotted in the Fig. 6.2. In this figure, a circle and a diamond represents the speed of the injected pellet in the range of 0.17-0.27 kms^{-1} and 1.0-1.2 kms^{-1}, respectively. Within these data range, two typical discharges, which had the good diagnostic data are analyzed. In the case of the LFS injection, the plasma parameters are: (#104254) n_{eo} = 1.5 $\times 10^{19}$ m^{-3}, T_{eo} = 2.26 keV, and $P_{\mathrm{NBI}}^{\mathrm{depo}}$ = 0.8 MW (CCW). Penetration characteristic for a high-speed pellet from this injection location is also studied. Similarly, the parameters in the case of the alternative injection are (#104237) 1.4 $\times 10^{19}$ m^{-3}, 2.36 keV, and 2.1 MW/1.6 MW (CCW/CW), respectively. The pellet speed in the case of the LFS and the HFS launching are, 220 and 237 ms^{-1}, respectively.

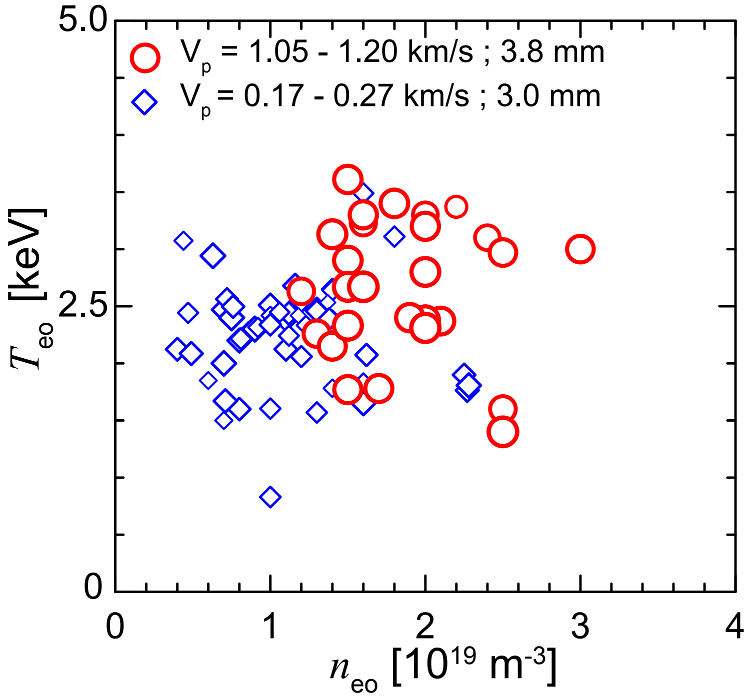

Figure 6.2 The range of the plasma parameters covered in this experiment. The size of a symbol represents the pellet injection speed in the corresponding speed range.

6.3.1 Low field side pellet injection

In LHD, it has been observed that the pellet deflects three-dimensionally in the presence of one sided tangential NBI [106]. Concerning with this, reduction of the pellet speed has been observed for the CW-NBI; while for the CCW and balanced NBI, the pellet penetrates with the constant speed. Therefore, for the outboard low field side pellet penetration and mass deposition analysis, only the pellets of both sided or CCW dominated NBI are considered.

In the case of the outboard LFS pellet injection, pellets of two different size (3.0 and 3.8 mm) and speed (250 and 1100 ms^{-1}, respectively) are injected. A typical waveform of the pellet injected discharge for the LFS location is shown in Fig. 6.3. With the pellet injection, a simultaneous increase in the line averaged $\bar{n}_e$ and the plasma stored energy can be observed from the figure. The penetration depth of the pellets has been estimated from the duration of the H$_\alpha$ signal assuming

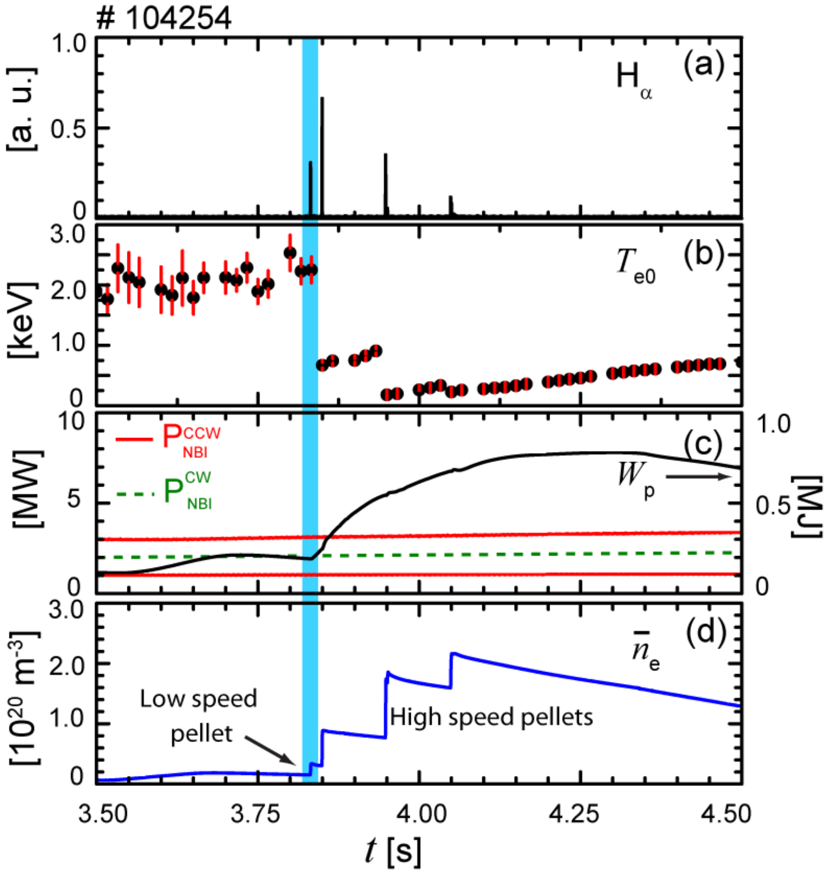

Figure 6.3 Waveform of a typical pellet injected discharge for LFS injection showing: (a) H$_\alpha$ ablation light, (b) central electron temperature T_{e0}, (c) plasma stored energy and the port through NBI power, and (d) line averaged electron density $\bar{n}_e$.

a constant radial velocity. The validity of the NGS scaling law for different plasma conditions in LHD is examined by comparing the experimentally observed pellet penetration with the calculated penetration. Since, a pellet is injected into the plasma with an oblique angle in the case of the inboard HFS injection, only the pellets injected from the LFS is considered in this comparison. Assuming the linear profile for the electron temperature and density, the NGS (electron only) scaling law for the pellet penetration depth is given by [107],

$$\frac{\lambda}{a} = 0.079 T_{eo}^{-5/9} n_{eo}^{-1/9} m_p^{5/27} V_p^{1/3}. \tag{6.1}$$

Where, λ/a is the normalized penetration depth with $\lambda/a = 1$ corresponds to the pellet penetration to the axis of the plasma. Here, T_e is in keV, n_e is in 10^{20} m^{-3}, m_p is the number of Hydrogen atoms per pellet in 10^{20} and V_p is the speed of the pellet in ms^{-1}. Figure 6.4 shows a comparison between the experimentally observed and the calculated penetration depth by using the above scaling law. A linear fitting of the experimental points is shown by the dashed line. It can be observed from

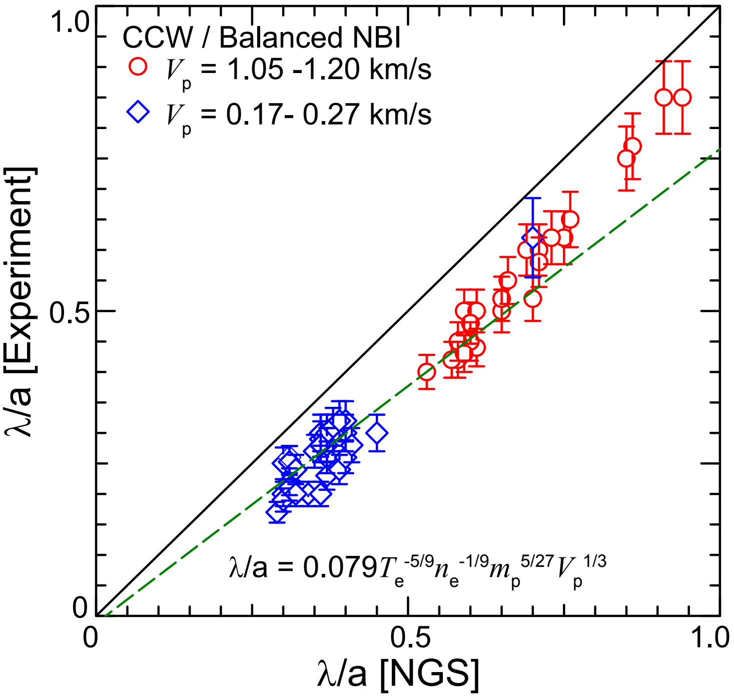

Figure 6.4 Experimental penetration depth plotted against the predicted penetration depth considering the NGS model (electron ablation only).

the figure that there is a clear discrepancy between the measured and the calculated penetration depth. However, the trends in measured λ/a is similar to that of the scaling. This discrepancy is due to the increase in ablation by the fast ions and shortening of the pellet life time. Since, the original NGS scaling does not take into account the ablation due to the fast ions, shortening of the experimental penetration depth from the scaling is obvious. Another point to be noted from the figure is that, the experimentally observed penetration is systematically higher than the fitted data for the pellets penetrate more than 3/4 of the plasma radius. The reason can be explained as follows. The pellet penetration depth is a strong function of the background temperature. Commonly, higher penetration of the pellet is due to the lower background temperature. Lower temperature plasmas are accompanied with higher n_{e}. Extending the discussion for the NBI generated fast ion effect on the pellet (previous chapter), it can be said that, at higher densities the effect of the fast ions is reduced and hence the penetration depth increases. A new penetration depth scaling based on the fast ions stored energy at the plasma center as one of the factor is put forward by Hoshino *et al.* [90]. In that study it has been found that, when the ratio of the fast ion stored energy to that of the plasma stored energy, (W_{f0} / W_{dia}) < 5 %, the trend agrees with the NGS scaling. However, when this ratio exceeds 5 %, a large difference from the predicted penetration has been observed in the case of deeper penetration of the pellet. Therefore, the fast ions generated due to the NBI heating significantly affects the pellet ablation process and hence the pellet penetration inside the plasma. Variation of the pellet penetration depth with the T_{e0}, in the case of the high speed and the low speed pellets is shown in Fig. 6.5. The modified scaling law considering the NGS parameters used for the LHD data's has a temperature dependence of $T_{\mathrm{e}}^{-0.68}$, which is more or less similar to that of the original NGS scaling dependence of $T_{\mathrm{e}}^{-5/9}$. A solid line corresponding to the $T_{\mathrm{e}}^{-0.68}$ dependence is fitted to the experimental points, and it qualitatively validates the NGS penetration scaling.

In the case of LFS injected pellet (#104254) with CCW NBI, the penetration depth estimated from the constant speed (V_{p} = 220 ms^{-1}) approximation for 1.14 ms ablation time is 25 cm. Using the stereoscopic diagnostic, the pellet penetration depth measured for this discharge is $\approx$ 23 cm, which is in close agreement with the expected penetration depth. As like observations presented in the previous chapter for CCW NBI case, deflection of the pellet trajectory has been observed at the final stage of its trajectory. However, due to long spread plasmoid and the strong intensity of the ablation light on the image frames, it has not been possible to obtain the pellet position more accurately at the final stage of its motion. The pellet speed in its injection direction and in the

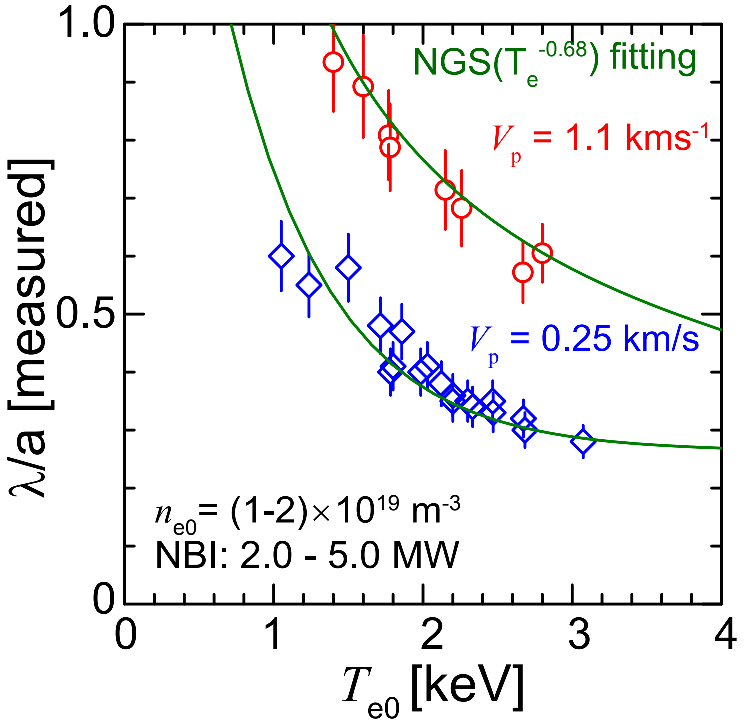

Figure 6.5 Temperature dependence of the penetration depth in the density range (1-2) $\times 10^{19}$ m^{-3} in case of low speed and high speed pellets. The solid line indicates the $T_e^{-0.68}$ fitting of the data's.

vertical direction is found to be constant. The pellet deflection speed up-to 600 ms^{-1} has been found in the toroidal direction.

Pellet fueling efficiency depends on the radial profile of the particle deposition. The particle deposition profile measured from the difference of the Thomson scattering n_e profile before and 3 ms after the pellet injection is plotted in Fig. 6.6. The pellet ablation light (H$_\alpha$) mapped onto the radial direction considering the constant pellet speed is also shown in the figure. The ablation light signal indicates that the pellet penetrates to $\rho \approx 0.7$, and the peak of the ablation light lies at $\rho \approx 0.83$. Drop in the temperature profile at different plasma radii after the pellet injection also coincides with the penetration depth. Therefore a mass deposition profile similar to that of the ablation profile is expected. In contrast, it can be observed that the mass deposition profile lies at

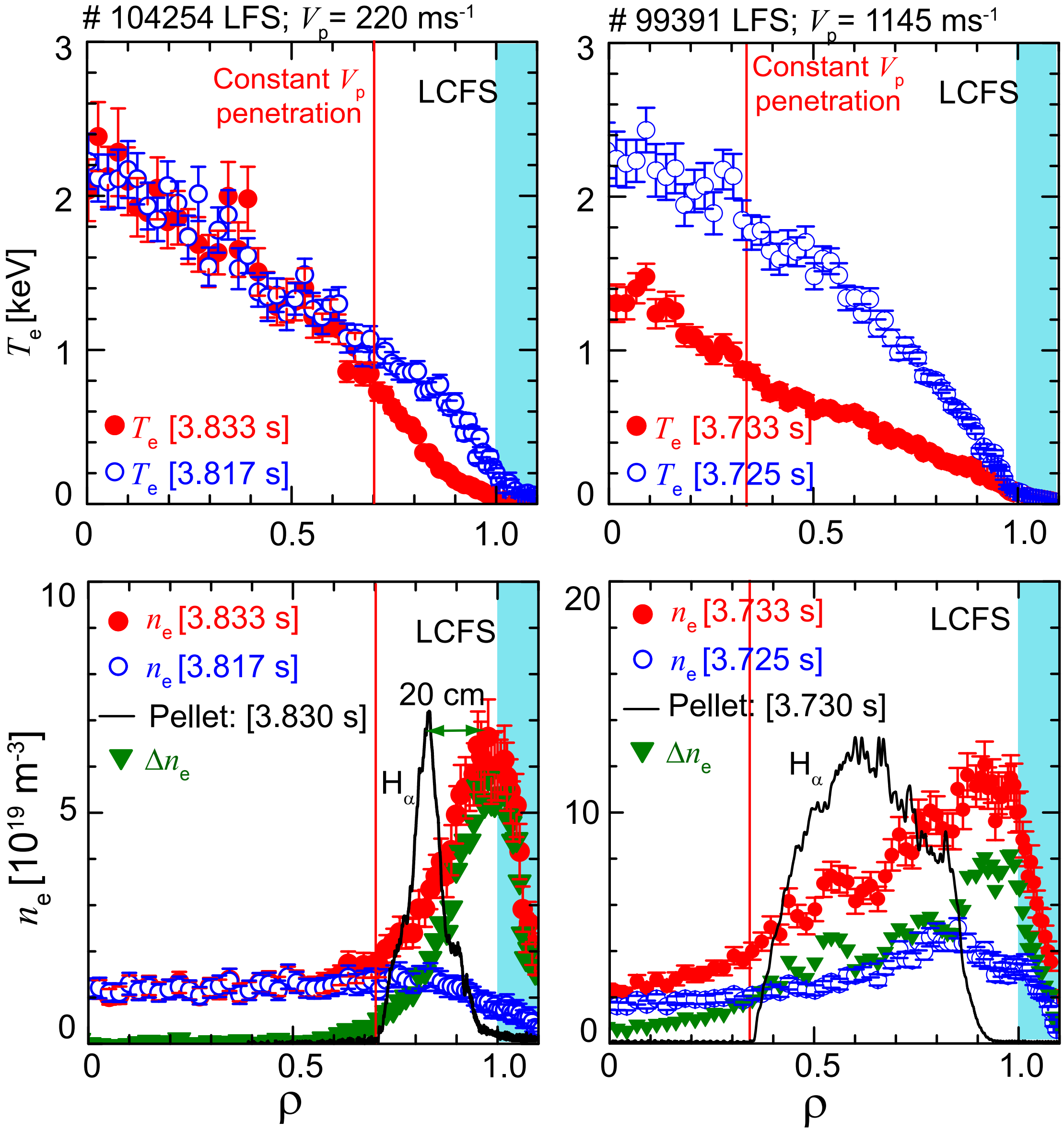

Figure 6.6 Radial profiles of the T_e and n_e obtained from the Thomson scattering diagnostic in the case of (left) low speed (# 104254), and (right) high speed (# 99391) injected pellets. The particle deposition profile, which is the difference in density profile after and before the pellet injection, is shown by the inverted solid triangles. H_α ablation light indicating the pellet penetration depth is also shown.

the last closed flux surface (LCFS). The difference between these two peaks is 15-20 cm. A case for a high speed pellet injection with speed V_{p} = 1145 ms^{-1} and size 3.8 mm is shown in the right side of the Fig. 6.6. Due to higher speed and mass, the pellet penetrates to $\rho = 0.35$. However, similar to the observation in low speed case, the peak of the deposition profile lies at the edge of the plasma. This fact suggests that the ablation of the pellet is not the end of the process, and there exists some outward force that drives out the ablated mass towards the edge of the plasma. We will discuss this issue latter; for the time being it can be said that, this is similar to the ∇B induced drift of the pellet plasmoid in tokomaks.

6.3.2 Inboard high field side pellet injection

Hydrogen pellet of size, 3mm, and speed, < 260 ms^{-1} has been injected from the presumed HFS of the LHD. Waveform of a typical pellet injected discharge is shown in Fig 6.7. Increase in W_{p} and $\bar{n}_{\mathrm{e0}}$, just after the pellet injection can be observed from the figure. Similar to that of the outboard injection, it has been observed that the pellet has three-dimensional trajectory, in presence of the asymmetric NBI heating. In fact, the pellet always deflects in CW-toroidal direction in presence of both type of NB heating. The cause is discussed latter in this section. The reconstructed pellet trajectory of a maximum toroidally deflected pellet obtained from the stereoscopic diagnostics is shown in Fig. 6.8 (a) & (b). The parameters in this discharge are: n_{eo} = 0.63 $\times 10^{19}$ m^{-3}, T_{eo} = 2.36 keV, and $P_{\mathrm{NBI}}^{\mathrm{depo}}$ = 0.82 MW (CCW) and 0.66 MW (CW). The error bars are calculated by considering the width of the ablation light intensity. Since, LHD plasma is surrounded by a thick ergodic layer, and especially ergodicity is significant in the inboard side, ablation of the pellet well before the LCFS is expected. In addition, oblique injection of the pellet makes the situation more complicated. In concern to this, the pellet ablation light in the camera frame well before the LCFS has been observed. It can be observed from the figure that the pellet initially follows the injection path but just after crossing the LCFS, the pellet deflects three dimensionally in CW toroidal and vertically downward direction. Where as the toroidal deflection depends upon the fast

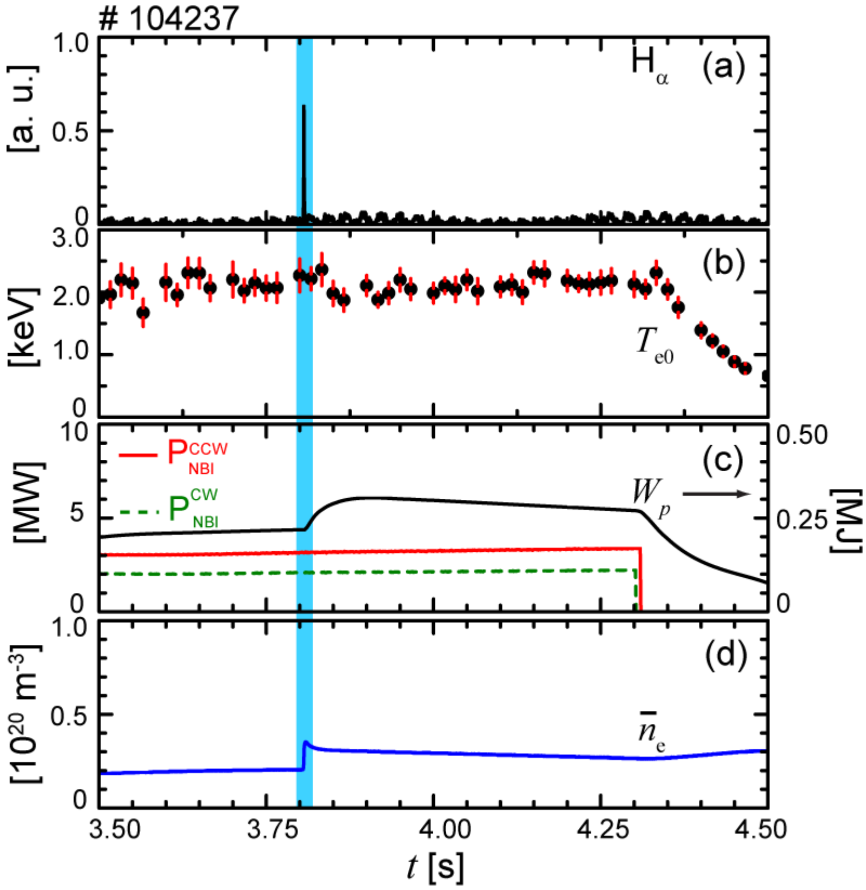

Figure 6.7 Waveform of a typical pellet injected discharge for alternative injection showing (a) H$_\alpha$ ablation light, (b) central electron temperature T_{e0}, (c) Plasma stored energy and the port through NBI power, (d) line averaged electron density $\bar{n}_e$.

ion density; the vertical deflection depends on the local pitch angle of the field lines where, the toroidal deflection of the pellet starts. Owing to the toroidal deflection and high pitch angle at the outer plasma radii, the pellet resides most of the time in the outer flux surface, although it seems to be penetrating radially more inside the plasma. The penetration depth of the pellet is reduced due to its three-dimensional deflection. Another point to be noted is, this deflection drives the pellet to a location having similar characteristics as that of the LFS injection (in case of CW toroidal deflection only). Taking into account of these aspects, estimation of the pellet penetration depth

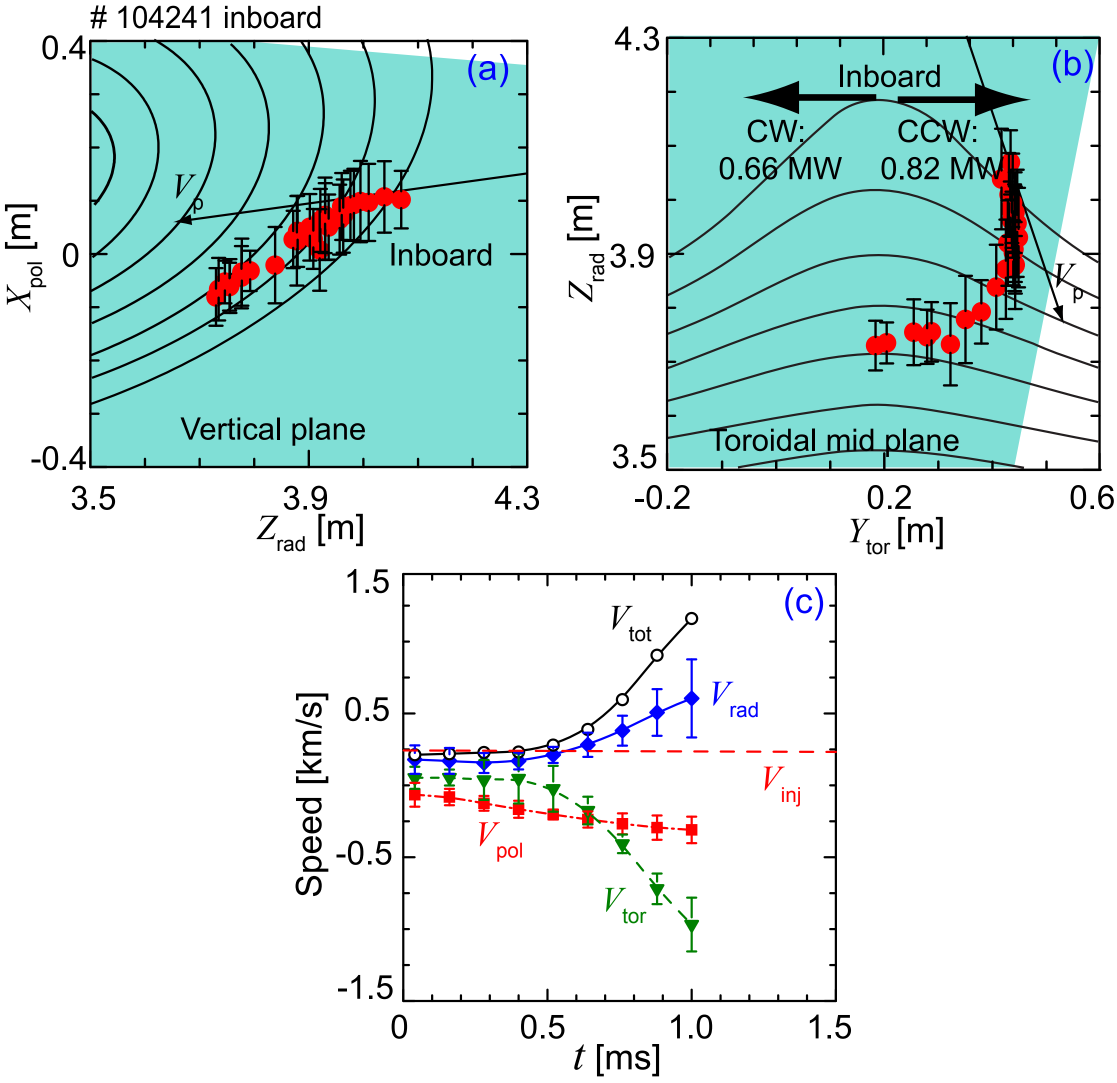

Figure 6.8 Reconstructed pellet trajectory for alternative location injected pellet on (a) vertical plane ($\phi = 23^\circ$ section) and (b) toroidal mid-plane of LHD. The shaded area indicates the viewing area of the observation system. (c) Pellet speed in three directions, injection speed and the total speed of the pellet.

by considering the constant pellet speed and ablation time can lead to wrong information. The use of the stereoscopic diagnostics makes it possible to measure the penetration depth of the pellet independent of its injection parameters within the uncertainty of the ablation cloud dimension (in addition to the calibration error). The pellet speed in toroidal (V_{tor}), radial (V_{rad}), and poloidal (V_{pol}) directions is shown in Fig. 6.8(c). The corresponding positive values represent the CCW, radial and vertically upward directions, respectively. In different plasma conditions maximum toroidal deflection up-to 40 cm has been observed. The total speed of the pellet, V_{tot}, remains equal to the injection speed before the pellet deflection. The increase in toroidal deflection speed mainly contributes to the increased total pellet speed. Also, an increase in radial speed of the pellet at its latter phase of the moton can be observed from the figure, with higher uncertainty. This increase may be explained by considering the geometrical angle of interaction between the fast ion flux and the pellet itself. The passing fast ions follow the field lines on to the pellet surface. With the start of the deflection, as the pellet resides on the outer flux surfaces due to simultaneous toroidal and vertical deflection, the angle between the field line and the pellet radial direction decreases. At this situation, considering the geometry of the field lines, there is a certain probability that the fast ions heat the pellet from its injection side, and hence there is a increase in pellet speed along the radial direction. The toroidal deflection speed and acceleration is found to be $\approx$ 1 kms^{-1} and 2 $\times 10^6$ ms^{-2}, respectively.

In the case of the LFS injection it has been found that the pellet deflection depends upon the direction of effective NBI power, whenever both kind of beams are applied simultaneously (in fact depends upon effective fast ion density). However, in the case of the inboard injection, the pellet always deflects along CW direction, if there exists a CW NBI beam. The toroidal acceleration of the pellet depends upon the fast ion density in the plasma. Therefore, a qualitative analysis of the toroidal deflection as a function of the ratio of the fast ions density in CW and CCW direction is shown in Fig. 6.9. In this figure, $F^{\text{max}}_{\text{cw/ccw}}$ is the maximum of the ratio of CW and CCW fast ion density taken within the region (ρ = 0.8-1.0), where the pellets get ablated. The solid circles with red color represent the pellet having significant CW-toroidal deflection and blue color with no CW-deflection. The negative and positive sign of Δ_{tor} represents the CW and CCW directions, respectively. In one discharge, where only CCW NBI beam is present (hollow circle), no CW

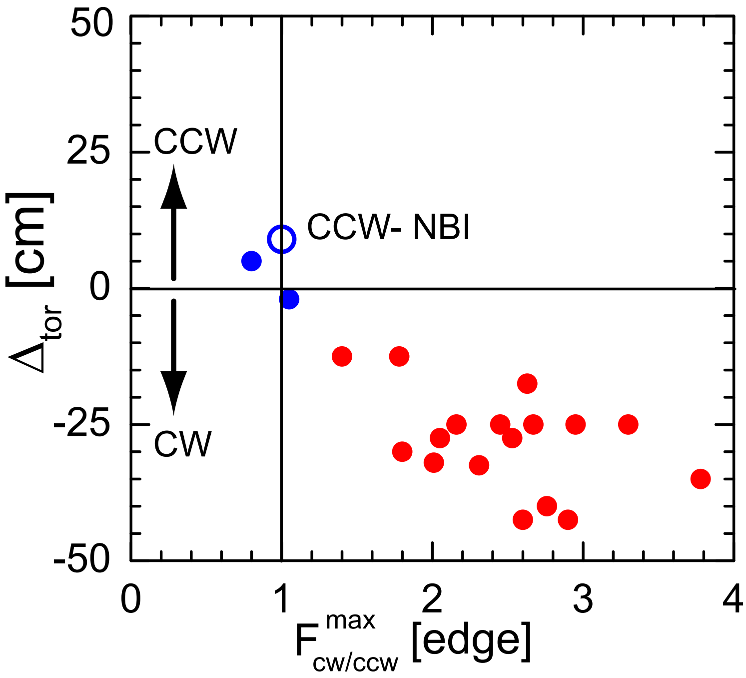

Figure 6.9 Pellet toroidal deflections as a function of the fast ion density ratio.

deflection has been observed. It can be observed that the pellets having $F^{\mathrm{max}}_{\mathrm{cw/ccw}} > 1$ have only CW deflection and, the deflection distance increasing with the ratio of the fast ions density. In addition to the fast ion density, the geometry of interaction between the pellet and the fast ion plays a significant role in pellet deflection. Qualitatively, differences between the CW toroidal deflection for the LFS and HFS injection can be understood as follows. In the case of the inboard HFS injection, the pellets are injected little tangentially. In this injection condition, the interaction angle of the fast ion with the pellet is less and the effective area of the fast ion collection on pellet surface is higher. In addition, the pellet spent more time on the same flux surface. Since the CW fast ion density is significantly high in the outer layer of the plasma, the possibility of the pellet deflection is higher in this case. In contrast, for the outboard LFS injection, the pellet is injected radially and the interaction angle between the fast ion and pellet is higher. Due to the radial injection, pellet residing time in each flux surface is less in comparison to tangential injection (inboard). Therefore, the pellet get deflected to CW toroidal direction in the case of the LFS injection, only when the effective NBI is in the CW direction.

Another feature of the pellet toroidal deflection, dependence of the deflection speed on the background plasma parameters is illustrated in Fig. 6.10. The maximum toroidal deflection speeds are plotted (inboard: open diamonds; outboard: solid diamonds) as a function of the ion collision time, τ_{col}. The size of the symbol represents the deposited NBI power for the corresponding pellets. The dashed line indicates a power fitting of the maximum toroidal deflection in terms of the collision time (τ_{col}^{c}). Where, c, an arbitrary constant, is the fitting parameter. It can be inferred from the figure that the toroidal deflection speed increases with the ion collision time. At higher collision frequency (low collision time), a rapid decrease is toroidal deflection speed can be observed from the figure. The above observation is explained as follows. At higher temperatures

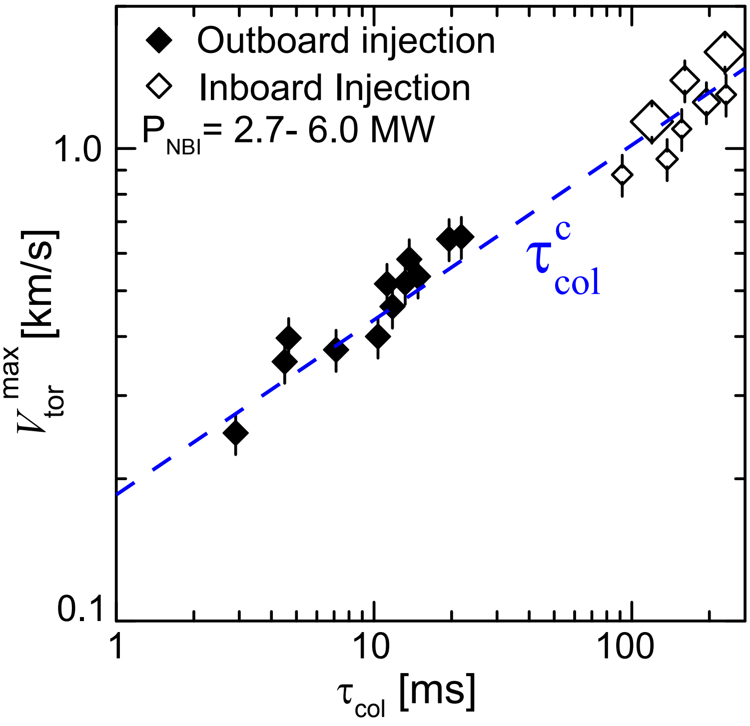

Figure 6.10 Maximum toroidal deflection as a function of the ion collision time for the inboard (open diamond) and outboard injection (solid diamonds).

there is a lower background density, and vice-versa. Since, ion collision time is $\propto T_{\mathrm{e}}^{3/2}/n_{\mathrm{e}}$, the collision time increases with increase in temperature and decrease in density. At higher collision frequency, the density of the passing fast ions reduces due to the higher collision rate. The decrease in fast ion density reduces the ablation rate due to the fast ions. Therefore, the rocket acceleration generated by the asymmetric ablation is reduced and hence the toroidal deflection.

Considering the above discussed pellet deflections in the CW toroidal direction, where a pellet approaches to the LFS characteristics region, pellets having lesser CW deflection, or CCW deflection has been considered for mass deposition analysis. A comparison between the mass deposition behaviors for a lesser CW deflected pellet (# 104237), and CCW deflected (# 102885) pellet is shown in Fig. 6.11. In the discharge # 104237, the pellet penetration depth is estimated by using the stereoscopic diagnostics. It can be observed from the figure that the measured penetration depth matches well with the perturbation in temperature profile due to the pellet penetration. Since the pellet deflects to a region having similar characteristic as that of the LFS injection, similar mass deposition profile as that of the LFS has been found in this case. The difference in H_{α} peak and the mass deposition peak is found to be $\approx$18 cm. Mass deposition profile in the case of a CCW deflected pellet is shown in Fig. 6.11 (right side figures). Due to lack of stereoscopic diagnostic in this case, penetration depth is estimated from the product of the pellet speed and the ablation time. Since, the pellet deflection starts more inside the plasma for CCW NBI (chapter-5), and the pellet is approaching to a smaller cross section, less error in penetration depth estimation assuming the constant speed of the pellet is expected. It can be observed that the estimated penetration depth matches well with the perturbation in temperature profile, obtained from the Thomson scattering diagnostic system. With similar n_{e} and T_{e} profile, the point to be noted that the penetration depth in CCW NBI case is much higher than the CW deflected pellet. Accompanied with the higher penetration, a little improvement in Δn_{e} peak position in comparison to the HFS CW deflected and the LFS injection case is evidenced from the figure. Although, there seems to be a little improvement, but it is not satisfactory. Concerning to the Δn_{e} peak position, possibility of the

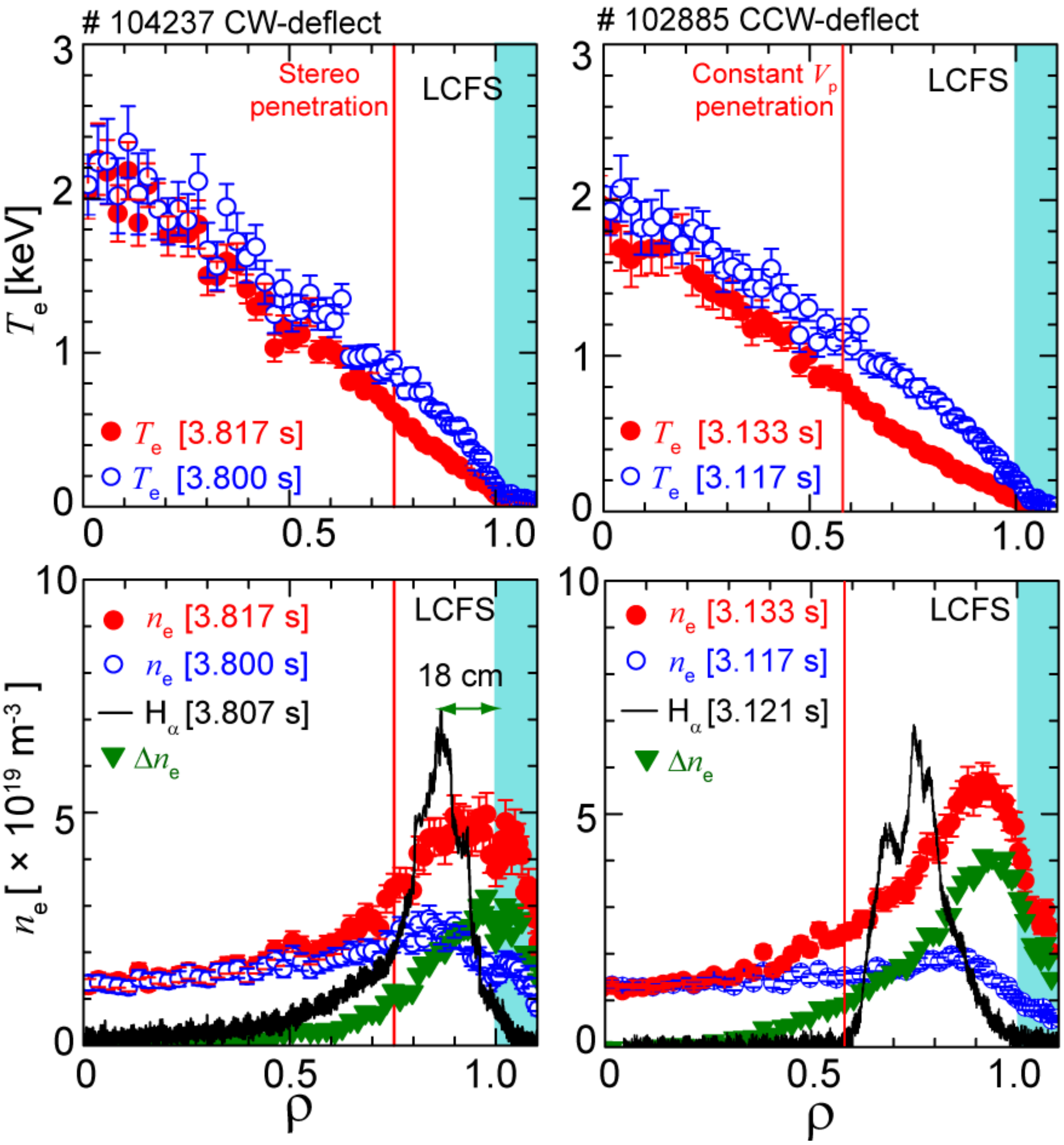

Figure 6.11 Radial profiles of the T_e and n_e obtained from the Thomson scattering diagnostic in the case of (left) less CW deflected pellet (# 104237), and (right) CCW deflected pellet (# 102885). The particle deposition profile, which is the difference in the density profile after and before the pellet injection, is shown by the inverted solid triangles. H_α ablation light indicating the pellet penetration depth is also shown.

pellet approach to the HFS characteristics region cannot be ruled out at its final phase of motion. Due to the lack of stereoscopic measurement system for CCW deflected pellet, it is difficult to predict the exact location and mass deposition characteristics for this injection case.

6.3.3 Plasmoid drift and mass redistribution

In previous subsections, it has been shown that the peak of the mass deposition profile lies at outer layer of the plasma in comparison to the pellet penetration depth. These observations are similar to the observations reported in the tokamak for LFS injection. The observed discrepancy in deposition is explained by analyzing the plasmoid dynamics obtained from the fast camera observation.

The fast three-dimensional observation system not only gives the information about the pellet position, but also the information regarding the ablated mass redistribution in the plasma can be extracted simultaneously. A typical frame of the fast camera image for two different viewing positions is shown in Fig. 6.12. In these images, it is assumed that the brightest part is the pellet position, and the spindly bright part expanding along toroidal direction transverse to the injection direction is the pellet plasmoid. Apart from the high intensity region, multiple low intensity plasmoids separated from the main cloud in parallel direction can be observed. These are the drifted plasmoid mass separating from the main cloud and its direction is opposite to that of the pellet penetration direction. Using the two views, it has been possible to calculate the absolute position of the pellet and the separating plasmoid, dimension of the plasmoid, extent of the plasmoid drift and the drifting speed. The absolute position of the pellet in the case of the LFS and the HFS are $\rho = 0.85$ and 0.9, respectively. The maximum error in measured position is ± 0.03. Typical fast camera sequence for an ablating pellet in the case of the LFS and the inboard HFS injection is shown in Fig. 6.13. The images from the fast camera are taken at a frame rate of 20 μs with 20 μs exposure time. Initially the cloud surrounding the pellet moves with it. After a certain penetration, the smooth path of the pellet gets striated with the separated cloudlets. The frame time t = 0 μs is taken for the pellet position at $\rho = 0.88$ (LFS) and 0.92 (HFS), where first striation of

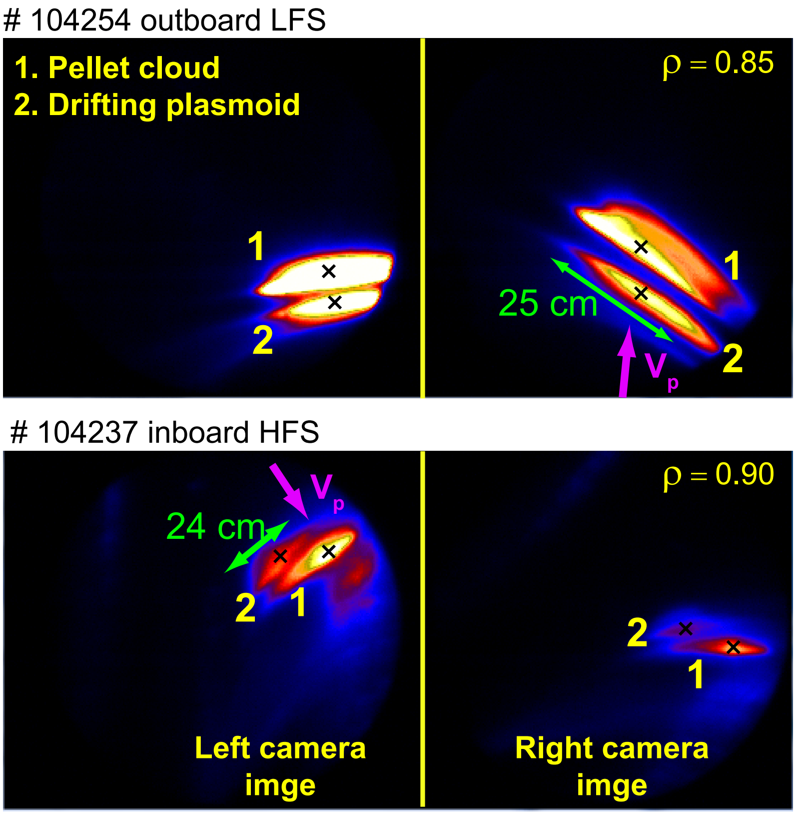

Figure 6.12 Typical fast camera view of an ablating pellet from two different observation points for, (top) outboard LFS and (bottom) inboard HFS.

the pellet has been observed. The specific conditions at which these striations arise is not analyzed in this study. The arrows in this frame indicate the pellet injection direction and the tangential NBI directions. The maximum elongation and width of these plasmoids is found to be $\approx$ 50 cm and 5 cm, respectively. On the time-integrated frame, these elongated structures appear to form a separated and regularly stacked cloud. Similar kind of observation has also been reported from TEXT [108]. The pellet and the breakaway plasmoids are indicated by 1 and 2, respectively. The directions of the breakaway plasmoid in both cases are indicated by the arrows. It can be observed from the figure that, there exist multiple striations in one image frame. In some discharges, up-to five striated structures have also been observed. Since the exposure time of the camera is 20 μs,

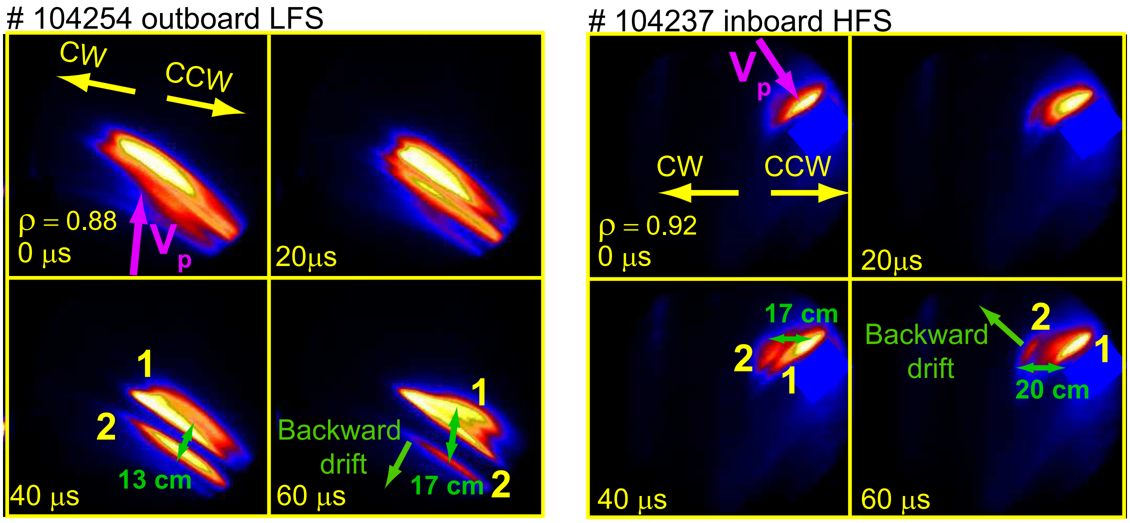

Figure 6.13 Typical fast camera image sequence (single view) of an ablating pellet in both type of injection, showing break-away plasmoids drifting in a direction opposite to that of the pellet injection direction .

several breakaway plasmoids can be expected in one camera frame. Therefore an imaging system with suitable frame rate is necessary to know the dynamics of these fast separating plasmoids. To characterize the fast plasmoid dynamics, a two-dimensional measurement of the H_α ablation light by using the bundled fiber with fast PIN-photodiode at 1 MHz acquisition rate has been performed recently, in LHD. From that measurement, it has been estimated that the breakaway frequency of these plasmoid is more than 100 kHz, which corresponds to the time of 10 μs [109, 110] or less. In this stereoscopic measurement as the exposure time was set at 20 μs, there exist multiple striations, and it has been possible to measure the drifting speed of these separated structures. Due to the high separation frequency of the plasmoid, the separated plasmoids in two consecutive frame are not necessarily be the same one. By taking the estimated separation distance of these plasmoids and the frame rate of the measurement, the velocity of these drifting ablatant is calculated as 6 -12 kms^{-1}. In this way the calculated speed is lower limit of the measurement, and it can be correctly estimated by using the fast measurement system with suitable frame rate. These kinds of structure are visible up-to 20 cm away from the pellet position. The estimated drift distances are comparable to the difference between the pellet penetration and mass deposition peak position, shown in the Thomson scattering diagnostics (Fig. 6.6) and (Fig. 6.11). From the Fig. 6.13, it is evident that the clouds are drifting down the ∇B (opposite to the pellet injection direction) in a direction outward to that of the plasma. These observations indicate the expulsion of the pellet particles from the ablation region before being captured by the magnetic field. The direction of the drift is similar in the case of the LFS injection and the inboard HFS injection with CW deflection. Therefore, it can be said that the observed mass redistribution is similar to that of the phenomenon reported in tokamaks. The effect of this redistribution on the fueling efficiency is discussed in next section.

The observed drift of these clouds can be explained as follows. The ablated neutral gas surrounding the pellet ionizes further, and forms a high-density low temperature cloud (plasmoid). The neutral gas cloud and the plasmoid shields the pellet against the incoming heat flux. A part of the incoming flux is stored as thermal energy inside the plasmoid or emitted radially. At this time, due to high pressure, the ionized cloud expands along the magnetic field line with ion sound speed, $\approx 10^4$ ms^{-1}. The thermal speed of the incoming electron flux from the background plasma is three orders of magnitude higher than the cloud expansion speed [75]. Due to the slower expansion of the ionized cloud in comparison to the incoming heat flux, the energy density inside the cloud increases rapidly, and it forms a locally high β_p plasmoid. The enhancement of the β in comparison to the background plasma can be calculated by taking the local n_e and T_e profile of the plasmoid and the background plasma from the following equation.

$$\beta = \frac{2\mu_0 k_\mathrm{B} n_\mathrm{e} T_\mathrm{e}}{B^2} \tag{6.2}$$

Where, B, is local magnetic field strength, μ_0, is vacuum permeability, and k_B is the Boltzman constant. In presence of the inhomogeneous magnetic field, due to the $\boldsymbol{B} \times \nabla B$ drift of ions and electrons, a polarization electric field is produced inside the plasmoid [101]. A detail picture of this is explained in Chapter-2. This polarized electric field interacting with the toroidal magnetic field pushes the plasmoid down the magnetic field gradient, out of the plasma. Different mechanisms that can compensate the drift inside the plasmoid are discussed in [19]. The multi channel FIR interferometer signal has also confirmed the outward redistribution of the pellet ablatant. The high time resolution (10 μs) line averaged density signal for the LFS and the inboard HFS pellet injection is shown in Fig. 6.14. The H_α signal in the figure indicates the pellet ablation duration.

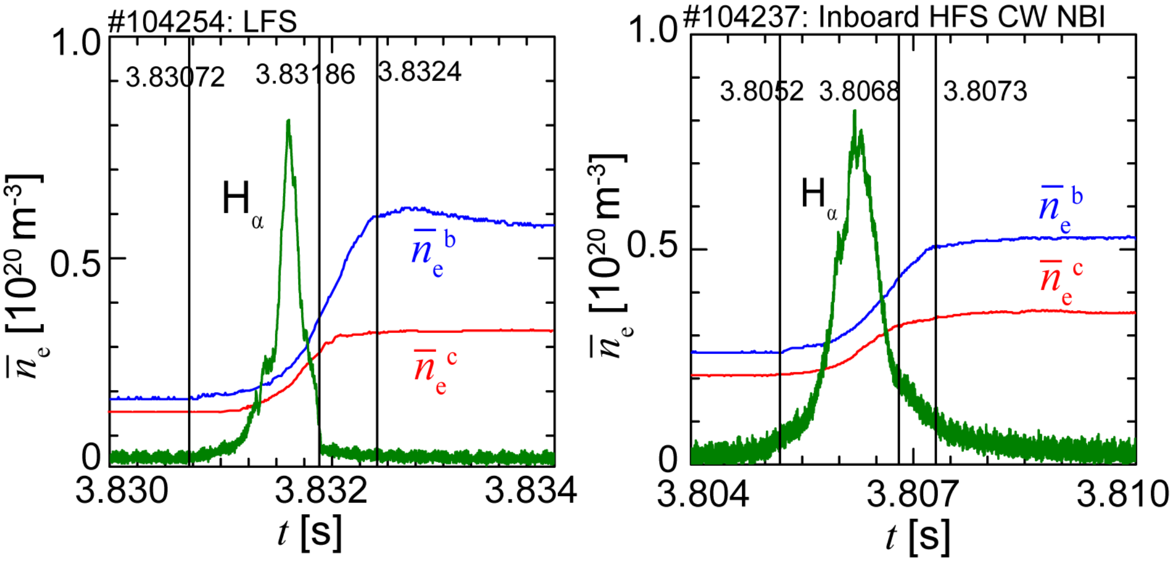

Figure 6.14 Temporal evolution of the pellet ablation light and the line averaged density for the chords at the boundary ($\bar{n}_e^b$) and core plasma ($\bar{n}_e^c$) .

The signals $\bar{n}_e^b$ and $\bar{n}_e^c$ represent the line averaged density signal for the chords at the boundary and the core region of the plasma, respectively. In both type of injection conditions, it can be seen that the signal from the core and boundary density starts to increase with the pellet ablation. The rise in core density signal stops just after the pellet ablation is finished (3.83188 s: LFS, 3.8068 s: HFS). Contrary to this, the boundary density signal rise continues up-to 3.8324 s and 3.8073 s for LFS and HFS injection, respectively. This observation is consistent with the previous observations in LHD, where an adiabatic redistribution of the ablatant at a time scale of 400 μs had reported.

6.3.4 Pellet fueling efficiency

The efficiency of the pellet fueling in case of the LFS and the inboard HFS injection is calculated for different plasma conditions. The ε_f is defined as the step increase of the plasma particle content due to the pellet injection divided by the number of particles in the injected pellet ($\varepsilon_f = \Delta N_e/N_e$) [111]. The pellets are injected through the curved guide tubes for the outboard (2.5 m, R_{bend} = 0.8 m: 2 bends) side and the inboard side (21 m, R_{bend} = 0.8 m: 5 bends) of the plasma. Due to lack of mass measurement system during the plasma discharges at the guide tube exit, pellet mass loss of 10 % of standard pellet size has been assumed for the inboard and the outboard side injection locations. The particle deposition in the plasma is calculated as, $\Delta N_e = \int \Delta n_e dV$, where Δn_e, is the difference in the Thomson density profile before and just after the pellet injection, and dV, is the plasma volume between the integrated profile points. The Thomson scattering data's are obtained within 2-10 ms after the pellet injection. A plot for the ε_f as a function of the pellet penetration depth is shown in Fig. 6.15(a). It is very clear from the figure that, ε_f increases with the increase in

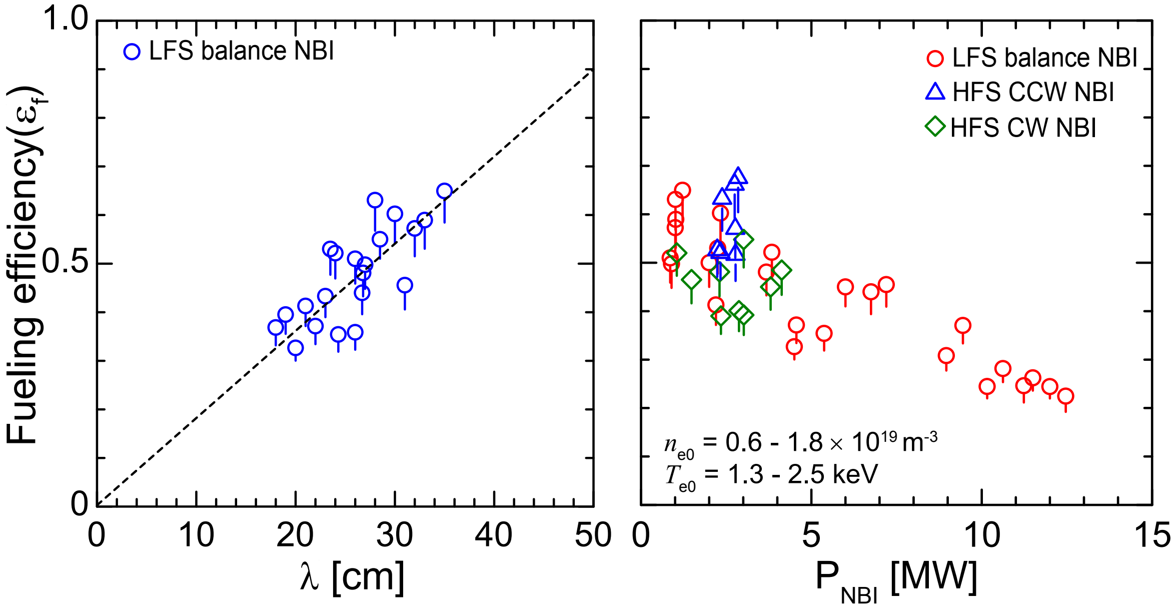

Figure 6.15 (a) Pellet fueling efficiency as a function of the penetration depth. (b) Degradation of the ε_f with the increase in NBI power.

pellet penetration depth. A linear fitting of the trends in ε_f data is shown by the dashed line. Since the pellet trajectory in the case of the alternative injection is not linear, only LFS pellet data's are shown in this plot. The error bars represent the scattering in ε_f for no mass loss. In the previous section, it has been discussed that the ablated mass drifts out of the plasma. Therefore, it clearly signifies that the drift of the ablated mass is the primary reason for the lesser fueling efficiency. From the trends in the efficiency curve, it can be anticipated that, the maximum efficiency can be obtained for the pellet penetration of more than 50 cm. Since the plasma minor radius at this injection cross section is $\approx$ 70 cm, this result is quite reasonable.

With the increase in NBI heating power, degradation of the ε_f has also been observed. Estimated values of the ε_f as a function of the NBI power for LFS, HFS CW and HFS CCW NBI are plotted in Fig. 6.15(b). It can be observed that the efficiency for the HFS CW injection is lower than the corresponding case for the CCW injection and the LFS injection. This can be explained as follows. In the case of the CW deflection, the pellet is deflecting to the LFS characteristic region and simultaneously it ablates on the outer flux surfaces of the plasma. Therefore owing to the less penetration and outward drift of the ablated pellet mass, ε_f becomes low. In contrast, HFS CCW deflected pellet is approaching to the presumed HFS with smaller cross section, therefore the penetration on the flux surface is higher. Additionally, the possibility of reduction in $\boldsymbol{E} \times \boldsymbol{B}$ drift force for this condition cannot be ruled out. The drift of the ablated mass seems to be like that of the tokamak results [40, 85]. The possibility of the degradation of the ε_f at high P_NBI can be associated with two factors. The first cause is the loss of the penetration depth due to the increased ion ablation with NBI power. Second possibility is the increase in β inside the plasmoid, associated with the higher heat flux on the ablation cloud, and subsequently higher cross field drift of the deposited mass down the magnetic field gradient, outward to that of the plasma.

6.4 Summary

In order to find the optimized pellet fueling conditions, pellet injection experiment has been carried out from multiple injection locations in the LHD. Considering the cross field drift of the ablating mass in presence of the asymmetric magnetic field, two injection locations are considered for the pellet injection. For the LFS, an injection location below the horizontally elongated section is chosen. For the HFS, injection of a pellet obliquely from the horizontally elongated inboard section to a location close to the helical coil has been considered.

It has been observed that the fast ions generated in presence of the tangential neutral beam deviates the pellet from its injection direction toroidally and vertically. Due to this 3D deflection, a pellet deviates from its injection direction in both kind of injection conditions. Deflection of the pellet trajectory exponentially varies with the ion collision time. Since, a pellet is injected little tangentially, deflection plays a major role for the inboard HFS injection case. In case of the inboard injection with CW deflection, the pellet approaches to a region having similar characteristics as that of the LFS injection. In CCW deflected inboard injection discharges, since the pellet is approaching to a shorter cross section and CCW deflection is limited at the edge region, an improved penetration has been observed.

Although, the pellet able to penetrate to one fourth or half of the plasma radius, it has been found that the mass deposition profile lies at the edge of the plasma. Due to significant increase in the pellet penetration for inboard CCW injection case than the CW case, little improved deposition peak, and the efficiency have been observed. Although there is a little improvement in the deposition peak, it is still unsatisfactory as the efficiency looks similar to that of the LFS injection conditions. This phenomenon is explained by the formation of a high β plasmoid and subsequently, ∇B induced $\boldsymbol{E} \times \boldsymbol{B}$ drift of the plasmoid down the magnetic field gradient, outward to that of the plasma. The estimated drift of this pellet ablatant far exceeds the injection speed of the pellet in a direction opposite to that of the pellet penetration. The observed separation of the drifting plasmoids are comparable to the differences between the penetration depth and the peak of the mass deposition profile. Due to this fast outward redistribution of the pellet mass, fueling efficiency of 65 % or less has been obtained. Whereas, the ε_{f} increases with the pellet penetration into the plasma, degradation of it has been found with NBI power.

The redistribution of the pellet mass presented here qualitatively agrees with the results in tokamak, considering the ∇B induced drift of the pellet plasmoid. In case of CCW-NBI, due to unavailability of the 3D measurement system, the exact ablation region has not been elucidated. Therefore, it is premature to predict the viability of enhanced mass deposition characteristics considering the ∇B induced drift in LHD. If there exist a common physical mechanism between the helical system and the tokamak, and if the pellet can be able to approach the optimized location, an enhanced fueling behavior as like that of a tokamak can be hopeful. Therefore, more experimental studies for the inboard HFS pellet injection with CCW-NBI conditions are necessary. From the theoretical point of view, considering the 3D helical magnetic configuration, an advanced modeling is necessary in-order to understand the detailed dynamics of the ∇B induced drift effect on the pellet ablatant in LHD.

Chapter 7

Summary and Conclusion

The study of two important aspects of the pellet fueling in the fusion devices, pellet ablation and mass distribution process are presented in this thesis. Using a fast 3D imaging diagnostic, three-dimensional interaction between the pellet and the plasma, and its effect on the fueling process is revealed. Extending the results presented in this study, prospects for the pellet fueling studies in the reactor scale plasmas are discussed in this section.

Pellet injection experiment is carried out by using a newly developed low speed single barrel pellet injector, which works on the combined operation of a mechanical punch and pneumatic propellant. Considering the intactness of the pellet inside the guide tube, the injection speed of the pellet during the experiment is limited to 275 m/s or less. In order to understand the pellet ablation behavior in presence of a 3D magnetic configuration in LHD, a three dimensional camera observation system basing on the stereoscopic principle has been calibrated. This diagnostic uses a single fast camera (20-50 μs time and 512 × 232 pixel resolution) and a coherent bifurcated imaging fiber to obtain the pellet ablation images. This diagnostic not only helps us to reveal the three-dimensionality in the pellet-plasma interaction, but also it has been possible to measure the mass deposition characteristics, simultaneously.

In future fusion devices with electron temperature up to 20 keV, core penetration of the pellet and hence the effective fuelling is one of the major concern. The fueling factor is primarily governed by the ablation dynamics of the pellet. In this regard, the prime conclusion can be drawn from this study in chapter-5 is the pellet ablation by high energy particles in the plasma. In presence of theses particles, pellet ablation is enhanced and there is a shortening of the penetration depth. These energetic particles are generated either by the external heating or by itself in the plasma such as suprathermal electrons and α particles. At higher T_e, the contribution of these particles to the ablation will be higher, hence the ε_f will be greatly affected in future devices with reactor conditions. However a negligible contribution to ablation from the fusion born α particle is expected, as reported by *Ho & Perkins* [112].

Implicit with the fast ion ablation, another thing can be concluded is the effect due to the asymmetry in distribution of theses energetic particles surrounding the pellet. Due to this asymmetry, an unbalanced ablation can deflect the trajectory of the pellet from its injection direction. This can lead to shortening of the penetration depth and hence the efficiency of the fueling. It has been also shown that, with the start of pellet toroidal deflection, helicity of the field lines leads to a three dimensional trajectory of the pellet. Any asymmetry in pellet shielding cloud on the front and rear side of the injected pellet (while considering mass drift) can also change the pellet penetration speed. In reactor conditions, with increase in required external heating power, the generation of these energetic particles will be higher and hence the above discussed process will be dominant. At this point, the thing to be considered is the effective contribution of the ion and electrons to the ablation process depending on their effective cross section. The deflection of the pellet depends upon the slowing down time of the energetic ions. Plasmas with higher T_e and lower n_e have higher slow down time and hence the enhanced effect on ablation dynamics can be predictable for fusion devices.

Another important aspect of this thesis is the study of the pellet mass deposition inside the plasma. With regard to this, mass deposition results are presented for the outboard LFS and inboard HFS injection in chapter-6. Although mass deposition characteristic is still inconclusive for the HFS injection due to the pellet deflection, the results from the LFS mass deposition properties in LHD can be extended to the prospect for the injection position optimization in future devices. The observed mass deposition at the outer layer of the plasma can be related to the drifting of the plasmoid down the ∇B, which is similar to the observation in tokamaks. The speed of the drifted plasmoids are up-to 12 kms^{-1}, and the distance of the separation from the ablated region agrees well with the mass deposition radius. In reactor conditions, higher drift on the pellet can be predictable due to the following reasons. At higher T_e, there will be higher ionization inside the plasmoid due to the high heat flux on the pellet surface. Owing to the high pressure, there will be an enhancement of the β of the cloud. Due to the increase in the ionization rate, vertical electric field inside the plasmoid will be also increase. This β enhanced cloud in presence of the higher $\boldsymbol{E} \times \boldsymbol{B}$ force will experience enhanced drift velocity. Therefore in one way for LFS injection it will cause low efficiency, on the other way it can favor fueling for HFS injection.

From these discussions, it can be simply concluded that, in future fusion machines there will be negative effect on ε_f with the increase in plasma size, shortening of the pellet penetration due to enhanced ablation, and finally the drift of the ablated mass for the conventional LFS fueling. For deep penetration of the pellet, high speed pellets are necessary. Extending the validity of the mass drift for the LFS injection in LHD, it can be concluded that, instead of increasing the pellet speed, fueling optimization considering the ∇B effect on the plasmoid is necessary in reactor conditions. Hopefully, higher efficiency can be expected owing to the ablated mass drift from the HFS pellet injection in the torus.

Further experimental study for different pellet speed and plasma parameters can help to improve the understanding of the pellet deflection in presence of the NBI heated plasma in LHD. Although, a similarity in fueling behavior between LHD and tokamak in case of LFS injection has been found in LHD, it is still premature to predict the HFS fueling behavior, and is hopefully positive if there exists a common physical mechanism in tokamak and helical system. Pellet injection experiments from the inboard HFS with CCW NBI beam is favorable for a better understanding of the HFS fueling characteristics in LHD. Another important issue is, the dynamics of the fast breakaway plasmoids, which can also be further investigated. From the theoretical point of view, an advanced modeling considering the three dimensional plasma configuration is helpful to understand the dynamics of the ∇B induced drift effect on the pellet ablatant in LHD.

Bibliography

[1] John Sheffeld, A. Gibson, P. Vandenplas, et al., "World population and energy demand growth: The potential role of fusion energy in an efficient world [and discussion]", *Philsophical Transactions Mathematical, Physical and Engineering Sciences*, 357, (1752):377-395 (MAR 1999).

[2] "UN Energy Report: The Energy Access Situation in Developing Countries: A Review Focusing on the Least Developed Counties and Sub-Saharan Africa", (2009). http://www.un.org/apps/news/story.asp?NewsID=33049&Cr=energy&Cr1.

[3] World energy resources and consumption http://en.wikipedia.org/wiki/World_energy_resources_and_consumption#cite_note-EIA-0.

[4] John Wesson, "Tokamaks", Chapter 1.8, p.25, Clarendon Press - Oxford, (2004).

[5] John Wesson, "Tokamaks", Chapter 1.2, p.4, Clarendon Press - Oxford, (2004).

[6] M. J. Gouge, Fusion Technology, 34, 435 (1998).

[7] "ITER, The way to new energy", http://www.iter.org/

[8] K. Miyamoto, Poster abstract (p-22.2), 17th IEEE/NPSS symposium on Fusion Engineering, San Diego, Ca, USA, October 6-10, (1997).

[9] M. Greenwald, et al.,"Energy Confinement of Hgih-Density Pellet-Fueled Plasmas in the Alcator C Tokamak", Phys. Rev. Lett. 53, 352 (1984).

[10] L. R. Baylor, "Improved core fueling with high field side pellet injection in the DIII-D tokamak", Phys. Plasmas 7, 1878, (2000).

[11] S. L. Milora et al.,"Confinement of high-density pellet-fueled discharges in TFTR", Plasma Phys. Control. Fusion 28, 1435, (1986).

[12] M. Kaufman et al., "Pellet injection with improved confinement in ASDEX", Nucl. Fusion 28, 827 (1988).

[13] B. J. D. Tubing et al., "H-mode confinement in JET with enhanced performance by pellet peaked density profiles", Nucl. Fusion 31, 839 (1991).

[14] M. Nagami, JT-60 Team, "Recent results in JT-60 experiments",
Plasma Phys. Control. Fusion 31, 1597, (1989).

[15] Y. Kamada et al., "Improved confinement characteristics of pellet fueled discharges on JT-60", Nucl. Fusion 29, 1785 (1989).

[16] R. Sakamoto et al., "Impact of pellet injection on extension of the operational region in LHD", Nucl. Fusion 41, 381 (2001).

[17] P. B. Parks and R.J. Turnbull, "Effect of transonic flow in the pellet ablation cloud on the life time of a solid hydrogen pellet in a plasma", Phys. Fluids 21, 1735 (1978).

[18] L. R. Baylor et al., "Pellet fuelling and control of burning plasmas in ITER",
Nucl. Fusion, 47, 443 (2007).

[19] B. Pégourié et al., "Homogenization of the pellet ablated material in tokamaks taking into account the ∇B-induced drift", Nucl. Fusion, 47, 44 (2007).

[20] S. Sudo et al., "Particle transport diagnostics on CHS and LHD with tracer-encapsulated solid pellet injection", Plasma Phys. Control. Fusion, 44, 129 (2002).

[21] R. D. Durst et al., "q-profile measurement in tokamaks using fueling pellets",
Rev. Sci. Instrum. 59, 8l, 1623 (1988).

[22] P. T. Lang et al., "ELM frequency control by continuous small pellet injection in ASDEX Upgrade", Nucl. Fusion 43, 1110, (2003).

[23] A. Iiyoshi et al., "Overview of the Large Helical Device project",
Nucl. Fusion, 39, 9Y, 1245 (1999).

[24] A. Komori et al., Plasma Physics and Controlled Nuclear Fusion Research 1994 (Proc. 15th Int. Conf. Seville, 1994), Vol. 2, IAEA, Vienna, 773 (1995).

[25] S. Kubo et al., "Achievement of 10keV Central electron Temperatures by ECH in LHD", Plasma Fusion Res. 78, 99 (2002).

[26] O. Kaneko et al., "Engineering prospects of negative-ion-based neutral beam injection system from high power operation for the large helical device",
Nucl. Fusion 43, 692 (2003).

[27] A. Komori et al., "Overview of the Large Helical Device",
Plasma Phys. Control. Fusion 42, 1165 (2000).

[28] J. Miyazawa et al., "Fueling efficiency of gas puffing on large helical device",
Journal of Nucl. Materials 313-316, 534 (2003).

[29] H. Yamada et al., "Repetitive fueling pellet injection in large helical device", Fusion Eng. Des. 69, 11 (2003).

[30] R. Sakamoto et al., "Repetititve pellet fuelling high-density/steady-state operation on LHD", Nucl. Fusion 46, 884 (2006).

[31] S. Murakami et al, "Simulation Study of Energetic Particle Distributions during ICRF and NBI Heating in the LHD Plasma", J. Plasma Fusion Res. Ser. 2, 255 (1999).

[32] H. S⊘rensen et al., "A microwave cavity for measurement of the mass of hydrogen pellets", Rev. Sci.Instrum. 61, 3464, 11 (1990).

[33] G. Motojima et al., "High-speed imaging spectroscopy for pellet plasmoid observation in LHD", 37th EPS Conference on Plasma Physics P5.173 (2010).

[34] S. Sudo et al., "Recent diagnostic developments on LHD", Plasma Phys. Control. Fusion 45, 1127 (2003).

[35] K. Kawahata et al., "A two color millimeter-wave interferometer for the measurement of line integral electron density on large helical device", Rev. Sci. Instrum. 70, 695 (1999).

[36] K. Kawahata et al., "Far infrared laser interferometer system on the Large Helical Device", Rev. Sci. Instrum. 70, 707 (1999).

[37] K. Tanaka et al, 2001 Proc. 5th Int. Workshop on Reflectometry NIFS-PROC-49

[38] K. Narihara et al., "Design and performance of the Thomson scattering diagnostic on LHD", Rev. Sci. Instrum. 72, 1122 (2001).

[39] V. Waller et al.,"Analysis of Pellet Toroidal Deflection in Sawtoothing Discharges", 29th EPS Conference on Plasma Phys. and Contr. Fusion Montreux, 17-21 June 2002 ECA Vol. 26B, P-5.083 (2002).

[40] L.R. Baylor et al.,"Pellet fuelling and deposition measurements on JET and TFTR", Nucl. Fusion, 32, 12, 2177 (1992).

[41] P. T. Lang et al.,"High density operation in H mode discharges by inboard launch pellet fuelling", Nucl. Fusion, 40, 2, 245 (2000).

[42] A. K. MacAulay,"Geometrical, kinetic and atomic physics effects in a two dimensional time dependent fluid simulation of ablating fuel pellets", Nucl. Fusion, 34, 1, 43 (1994).

[43] W.A. Houlberg et al., "Neutral gas and plasma shielding model for pellet ablation", Nucl. Fusion, 28, 4, 595 (1988).

[44] R. Ishizaki et al.,"Two-dimensional simulation of pellet ablation with atomic processes", Phys. of Plasmas, 11, 8, (2004).

[45] S. L. Milora, "New algorithim for computing the ablation of hydrogenic pellets in hot plasma",
Oak Ridge national laboratory rep., ORNL/TM-8616 (1983).

[46] Y. Nakamura, "An analysis of the ablation rate for solid pellets injected into neutral beam heated toroidal plasmas", Nucl. Fusion, 26, 7, 907 (1986).

[47] M. Kaufmann et al., "Plasma shielding of hydrogen pellets", Nucl. Fusion 27, 171 (1986).

[48] V. Rozhansky et al.,"Mass deposition after a pellet injection into tokamak",
Plasma Phys. Control. Fusion 46, 575 (2004).

[49] J S Mishra et al., "A low speed single barrel pellet injector and its application to complementary study on ablatant in LHD" J. Plasma Fusion Res. SERIES, 9, 106 (2010).

[50] S. K. Combs et al., "Eight shot pneumatic pellet injection system for the tokamak fusion test reactor", Rev. Sci. Instrum. 58, 1195 (1987).

[51] S. K. Combs et al., "Repeating pneumatic hydrogen pellet injector for plasma fueling", Rev. Sci. Instrum. 56, 1173 (1985).

[52] S. K. Combs et al., "Simple pipe gun for hydrogen pellet injection", Rev. Sci. Instrum. 57, 2636 (1986).

[53] S. K. Combs et al., "Performance of a pneumatic hydrogen pellet injection system on the Joint European Torus ", Rev. Sci. Instrum. 60, 2697 (1989).

[54] P. T. Lang et al., "80 Hz repetitive centrifuge injector for hydrogen pellets",
Rev. Sci. Instrum, 67, 619 (1996).

[55] H. Hiratsuka et al., "A four-pellet pneumatic injection system in the JT-60", Fusion Eng. and Design, 13, 4, 417 (1991).

[56] R. Sakamoto et al., "Development of Advanced Pellet Injector Systems for Plasma Fuelling", Plasma and Fusion Research, 4, 002 (2009).

[57] S. L. Milora et. al., "Pmeumatic hydrogen pellet injection system for the ISX tokamak", Rev. Sci. Instrum, 50, 4, 482 (1979).

[58] S. K. Combs et al., "New extruder based deuterium feed system for centrifuge pellet injection", Rev. Sci. Instrum., 68, 12, 4448 (1997).

[59] S. Sudo et al., Fusion Technology 20, 387 (1991).

[60] S. K. Combs et al., "High-field side pellet injection technology",
Fusion Technology, 34 , 419 (1998).

[61] K. J. McCrathy et al., "A compact flexible pellet injector for the TJ-II stellarator", Rev. Sci. Instrum, 79, 10F321 (2008).

[62] S. K. Combs, "Pellet injection technology ", Rev. Sci. Instrum, 64, 7, 1679 (1993).

[63] J S Mishra et al., "Design and performance of a punch mechanism based pellet injector for alternative injection in the large helical device", Rev. Sci. Instrum, 82, 023505 (2011).

[64] S. K. Combs et al., "ORNL mock-up tests of inside launch pellet injection on JET and LHD", Fusion Eng. and Design 58-59, 343 (2001).

[65] H. Yamada et al., "Development of pellet injector system for large helical device", Fusion Eng. Des. 49/50, 915 (2000).

[66] L. D. Landau, E. M. Lifshitz, Fluid Mechanics, Pergamon Press (1987).

[67] S. K. Combs et al., "Technique for measuring D2 pellet mass loss through a curved guide tube using two microwave cavity detectors", Rev. Sci. Instrum., 77, 073503 (2006).

[68] S. Sudo et al., Fusion technology, 14, 1334 (1988).

[69] A. Lorenz et al., "Impact strngth of cryogenic deuterium pellets for injection into tokamak plasmas", Rev. Sci. Instrum, 71, 10, 3736 (2000).

[70] B.Pégourié, "Review: Pellet injection experiments and modelling", Plasma Phys. Control. Fusion, 49, R-87 (2007).

[71] P. B. Parks et al., "A model for the ablation rate of a solid Hydrogen pellet in a plasma.", Nucl. Fusion, 17, 3 (1977).

[72] H. W. Müller et al., "High β plasmoid formation, drift and striations using pellet ablation in ASDEX upgrade.", Nucl. Fusion, 17, 301 (2002).

[73] S. L. Milora et al., "Review Paper: Pellet fuelling", Nucl. Fusion, 35, 6, (1995).

[74] G. A. Wurden et al., "Pellet injection techniques in the ASDEX tokamak", Rev. Sci. Instrum., 61, 11, 3602 (2007).

[75] H. W. Müller et al., "Improvement of q-profile measurement by fast observation of pellet ablation at ASDEX Upgrade", Rev. Sci. Instrum. 68, 4051 (1997).

[76] P. Innocente et al., "Three-dimensional time-resolved H pellet trajectory reconstruction in RFX by position sensitive detector H_α diagnostic", Rev. Sci. Instrum., 70, 943 (1999).

[77] M. Hoshino et al., "2-D PSD Diagnostic System for the Pellet Trajectory in LHD Plasmas", Plasma and Fusion Research: Letters, 3, 002 (2008).

[78] G. Kocsis et al., "A fast framing camera system for observation of acceleration and ablation of cryogenic hydrogen pellet in ASDEX Upgrade plasmas",
Rev. Sci. Instrum. 75, 11, 4754 (2004).

[79] A. C. Kak and M. Slaney "Principles of Computerized Tomographic Imaging", ISBN-0-87942-198-3.

[80] R. Sakamoto, "Three-dimensional observation system for pellet ablation traveling in the high-temperature plasmas", Rev. Sci. Instrum. 76, 103502 (2005).

[81] Gang Xu and Zhengyou Zhang, "Epipolar geometry in stereo motion and object recognition", Kluwer Academic Publishers, ISBN:0-7923-4199-6.

[82] Richard Hertley, Andrew Zisserman, "Multiple view geometry in computer vision", Chap-9, Cambridge Unversity Press (2000), ISBN-978-0-521-54051-3.

[83] Richard I Hertley, "In Defense of the Eight-Point Algorithm", IEEE TRANSACTIONS ON PATTERN ANALYSIS AND MACHINE INTELLIGENCE, 19, 6, 580, (1997).

[84] W. H. Press, S .A. Teukolsky, W. T .Vetterling, B .P. Flannery, "Numerical recipes in fortran 77", Cambridge University press.

[85] P. T. Lang et al.,"Pellet fuelling of ELMy H mode discharges on ASDEX Upgrade",
Nucl. Fusion 36, 1532 (1996).

[86] J. S. Mishra et al., "Observation of three-dimensional motion of pellet ablatant in LHD", P5.170, 37^{th} EPS Conference on Plasma Physics, Dublin, Ireland, (2010).

[87] L. Garzotti et al., "Investigation of Electron-Distribution Function and Dynamo Mechanisms in a Reversed-Field Pinch by Analysis of Hydrogen-Pellet Deflection",
Phys. Rev. Lett., 84, 24, 5532, (2000).

[88] V. Waller et al.,"Investigation of Current-Density Modification during Magnetic Reconnection by Analysis of Hydrogen-Pellet Deflection",
Phys. Rev. Lett., 91, 20, 205002, (2003).

[89] S. M. Egorov et al., "CURRENT DENSITY PROFILE AND ELECTRON BEAM LOCALIZATION MEASUREMENTS USING CARBON PELLETS ON T-10",
Nucl. Fusion, 32, 11, 2025, (1992).

[90] M. Hoshino et al., "Observation of the Effect of Energetic Ions on Pellet Ablation in the Large Helical Device", Plasma and Fusion Research, 1, 033, (2006).

[91] R. Sakamoto et al., "Observation of pellet ablation behaviour on the Large Helical Device", Nucl. Fusion, 44, 624 (2004).

[92] S. L. Milora et al., "RESULTS OF HYDROGEN PELLET INJECTION INTO ISX-B", Nucl. Fusion, 20, 12, 1491 (1980).

[93] H. H. Andersen et al.,"Hydrogen stopping powers and ranges in all elements" pg. 16-17, Pergamon press (1977).

[94] S. Morita et al., "Observation of ablation and acceleration of impurity pellets in the presence of energetic ions in the CHS heliotron/torsatron", Nucl. Fusion, 42, 876, (2002).

[95] B. Pégourié, "Modelling of pellet ablation in additionally heated plasmas", Plasma Phys. Control. Fusion, 47, 17 (2005).

[96] S. L. Milora et al., "Review Paper: Pellet fuelling", Nucl. Fusion, 35, 6, p.680 (1995)

[97] V. R. Rozhansky et al.,"On the Ablation Models of Fuel Pellets", Plasma Physics Reports, 31, 12, 993, (2005).

[98] J. A. Rome et al., "Neutral-beam injection into a tokamak, part I: fast-ion spatial distribution for tangential injection", Nucl. Fusion, 14, 141, (1974).

[99] I. Senichenkov et al., "The pellet rocket acceleration caused by ∇B-induced drift", 36^{th} EPS conf. on plasma Phys. (Warsaw), Vol. 31F, P-4.094 (2007).

[100] B. Pégourié et al., "Recent results on the fuelling and control of plasmas by pellet injection, application to ITER" Plasma Phys. Control. Fusion, 51, 124023 (2009).

[101] V. Rozhansky et al., "Evolution and stratification of a plasma cloud surrounding a pellet" Plasma Phys. Control. Fusion, 37, 399 (1995).

[102] P. T. Lang et al., "High-efficiency Plasma Refueling by Pellet Injection from the Magnetic High-Field Side into ASDEX Upgrade", Phys. Rev. Lett., 79, 8 (1997).

[103] J. de Kloe et al., "Fast backward drift of pellet ablatant in tokamak plasmas" Phys. Rev. Lett., 82, 13 (1999).

[104] H. W. Müller et al., "High-β plasmoid drift during pellet injection into tokamaks" Phys. Rev. Lett., 83, 11 (1999).

[105] D. Terranova et al.,"Pellet ablation and mass deposition in FTU: analysis of vertical and low field side injection experiments", Nucl. Fusion, 47, 288 (2007).

[106] J. S. Mishra et al.,"Observation of three-dimensional motion of the pellet ablatant in the large helical device" Nucl. Fusion, 51, 08039 (2011).

[107] L.R. Baylor et al., "AN INTERNATIONAL PELLET ABLATION DATABASE", Nucl. Fusion, 32, 12, 2177 (1992).

[108] R. D. Durst et al., "Experimental observations of the dynamics of pellet ablation on the Texas experimental tokamak (TEXT)",
Nucl. Fusion, 30, 1, 3 (1990).

[109] R. Sakamoto, "Observation of Intermittent Breakaway of Pellet Plasmoid in LHD", P5.183, 37th EPS Conference on Plasma Physics, Dublin, Ireland, (2010).

[110] R. Sakamoto et al., "Observation of Cross-Field Transport of Pellet Plasmoid in LHD", Plasma and Fusion Research, 6, 1402085 (2011).

[111] S. L. Milora et al., "Review Paper: Pellet fuelling", Nucl. Fusion, 35, 6, p.683 (1995).

[112] S.K. Ho and J. Perkins, Fusion Technol., 14, 1314 (1988).